

The Pennsylvania State University
The Graduate School
Department of Energy and Mineral Engineering

**THE ROLE OF PORE STRUCTURE IN PERMEABILITY EVOLUTION OBSERVED
IN LABORATORY STUDIES OF MARCELLUS AND WOLFCAMP SHALE**

A Dissertation in
Energy and Mineral Engineering
by
Brandon A. Schwartz

© 2018 Brandon A. Schwartz

Submitted in Partial Fulfillment
of the Requirements
for the Degree of

Doctor of Philosophy

December 2018

The dissertation of Brandon A. Schwartz was reviewed and approved* by the following:

Derek Elsworth
Distinguished Professor of Energy and Geo-Environmental Engineering
Dissertation Advisor
Chair of Committee

Shimin Liu
Assistant Professor of Energy and Mineral Engineering

Hamid Emami
Assistant Professor of Petroleum and Natural Gas Engineering

Chris Marone
Professor of Geophysics

Luis F. Ayala H.
Professor of Petroleum and Natural Gas Engineering
Associate Department Head for Graduate Education, John and Willie Leone
Family Department of Energy and Mineral Engineering

*Signatures are on file in the Graduate School

ABSTRACT

We explored the role of pore geometry and stiffness on the distribution of strain around pores for Marcellus and Wolfcamp shales. Relationships exist to model permeability evolution as well as bulk stiffness evolution—here we find a relationship relating these two variables to each other. Whereas bulk stiffness is determined by bulk mineralogy and initial pore structure, evolving bulk stiffness is determined by the evolution of the pore structure alone. Permeability evolution is also determined by the evolution of the pore structure. We cast the permeability evolution in terms of evolving material properties including the Poisson ratio, the crack density parameter, and the bulk modulus—all of which can be measured via acoustic waves. The end result is a method to measure permeability evolution via acoustic waves alone.

We modeled the effects of fracture spacing, aspect ratio, and pore stiffness on the permeability evolution of an ellipsoid crack under uniaxial stress and varying pore pressure. We found that rocks undergoing identical compressional strain and pore pressure can undergo significantly different magnitudes of fracture closure or dilation based on these three variables. This is especially important in gas shales, where nano-porosity is challenging to characterize and heterogeneity between basins has led to disparate permeability responses in the field and in the laboratory. We found that the aspect ratio is the most sensitive parameter influencing pore compressibility. The fracture spacing becomes important when external stress is applied, but it has no significant effect when pore pressure is varied in the absence of external stress. To capture effects of mineral distribution around pores, we simulated mismatches between a pore's skeletal stiffness and the surrounding matrix and determined that for a given strain soft pores relative to the bulk material experience greater permeability evolution than pores that are stiff relative to the surrounding matrix. While soft pores experience greater closure than stiff pores for a given applied

stress, they also experience a greater amount of dilation when pore pressure increases. This highlights that while some shale basins such as the Marcellus can experience large permeability drops relative to other basins given the same production conditions, pressure maintenance may be the most important tool to preserve permeability.

We compare the permeability response of Marcellus shale to Wolfcamp shale under changing strain to explore differences in pore structure between them. This work highlights that while magnitude of strain for a given stress is determined predominantly through a shale's mineral composition, the response of transport properties to a given strain are dependent on fracture spacing, fracture geometry, and mineral distribution around pores. We dynamically stress samples of Marcellus and Wolfcamp shales and observed levels of compaction, creep, and permeability evolution. We characterize the differences between the two shales using bulk mineralogy, SEM imaging with elemental analysis, and the cubic law for permeability evolution. We find that the Marcellus shale is comprised predominantly of clays that leads to more deformation when stressed than the Wolfcamp shale which is composed predominantly of quartz and calcite. The level of creep and compaction are directly related to the amount of clay in each shale sample. Modifications to the cubic law for fluid flow reveal that Marcellus shale has a lower fracture density than the Wolfcamp shale, that the pore geometry more closely resembles slit-like pores, and that the mineral distribution around the pore space is soft compared to the Wolfcamp shale. These differences cause the Marcellus shale to experience much greater permeability reduction under the same compressive strain than the Wolfcamp. The result of our study is a unique strain-driven model to capture permeability evolution in shale due to differences in pore structure.

We show that nitrogen flooding can double matrix permeability of gas shales. In laboratory experiments, nitrogen gas increased permeability in the bedding-parallel and bedding-

perpendicular directions by 206% and 234%, respectively. Experiments are performed at constant stress, pore pressure, and temperature. We build a model to show that the permeability enhancement is controlled by the sorptive strain, pore geometry, and the spacing-to-aperture ratio. This work addresses how an organic-poor shale can experience large permeability changes driven by sorption induced strains. We plot methane and helium permeability curves as a function of pore pressure to isolate the portion of permeability evolution controlled by sorption. We independently build strain curves to solve for the sorptive strain and find good agreement between these two methods. This work demonstrates that matrix permeability in gas shales can be doubled, which suggests that ultimate recovery can be improved as well.

We explore relationships among bulk modulus, crack density, and permeability through repetitive loading of Marcellus shale. Cumulative cyclic stressing (22-26 MPa with confinement of 24 MPa) is applied at a frequency of 0.05 Hz over 100,000 cycles. Changes in acoustic velocities are used to follow changes in dynamic bulk modulus, Poisson ratio, and crack density and to correlate these with bedding-parallel measurements of methane permeability. The shale is represented as an orthotropic elastic medium containing a dominant, noninteracting fracture set separated by thin laminae. An effective continuum model links permeability evolution to the evolution of the bulk modulus and crack density. Bulk modulus is linearly related to crack density by a scaling parameter representing rock fabric and fracture geometry. The Poisson ratio and bulk modulus of the intact, uncracked shale are deduced from our data. We propose a method for tracking permeability evolution of finely laminated shale using acoustic waves.

TABLE OF CONTENTS

List of Figures	viii
Chapter 1 The Effects of Mineral Distribution, Pore Geometry, and Fracture Spacing on Permeability Evolution in Gas Shales	1
Abstract	1
Introduction	2
Model Description	5
Results and Discussion	10
Uniaxial Strain Results	11
Incorporating Pore Geometry	14
Varying Pore Pressure Results	17
Incorporating Pore Geometry	20
Summary and Conclusion	22
References	24
Chapter 2 A Strain Based Approach to Calculate Disparities in Pore Structure between Shale Basins during Permeability Evolution	28
Abstract	28
Introduction	29
Characterization Techniques	33
SEM Imaging	34
Mineralogy Data	36
Time Dependent Compaction Data	39
Permeability Evolution with Strains	41
Characterization Using the Cubic Law	41
Fracture Spacing	42
Pore Geometry	44
Mineral distribution around the pore space	47
Integrating all variables	48
Conclusion	50
References	51
Chapter 3 Permeability Enhancement in Gas Shale due to Nitrogen Flooding	55
Abstract	55
Introduction	55
Methods	57
First Experimental Set	57
Second Experimental Set	58
Results	58
Resolving Sorptive Strain	59
Solving for sorption-induced permeability evolution	60
Nitrogen Flooding Experiments	62
Discussion	65
Lowering the partial pressure of methane causes desorption	65

Langmuir-type curves vs. BET-type curves	66
Alternative methods	66
Conclusion	67
References	68
Chapter 4 Relationships between Mechanical and Transport Properties in Shale	71
Abstract	71
Introduction	71
Methods	73
Results	74
Evolution of material properties over time	75
Evolution of permeability plotted against changing material properties	75
Relationship between bulk modulus, crack density, and intact Poisson ratio	77
Discussion	78
Finding the unknowns K and ν	78
Relating crack density to permeability	79
Conclusion	80
References	82

LIST OF FIGURES

- Figure 1-1: The simulation study focused on bands of material surrounding 2D pore spaces with an aspect ratio of 1/3. Figure 1-1a shows the schematic of each square. The size of the ellipse and the dimensions of the surrounding band were not changed as the squares were enlarged. The material stiffness of the band was varied between 10^7 Pa to 10^{13} Pa while the matrix stiffness was kept constant at 10^{10} Pa. Squares were created with increasing side length such that the spacing to aperture ratio s/b varied from 5 to 10^4 . Two configurations were tested. The first was uniaxial strain applied to the top face of the square and is pictured in 1-1b. The second was incremental increases in pore pressure with zero displacement along all exterior boundaries and is pictured in 1-1c.6
- Figure 1-2: Pore compressibility vs aspect ratio shows that pore compliance increases by an order of magnitude once α becomes less than 0.20, an aspect ratio b/a of 1/5. Shown are four curves representing different shear moduli.7
- Figure 1-3: Permeability evolution with changing aspect ratio. In this plot, the external stress is held constant such that there is no additional bulk strain. This shows that for lower aspect ratios the bulk strain is concentrated around the pore space. The cases shown are where the aspect ratio of fractures is held constant under hydrostatic stress (blue) and where deformation only occurs in along the minor semi-axis b (orange).....9
- Figure 1-4: db/u vs. α shows that as pores become more compliant, the bulk strain becomes concentrated in the pore space. The right-hand plot shows the same data in a log scale. As spacing between fractures increases they become less compliant, as is seen by the additional reduction in aspect ratio required to achieve the same strain distribution per fracture. In all cases, as α becomes much less than unity, 100% of the bulk deformation is accommodated by fracture closure..... 10
- Figure 1-5: Change in permeability k/k_0 vs. K_{sk}/K_m shows that as pore stiffness increases, aperture closure decreases. All curves are at a constant strain ϵ of $2e^{-3}$ and each curve represents a different s/b . The right-hand plot shows k/k_0 on a logarithmic scale..... 12
- Figure 1-6: Aperture closure with varying skeletal stiffness at constant fracture spacing. Curves show iso-strains. When K_{sk}/K_m is very small, aperture closure is close to constant as it is controlled by the matrix stiffness K_m which is constant throughout the simulation at 10 GPa. As the pore's skeletal band becomes stiffer, it exerts its own influence, resulting in a decreased level of aperture closure for each strain. As the band's stiffness becomes much larger than the matrix stiffness, the strain becomes distributed within the matrix instead of the pore space, as seen when K_{sk}/K_m is much greater than 1. Figure 1-6b shows that when permeability evolution k/k_0 is normalized to K_{sk}/K_m of 1.0, all curves overprint each other and collapse to a single line. This suggests that permeability evolution relative to changes in mineral distribution around pores is independent of strain. 13
- Figure 1-7: Aperture closure with increasing external strain. As spacing between fractures increases, aperture closure also increases. 14
- Figure 1-8: Permeability evolution normalized to K_{sk}/K_m of 1.0. Figure 1-8a shows a 3D heat map of k/k_0 with changing aspect ratio b/a , fracture spacing s/b , and mineral stiffness ratio K_{sk}/K_m . It shows that the aspect ratio is the most influential parameter on k/k_0 . Figure 1-8b shows a 2D heat map of k/k_0 for a cross plot of aspect ratio vs. K_{sk}/K_m . For the case of

external stress, stiffer pore material and larger aspect ratios result in higher permeability as seen in the top right red portion of 8b. Figure 1-8c shows K_{sk}/K_m vs. s/b . For this configuration, spacing had minimal impact on k/k_0 . 8d shows aspect ratio vs. fracture spacing. As s/b increased, permeability also decreased. 15

Figure 1-9: Expanded simulation results to include the effect of spacing as strain increases. The bottom row shows explicitly that as strain increases from left to right, permeability is reduced at higher spacings. This suggests that in shale reservoirs where the s/b ratio is high, permeability evolution may be very sensitive to additional strains brought about by pressure depletion or drilling activities. 16

Figure 1-10: Aperture dilation $\Delta b/b$ with varying skeletal stiffness. All data are captured at a constant pore pressure of 60 MPa, and each curve represents a different spacing to aperture ratio s/b . It can be seen that s/b exerts almost no influence over fracture dilation. The first region of the plot, where K_{sk}/K_m is between 10^{-3} to approximately 10^{-1} is controlled by the matrix stiffness. The middle portion of the plot with K_{sk}/K_m between 10^{-1} to 10^1 represents a transition where both the matrix stiffness and the skeletal stiffness exert influence over the aperture dilation. The final third of the plot where K_{sk}/K_m is between 10^1 to 10^3 is controlled by the skeletal stiffness. 17

Figure 1-11: Aperture dilation with varying K_{sk}/K_m for three different pore pressures..... 19

Figure 1-12: Aperture dilation with varying pore pressure for different spacings. The three regions of Figure 1-10 are shown here, with mineral stiffness around the pore increasing from left to right. In the middle case K_{sk} is equal to K_m , showing a general trend separate from stiffness mismatches..... 19

Figure 1-13: Aperture dilation with increasing pore pressure for different skeletal stiffness ratios. The softest fracture experienced the most dilation..... 20

Figure 1-14: Plot 1-14a shows a 3D heat map of aperture dilation with changes in aspect ratio b/a , pore mineral stiffness K_{sk}/K_m , and fracture spacing s/b . Figure 1-14b shows that softer pores experience greater aperture dilation as pore pressure is increased than do stiffer pores. We note that the solution does not change with spacing, as is confirmed in Figure 1-14c and 1-14d. 21

Figure 2-1: SEM images of Marcellus and Wolfcamp shales. Each row shows (from left to right) a backscatter image, calcium content, aluminum content, and silicon content as proxies for calcite, clays, and quartz. In the case of the Marcellus images (top two rows), the predominant mineral constituent is clay. In the Wolfcamp, the predominant mineral is calcite with clays surrounding large calcite grains. This suggests that the Marcellus is likely to be typified as soft pores surrounded by a stiffer matrix and the Wolfcamp as stiffer pores surrounded by a soft matrix..... 35

Figure 2-2: Cross plots of mineralogy by weight % for Wolfcamp samples and Marcellus samples. Figure 2-2a displays clay content vs. quartz content and shows that the Marcellus typically has higher clay composition. Figure 2-2b displays clay content vs. carbonate content. Figure 2-2c displays quartz content vs. carbonate content and shows that the Wolfcamp samples have higher quartz composition. Figure 2-2d shows quartz + clay vs. carbonate content. All values for both basins fall along a straight line. Figure 2-2e displays

quartz + carbonate vs. clay and shows that the Wolfcamp is predominantly quartz and carbonates whereas the Marcellus is predominantly clay. This suggests a mismatch in mineral distribution around pores. Figure 2-2f displays clay + carbonate content vs. quartz content.....38

Figure 2-3: Elastic moduli of Wolfcamp samples with varying mineralogy. E, G, and K all decrease with increasing clay content (LHS) and decreasing carbonate content (RHS). 39

Figure 2-4: Compaction after loading (left) is related to % clay content (right).39

Figure 2-5: Marcellus shale samples creep during permeability measurements, whereas Wolfcamp shale samples do not. On the LHS permeability is plotted against pore pressure. The blue curve representing helium should be monotonically increasing due to poromechanical expansion, as is seen on the RHS for the Wolfcamp sample. The downward shift of the curves on the LHS is due to time dependent compaction throughout the experiment. The Marcellus sample is 50% clay and 38% quartz, whereas the Wolfcamp sample is 38% clay and 46% quartz. Both are 3% organic matter, which is seen in the adsorptive permeability loss between the curves for each sample.40

Figure 2-6: The same magnitude of strain in Marcellus samples produce very large permeability loss compared to the same level of strain in Wolfcamp samples.41

Figure 2-7: As s/b increases, permeability is reduced at the same strain. The Marcellus shale permeability data fits a fracture spacing of approximately 1500, whereas the Wolfcamp sample fits a spacing of 50. In this figure, no other influences are considered. The fracture spacing will be lower once pore geometry and mineral stiffness are included later.42

Figure 2-8: Calculated fracture spacing using permeability and strain data in Equation 10 with a Poisson ratio of 0.22. In the absence of other influences, the Marcellus has a high spacing over 10^3 whereas the Wolfcamp is approximately 50.44

Figure 2-9: Fracture length to spacing a/s . Both equation 19 and equation 23 are shown.....46

Figure 2-10: Calculated initial aspect ratio for both the Marcellus and Wolfcamp samples. ..47

Figure 2-11: Changing aperture with varying pore mineral stiffness. Results are normalized to K_{sk}/K_m equal to 1, and show that if a grain mismatch creates a pore mineral stiffness less than the surrounding matrix stiffness, additional aperture is lost. The results are independent of strain.48

Figure 2-12: Experimental data for permeability and strain plotted with equation 28 for the Marcellus and Wolfcamp basins. The values used to match the Marcellus data were s/b_0 equal to 700, α equal to $7e^{-3}$, and K_{sk}/K_m equal to 0.7. The values used to match the Wolfcamp data were s/b_0 equal to 40, α equal to $6e^{-2}$, and K_{sk}/K_m equal to 1.0.....50

Figure 3-1: Strain vs. pore pressure for helium and methane. Subtracting the helium strain data from the methane strain data and fitting a Langmuir-type strain curve yields a Langmuir pressure P_L of 7 MPa and a Langmuir strain ϵ_L of 2.75×10^{-4}60

Figure 3-2: Solving for sorptive permeability evolution for processes in parallel. The light and dark blue dots represent the sorptive data points when calculated in series and in parallel, respectively—for the pressure range studied these values are very similar. The red regression curve is for a Langmuir-type permeability evolution with the Langmuir pressure as 7 MPa.....62

Figure 3-3: Normalized pressure decay α/α_0 . As N_2 infiltrates the sample, α increases.63

Figure 3-4: Normalized permeability evolution k/k_0 . Permeability increased 203% in the bedding-parallel direction and 236% in the bedding-perpendicular direction64

Figure 4-1: Evolution of material properties over time. The crack density is plotted on Cartesian axes while the permeability is plotted on semi-log axes: crack density evolution scales with the permeability evolution.....75

Figure 4-2: Mechanical properties plotted against permeability evolution. Figure 4-2a (top-left) shows permeability reduction as crack density decreases, largely driven by changes in fracture aperture. Figure 4-2b (bottom-left) shows bulk modulus increasing as permeability decreases, indicating that mechanical stress cycling led to a reduction in both the fracture length and fracture aperture. Figures 2c and 2d (V_p top-right and V_s bottom-right, respectively) show the change in acoustic wave speeds as permeability was reduced.76

Figure 4-3: Bulk modulus vs. crack density and Poisson ratio. The data indicate linear relationships and show the values of the intact bulk modulus and intact Poisson ratio. Interchanging the axes would show that the bulk modulus and crack density parameter are related through Equation (5).77

Figure 4-4: Measured and predicted permeability evolution plotted against crack density evolution ϵ/ϵ_0 (4a) and time (4b). The predicted permeability is Equation (12). Figure 4-4a has no spread compared to the scatter of the measured permeability. Figure 4-4b shows that the predicted permeability has more spread than the measured permeability when plotted versus time, although the trend lines are very close to each other.80

Chapter 1

The Effects of Mineral Distribution, Pore Geometry, and Fracture Spacing on Permeability Evolution in Gas Shales

Abstract

We modeled the effects of fracture spacing, aspect ratio, and pore stiffness on the permeability evolution of an ellipsoid crack under uniaxial stress and varying pore pressure. We found that rocks undergoing identical compressional strain and pore pressure can undergo significantly different magnitudes of fracture closure or dilation based on these three variables. This is especially important in gas shales, where nano-porosity is challenging to characterize and heterogeneity between basins has led to disparate permeability responses in the field and in the laboratory. We found that the aspect ratio is the most sensitive parameter influencing pore compressibility. The fracture spacing becomes important when external stress is applied, but it has no significant effect when pore pressure is varied in the absence of external stress. To capture effects of mineral distribution around pores, we simulated mismatches between a pore's skeletal stiffness and the surrounding matrix and determined that for a given strain soft pores relative to the bulk material experience greater permeability evolution than pores that are stiff relative to the surrounding matrix. While soft pores experience greater closure than stiff pores for a given applied stress, they also experience a greater amount of dilation when pore pressure increases. This highlights that while some shale basins such as the Marcellus can experience large permeability drops relative to other basins given the same production conditions, pressure maintenance may be the most important tool to preserve permeability.

Introduction

Shales are tight sedimentary rocks that consist—among others—of organic matter, quartz cement and silt, carbonates, pyrite, feldspar and various clays such as illite and smectite. The highly heterogenous nature of shale has made its response to changes in effective stress challenging to predict in the lab and in the field. Due to variations in depositional environment, mineralogy, burial history and thermal maturation the internal pore structure of shale is complex. Pore channels in shale are described as nanometer to micrometer wide fractures separated by finely laminated stacks of minerals (Ulm & Abousleiman 2006; Horne 2013). Permeability measurements of the intact rock range from 10^{-23} m^2 to 10^{-17} m^2 (Daigle et al., 2017). Within the matrix, there are two distinct planes for flow oriented orthogonal to bedding—the flow paths in the bedding-perpendicular direction are often typified as highly tortuous nano-sized capillary tubes (Javadpour et al., 2007; Javadpour 2009; Civan et al., 2012), whereas the flow paths in the bedding-parallel direction can be modeled as long penny-shaped cracks (Li & Elsworth, 2015; Kumar et al., 2016).

Pore channels in rocks are located near grain boundaries. The potential mismatch in material properties of the minerals surrounding a pore often leads to microcrack growth (Costin 1983). It can also create an environment in which the material properties of a pore's skeletal structure are different than the surrounding matrix. The mineral constituents of shale each have their own material properties, and the combination of mineralogy, grain orientation, and pore structure determine the bulk mechanical and transport properties of the intact shale. For organic-rich shales, pore channels residing within the organic matter are considered a substantial portion of the entire pore structure (Loucks et al., 2009). In addition to the organic matter, the clay portion of shales holds much of the remaining pore structure (Sondergeld et al., 2010; Curtis et al., 2012).

Indeed, some shales such as the Marcellus and Utica shales are predominantly composed of clays and organic matter. Other shales such as the Wolfcamp have been found to be composed of much higher amounts of quartz and carbonates, suggesting that the pores may be located in stiffer materials than in organic-rich and clay-rich basins. In contrast to clays and organic matter, minerals such as quartz, feldspars, and carbonates have rigid grains that resist mechanical compaction (Gu & Mildner, 2016). Data have been collected on the stiffness of different minerals that comprise shale and were found to vary within approximately one order of magnitude of each other (Mavko, 1998). Therefore, the difference between the response of a soft pore encased in a stiff matrix and a stiff pore encased in a soft matrix could be two orders of magnitude. Exploring the permeability evolution of such pores with varying mineral distribution is the goal of this study.

In addition to the mineral composition of its boundary, a pore's compressibility is determined by its geometry. Flow paths in shales can be described as circular tubes, ellipsoid fractures, or flat cracks (Bernabe et al., 1982; Sisavath et al., 2000; Javadpour 2009; Izadi et al., 2011). The main parameter used to differentiate these geometries is the aspect ratio α of an ellipse where b is the semi-minor axis half length, a is the semi-major axis half length, and α is b/a . An α value of unity is a circle, and as α becomes much smaller than unity it transitions from describing an ellipse to describing a flat crack. Pore compressibility and fracture density can be cast in terms of the perimeter and initial area of the ellipse, where the perimeter must be approximated and the area is πab (Budiansky & O'Connell, 1976; Tsukrov & Novak, 2002). Studies have found that pore channels in the organic portion of shale vary from nearly round patches where α is between 0.5-1.0 to thin layers where α is less than 0.05 (Sone & Zoback, 2013). Bandyopadhyay (2009) found that the optimum value of α in the Bakken shale to match the data of Vernik and Liu (1997) was 0.10. Disparities in average values of α within a basin are important, as the closing pressure

for a penny shaped crack is directly proportional to its aspect ratio (Zimmerman, 1985). The compressibility of two-dimensional pores can be modeled analytically (Savin, 1961; Zimmerman, 1986; Jasiuk, 1995). The only geometry suitable to analytical modeling in three dimensions is the penny shaped crack, which was found to be stiffer than the two-dimensional equivalent by a factor of $\pi/2$ (Walsh, 1965). In this study we will rely on two-dimensional modeling of pore compressibility: the axisymmetric nature of shale causes the three-dimensional case to reduce to the two-dimensional case when flow is studied parallel to the dominant fracture set in the bedding-parallel direction.

The third variable that affects permeability evolution in fractured media is the fracture spacing s/b , where s is the spacing between fractures and b is the fracture aperture. The inverse of the fracture spacing is b/s , which is also called the fracture density or fracture porosity. When fractures are soft compared to the surrounding matrix, the change in fracture aperture Δb can be approximated as $s*\epsilon$, where ϵ is the bulk external strain (Elsworth, 1989). Large values of s or ϵ will cause large changes in aperture. The ability to flow fluid through a fracture set is predominantly a function of the fracture aperture, and gas production is typically modelled as flow between parallel plates (Goodman, 1989). Fracture spacing is known to be related to bedding thickness (Ladeira, 1981; Narr, 1991) and the degree of rock compaction during burial (Chang et al., 2009). Spacing is often proportional to fracture aperture (Garrett & Bailey, 1977). While it will vary spatially, the spacing determined by permeability measurements will reflect an average (Narr, 1996; Ortega et al., 2006). In the case of fracture sets of various sizes and roughness, the calculated aperture will be an average aperture over the entire fracture set (Tsang & Witherspoon, 1981; Brown, 1987).

Mineral distribution around pores, pore geometry, and pore spacing should all influence permeability evolution in shales. Under the same effective stress, shales respond differently. The goal of this study is to explore the contributions of each of the above three variables to a shale's response to changes in effective stress. To that end, we created a two-dimensional simulation of a pore that captures changes in mineral stiffness, pore geometry, and pore spacing. We tested two configurations: uniaxial strain and varying pore pressure. Next, we discuss the study parameters and results.

Model Description

We used COMSOL Multiphysics to model 2D stress on squares with pore channels flowing through their centers. The 3D case essentially reduces to the 2D case. Figure 1-1a shows a schematic of the model geometry. A square with side length s was created and an ellipse with aspect ratio 1/3 was removed from the center. A second ellipse was created and is pictured in Figure 1-1 as a red band surrounding the pore space. This band was given a different material stiffness than the surrounding matrix pictured in grey in Figure 1-1. The matrix stiffness K_m was set constant at 10 GPa. Assigning the “skeletal stiffness” as K_{sk} and the matrix stiffness as K_m , we were able to create a dimensionless ratio K_{sk}/K_m in order to capture changes in aperture Δb at constant spacing and external stress while varying K_{sk}/K_m . We varied K_{sk}/K_m from 10^{-3} to 10^3 . We built squares with increasing side length s from 5 to 10^4 . Figure 1-1b illustrates the first configuration in which uniaxial stress was applied normal to the semi-major axis of the ellipse with the bottom face of the square fixed in space. Stress was varied such that it created a bulk strain that varied between 0 to $3.5e^{-3}$. The right and left sides of the square were allowed to deform freely. The result was a deformed square with a partially closed pore channel. At each stress, the change in ellipse aperture Δb was measured. In the second configuration illustrated in Figure 1-1c, all four exterior boundaries were fixed in space and pore pressure was applied as a traction

normal to the boundary of the pore. Pore pressure was varied between 0 to 100 MPa. For both configurations, the only aspect ratio modeled was 1/3. We applied an analytical solution to incorporate changing aspect ratio into the model results.

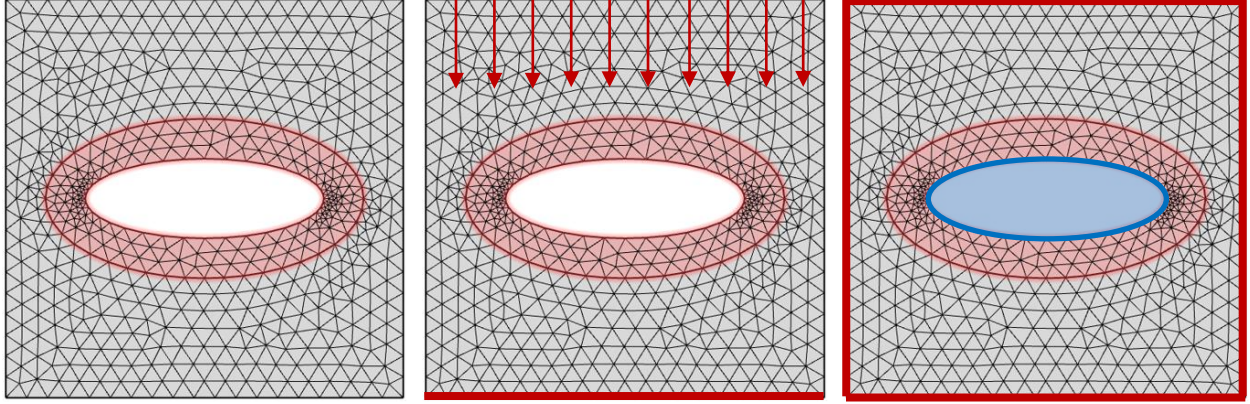


Figure 1-1: The simulation study focused on bands of material surrounding 2D pore spaces with an aspect ratio of 1/3. Figure 1-1a shows the schematic of each square. The size of the ellipse and the dimensions of the surrounding band were not changed as the squares were enlarged. The material stiffness of the band was varied between 10^7 Pa to 10^{13} Pa while the matrix stiffness was kept constant at 10^{10} Pa. Squares were created with increasing side length such that the spacing to aperture ratio s/b varied from 5 to 10^4 . Two configurations were tested. The first was uniaxial strain applied to the top face of the square and is pictured in 1-1b. The second was incremental increases in pore pressure with zero displacement along all exterior boundaries and is pictured in 1-1c.

Changing Aspect Ratio

Fracture compressibility can be cast as

$$C_{pc} = \frac{2(1-\nu_m)}{G_m} \left(\alpha + \frac{1}{\alpha} \right) \quad (1)$$

where ν_m and G_m are the Poisson ratio and shear modulus of the intact rock, respectively (Walsh, 1965). As α becomes much smaller than unity, the equation can be simplified as

$$C_{pc} = \frac{2(1-\nu_m)}{G_m \alpha} \quad (2)$$

We plot equation (1) below to show pore compressibility as it varies with aspect ratio. We assume an intact Poisson ratio of 0.20 and shear modulus ranging from 1 to 1000 GPa. For α between 0.20 and 1.0, the pore compressibility is roughly constant. At α less than 0.20, the pore compressibility

begins to increase dramatically, suggesting that shales with aspect ratios lower than 0.20 will experience significantly greater pore closure for a given compressive strain than shales with aspect ratios higher than 0.20.

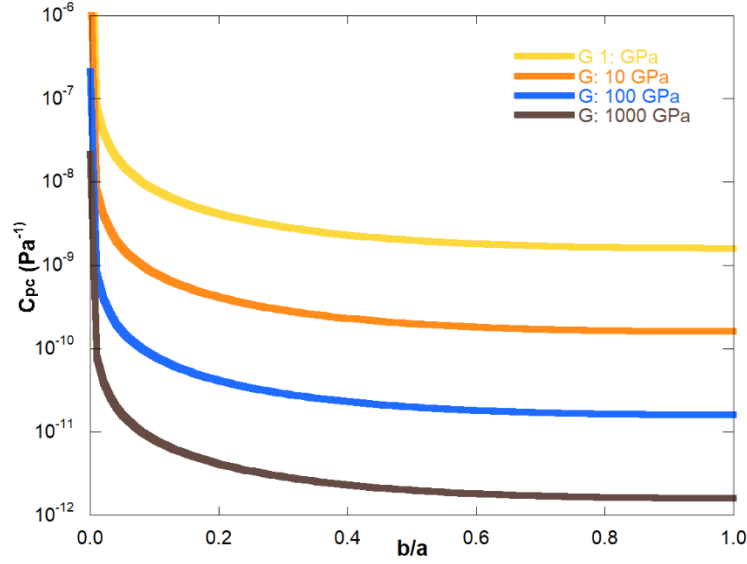


Figure 1-2: Pore compressibility vs aspect ratio shows that pore compliance increases by an order of magnitude once α becomes less than 0.20, an aspect ratio b/a of 1/5. Shown are four curves representing different shear moduli.

Strain in the pore space can be found as

$$\varepsilon_{pc} = \sigma' C_{pc} \quad (3)$$

We invoke the constraint that under hydrostatic stress the aspect ratio α can be assumed constant—a change in one semi-axis should be met by the same change in the other semi-axis due to equal stresses in all directions. Mathematically, this is

$$\frac{b}{a} = \text{const.} \rightarrow \frac{b(1 - \frac{\Delta b}{b})}{a(1 - \frac{\Delta a}{a})} = \frac{b}{a} \quad (4)$$

Therefore, the change in area ΔA of a 2D ellipse should be

$$\Delta A = \pi \Delta a \Delta b \rightarrow \Delta A = \pi \left(1 - \frac{\Delta a}{a}\right) a \left(1 - \frac{\Delta b}{b}\right) b \quad (5)$$

The strain in the pore space can therefore be recast as

$$\varepsilon_{pc} = \frac{A-\Delta A}{A} \rightarrow \varepsilon_{pc} = 1 - \left(1 - \frac{\Delta b}{b}\right)^2 \quad (6)$$

Combining (3) and (6) we have

$$\varepsilon_{pc} = \Delta\sigma' C_{pc} = 1 - \left(1 - \frac{\Delta b}{b}\right)^2 \quad (7)$$

Since

$$\frac{k}{k_0} = \left(1 - \frac{\Delta b}{b_0}\right)^3 \quad (8)$$

Equation (7) can be recast as

$$\frac{k}{k_0} = \left(1 - \Delta\sigma' C_{pc}\right)^{\frac{3}{2}} \quad (9)$$

In the case that the aspect ratio is not held constant, $\Delta\alpha$ can be modeled as occurring only along the minor semi-axis: aperture closure. In this case, the change in area of the ellipse is

$$\Delta A = \pi ab \left(1 - \frac{\Delta b}{b}\right) \quad (10)$$

and the pore strain becomes

$$\varepsilon_{pc} = \frac{\pi ab - \pi ab \left(1 - \frac{\Delta b}{b}\right)}{\pi ab} = 1 - \left(1 - \frac{\Delta b}{b}\right) \quad (11)$$

It can be readily shown that equation (9) becomes

$$\frac{k}{k_0} = \left(1 - \Delta\sigma' C_{pc}\right)^3 \quad (12)$$

in the case of changing aspect ratio due to a change in aperture b .

We normalize the permeability in equations (9) and (12) to an aspect ratio α of 1/3 in order to match the remainder of the simulation. Figure 1-1-3 shows the change in permeability as α decreases under constant stress. At aspect ratios greater than 0.20, permeability loss is small. However, as α continues to decrease and pore compressibility continues to increase, the permeability loss becomes much larger. This is in agreement with Figure 1-2, which shows that the main driver of the additional permeability loss at constant external stress is the pore

compressibility. It can be seen from Figure 1-3 that, if the only difference between two shales is that one has an average aspect ratio of 0.20 and the other an aspect ratio of 0.02, the permeability loss at constant effective stress goes from 0.98 to 0.50.

In both scenarios, the curves reach the lower bound of k/k_0 as α approaches 10^{-2} . Examining equations (9) and (12) shows that this occurs when $\sigma' C_{pc}$ becomes greater than 1. As the applied effective stress is 10^7 Pa, the lower bound is reached when C_{pc} is 10^{-7} Pa⁻¹. This is a mathematical constraint to the equations, and all values of α that take C_{pc} higher than this physical limit should be interpreted as causing complete pore closure.

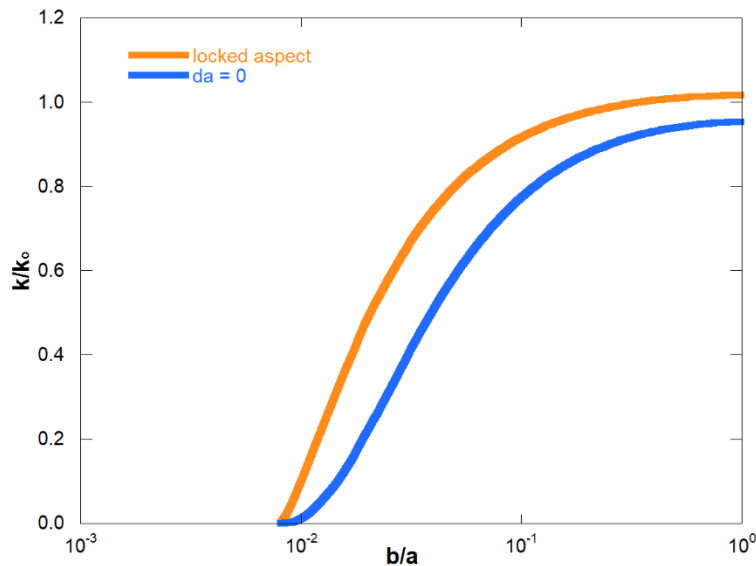


Figure 1-3: Permeability evolution with changing aspect ratio. In this plot, the external stress is held constant such that there is no additional bulk strain. This shows that for lower aspect ratios the bulk strain is concentrated around the pore space. The cases shown are where the aspect ratio of fractures is held constant under hydrostatic stress (blue) and where deformation only occurs in along the minor semi-axis b (orange).

As stress is constant, the additional aperture closure at lower aspect ratios is due to strain becoming concentrated around the pore space. Figure 1-4 shows the hypothetical distribution of strain for a shale as s/b varies. The applied external stress is 10 MPa and the bulk stiffness is 1 GPa. Therefore, for all α 's, the bulk strain is 10^{-2} . However, as α decreases the fracture closure

increases to the point where the entirety of the bulk deformation is accommodated in the pore space.

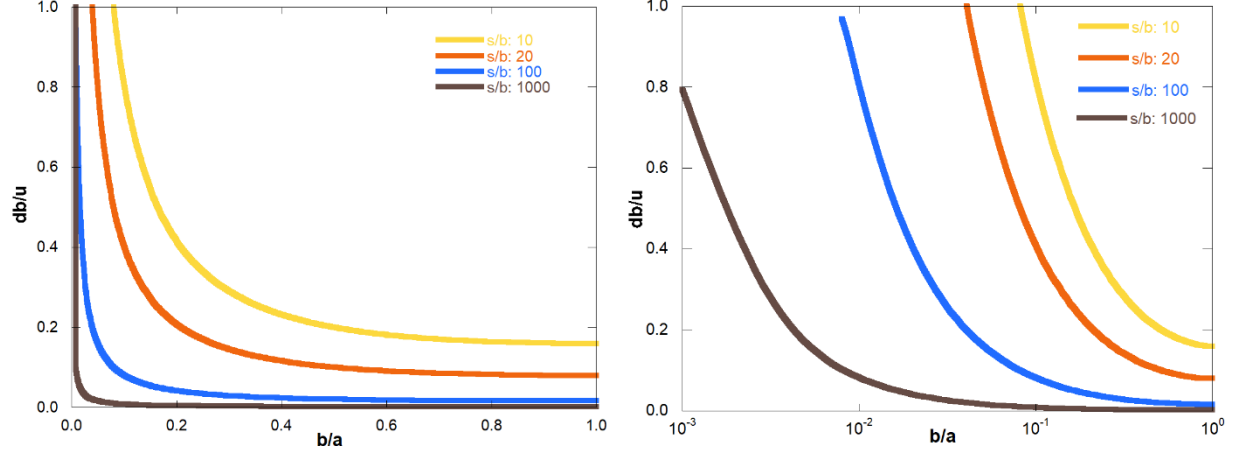


Figure 1-4: db/u vs. α shows that as pores become more compliant, the bulk strain becomes concentrated in the pore space. The right-hand plot shows the same data in a log scale. As spacing between fractures increases they become less compliant, as is seen by the additional reduction in aspect ratio required to achieve the same strain distribution per fracture. In all cases, as α becomes much less than unity, 100% of the bulk deformation is accommodated by fracture closure.

Results and Discussion

With anticipated results including changes in aperture Δb with varying strain, fracture spacing, pore skeletal stiffness and pore pressure, we completed a simulation of bulk deformation of a series of 2D squares representing ellipsoid fractures in rock. We formulated an analytical solution for changes in permeability with decreasing aspect ratio α which can extend the results in both configurations of the simulation. In the first configuration, we applied a uniaxial stress to the top face of each square and measured changes in aperture Δb while varying skeletal stiffness K_{sk} . We combine the results of the aspect ratio study to complete our set of variables, which for the first configuration are $\{\epsilon, K_{sk}/K_m, s/b, \alpha, k/k_0\}$. In the second configuration we held exterior boundaries at zero displacement and applied an increasing pore pressure from 0 to 100 MPa within the ellipsoid pore. We measured changes in aperture Δb while varying skeletal stiffness K_{sk} . We

combine the results of the aspect ratio study to complete our set of variables, which for the second configuration are $\{P_p, K_{sk}/K_m, s/b, \alpha, \Delta b/b\}$. Finally, we observe that the pore compression data and the pore dilation data represent competing processes in the subsurface and we locate regions where each variable exerts the dominant influence on net aperture response.

Uniaxial Strain Results

We convert changes in aperture Δb to permeability evolution k/k_0 for various combinations of the simulation variables in Figures 5-7. For all plots showing k/k_0 , permeability has been normalized to the value of k_0 when K_{sk}/K_m is equal to unity. For k/k_0 values less than one, additional permeability is lost relative to the base case of K_{sk}/K_m equal to one. Similarly, for k/k_0 values greater than one, permeability is enhanced relative to the base case. In Figure 1-5 we see that for a given strain, permeability remained almost constant when K_{sk} was much lower than K_m . As fractures become stiffer than the surrounding matrix such that K_{sk}/K_m is greater than unity, strain becomes distributed further away from the fractures and permeability increases relative to the base case. In this way, any given strain will cause a large permeability loss in the case of soft fractures relative to the surrounding matrix or negligible permeability loss in the case of stiff fractures relative to the surrounding matrix. Figure 1-5 shows four different curves representing different fracture spacing. As s/b increases, permeability evolution reaches a limit corresponding to maximum fracture closure for the given strain. The permeability evolution for a fracture spacing of 1000 overprints the s/b value of 100 because the closure limit has been reached. In these plots, strain is constant for all curves at $2e^{-3}$. The left-hand plot shows permeability evolution on semi-log axes while the right-hand plot is in log-log axes.

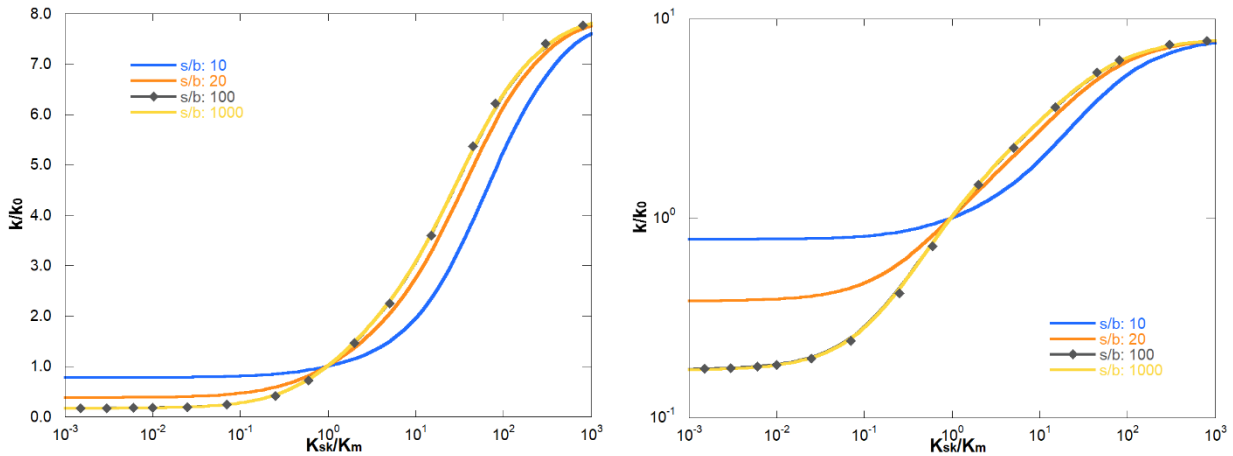


Figure 1-5: Change in permeability k/k_0 vs. K_{sk}/K_m shows that as pore stiffness increases, aperture closure decreases. All curves are at a constant strain ε of $2e^{-3}$ and each curve represents a different s/b . The right-hand plot shows k/k_0 on a logarithmic scale.

Figure 1-6 shows aperture closure with varied K_{sk}/K_m at constant fracture spacing—in this case, s/b is 100. As strain increases, the magnitude of aperture closure also increases. As in Figure 1-5, when fractures are soft compared to the surrounding matrix, aperture closure is almost constant for each strain. This is due to the fracture closure being controlled by the matrix stiffness. Once the skeletal stiffness K_{sk} approaches K_m , it begins to exert a separate influence and Δb decreases. As each curve is at constant bulk strain, the decreasing nature of each curve as K_{sk} becomes much stiffer than K_m suggests that the strain becomes distributed in the matrix instead of around the fracture itself. Figure 1-6b shows permeability evolution with all curves normalized to k_0 at K_{sk}/K_m equal to unity. All curves collapse to the same curve independent of strain, suggesting that at constant strain the permeability evolution is dependent on the mineral distribution around the pore space. The difference between the permeability evolution at a K_{sk}/K_m value of 10^{-1} and 10^1 is more than an order of magnitude and could represent the difference between quartz cemented pores in a clay matrix and clay pores surrounded by a quartz matrix.

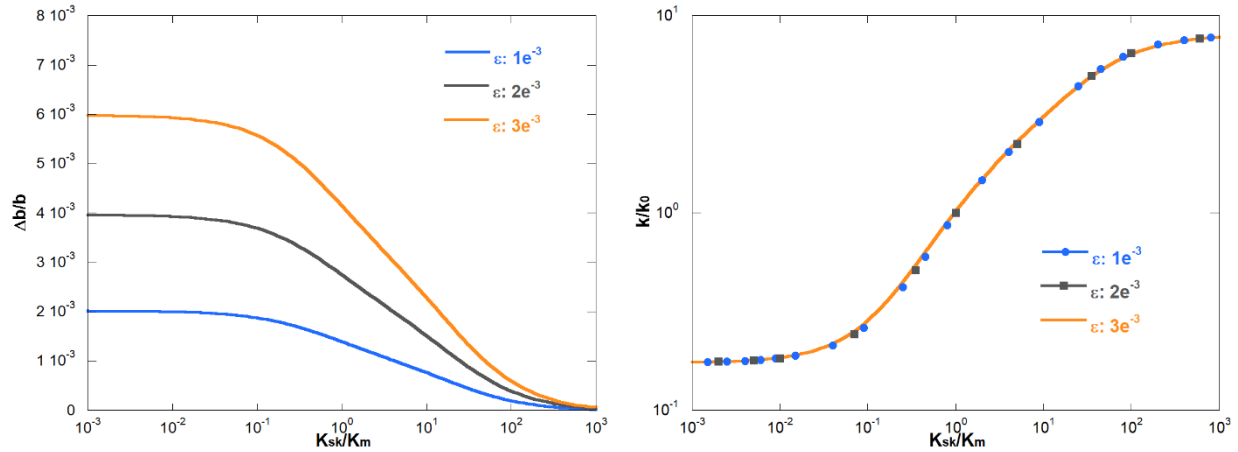


Figure 1-6: Aperture closure with varying skeletal stiffness at constant fracture spacing. Curves show iso-strains. When K_{sk}/K_m is very small, aperture closure is close to constant as it is controlled by the matrix stiffness K_m which is constant throughout the simulation at 10 GPa. As the pore's skeletal band becomes stiffer, it exerts its own influence, resulting in a decreased level of aperture closure for each strain. As the band's stiffness becomes much larger than the matrix stiffness, the strain becomes distributed within the matrix instead of the pore space, as seen when K_{sk}/K_m is much greater than 1. Figure 1-6b shows that when permeability evolution k/k_0 is normalized to K_{sk}/K_m of 1.0, all curves overprint each other and collapse to a single line. This suggests that permeability evolution relative to changes in mineral distribution around pores is independent of strain.

In Figure 1-7 the change in aperture $\Delta b/b$ is plotted with increasing external strain for different fracture spacings. As additional strain is applied, a commensurate amount of fracture closure occurs. As the spacing to aperture ratio s/b increases, each fracture becomes more compliant and more of the strain is distributed around the pore space up to an irreducible aperture closure limit where curves begin to overprint each other. As fractures become closer together, such as the blue curve representing s/b equals 5, they become less compliant as the strain can be distributed over more fractures, resulting in less net closure for each fracture.

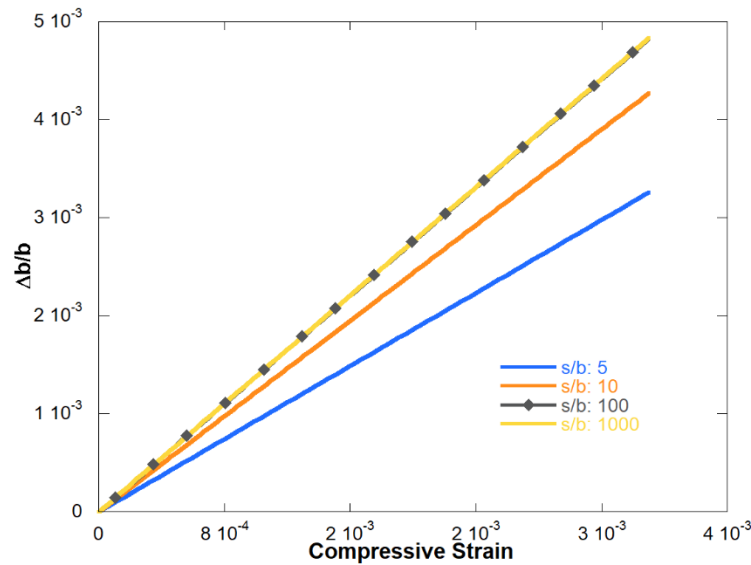


Figure 1-7: Aperture closure with increasing external strain. As spacing between fractures increases, aperture closure also increases.

Incorporating Pore Geometry

Results from Equation 12 were integrated into the COMSOL simulation in order to observe the influence of all three variables in conjunction with each other. Figure 1-8 shows all four combinations of the three variables with permeability evolution represented by color. In Figure 1-8a, a 3D heat map of all three variables is shown with k/k_0 in color. Figure 1-8a shows that for this configuration, spacing had the least effect on permeability while aspect ratio had the largest effect. As the aspect ratio approaches unity, pores compress less for a given strain than slit-like pores with lower aspect ratios. The aspect ratio is shown to be more important than the mineral distribution around the pore, as illustrated by variations in K_{sk}/K_m in Figures 8b and 8c. Figure 1-8b shows that while a soft pore made of clays or organics may experience additional closing, if the aspect ratio of the pore is greater than 0.10 much of the closure can be mitigated by the stiffer geometry. Figure 1-8d shows that spacing may play an important role for shales as effective stress increases, such as in drilling and completions operations or pressure depletion.

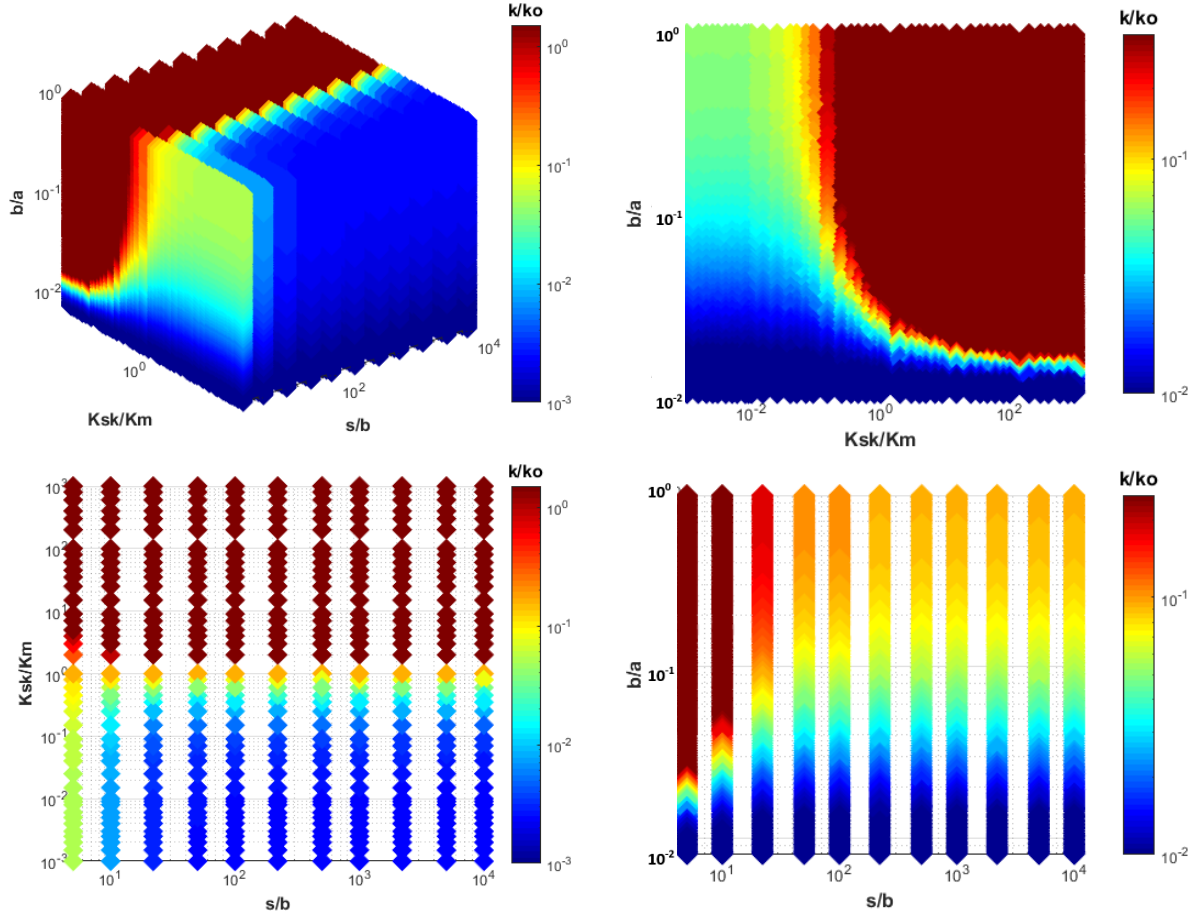


Figure 1-8: Permeability evolution normalized to K_{sk}/K_m of 1.0. Figure 1-8a shows a 3D heat map of k/k_0 with changing aspect ratio b/a , fracture spacing s/b , and mineral stiffness ratio K_{sk}/K_m . It shows that the aspect ratio is the most influential parameter on k/k_0 . Figure 1-8b shows a 2D heat map of k/k_0 for a cross plot of aspect ratio vs. K_{sk}/K_m . For the case of external stress, stiffer pore material and larger aspect ratios result in higher permeability as seen in the top right red portion of 8b. Figure 1-8c shows K_{sk}/K_m vs. s/b . For this configuration, spacing had minimal impact on k/k_0 . 8d shows aspect ratio vs. fracture spacing. As s/b increased, permeability also decreased.

To capture these effects, we expanded the simulation to include an additional analysis of spacing when fractures are soft compared to the matrix. The above represents the case in which the fracture stiffness is not much less than the surrounding matrix stiffness. If fracture stiffness is much less than matrix stiffness, Δb is $s \cdot \epsilon$. We expand the simulation by incorporating both s/b and strain in our 3D data. Using the cubic law we find that as spacing increases, the permeability results should be modified by the below equation:

$$\frac{k_1}{k_2} = \left(\frac{1 - \nu \frac{s_1}{b_0} \varepsilon}{1 - \nu \frac{s_2}{b_0} \varepsilon} \right)^3 \quad (13)$$

Results are plotted below in Figure 1-9 for four different strains. It can be seen that as the strain increases, fracture spacing becomes more important.

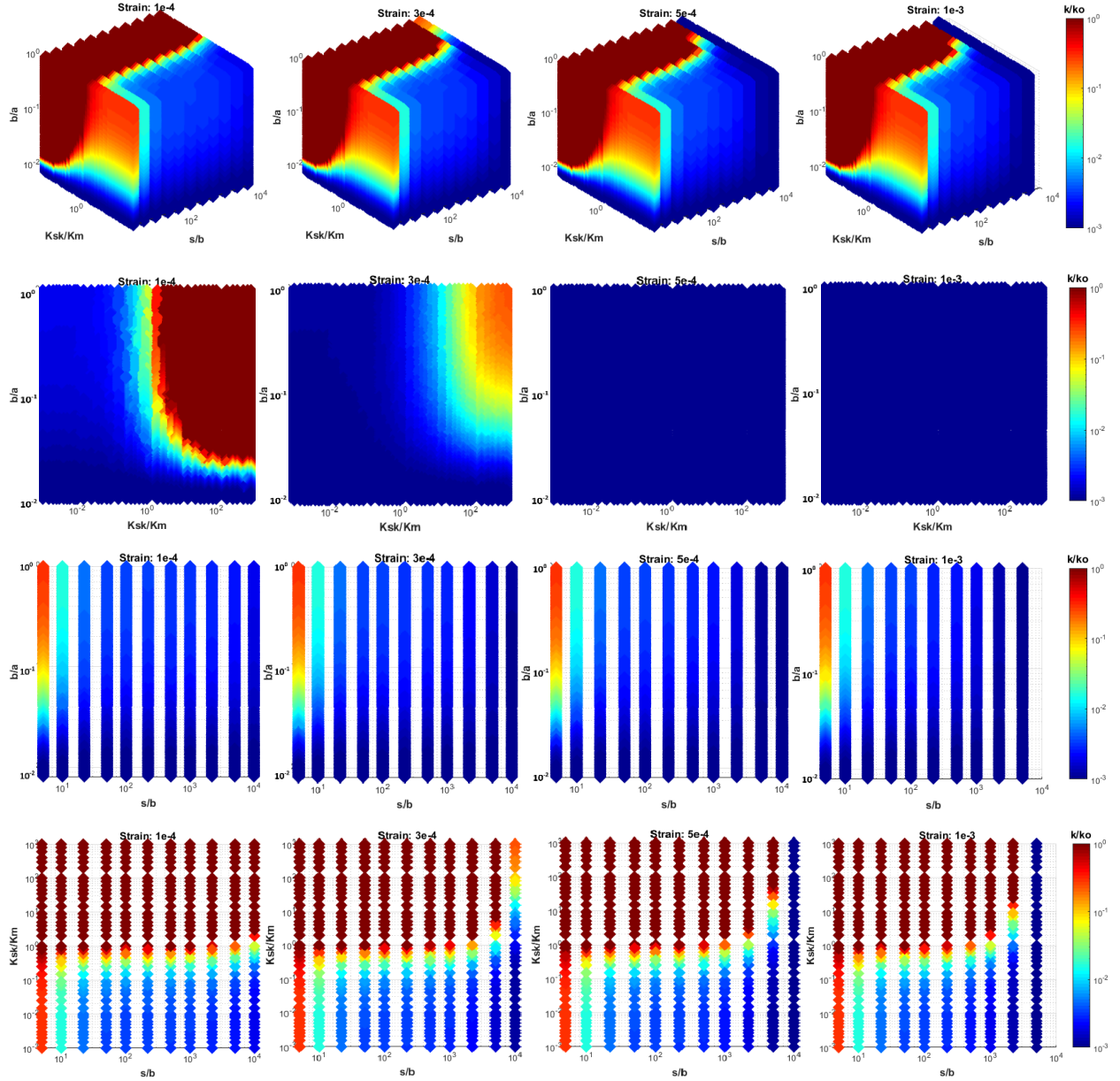


Figure 1-9: Expanded simulation results to include the effect of spacing as strain increases. The bottom row shows explicitly that as strain increases from left to right, permeability is reduced at higher spacings. This suggests that in shale reservoirs where the s/b ratio is high, permeability evolution may be very sensitive to additional strains brought about by pressure depletion or drilling activities.

Varying Pore Pressure Results

For the second configuration of the simulation, we held the exterior boundaries of a series of squares at zero displacement and varied the pore pressure within the ellipsoid pore. We varied the skeletal stiffness of the pore between 10^7 Pa to 10^{13} Pa while holding the matrix stiffness constant at 10^{10} Pa. Figures 10-13 capture the main features of each fracture's response to the pore pressure. In the case of the pore pressure study, positive Δb represents pore dilation and should be seen as a competing force to the external strain applied in the first part of the study. Both parts will be examined in tandem below, as the combination of the two reflects real world processes in the subsurface and in the lab.

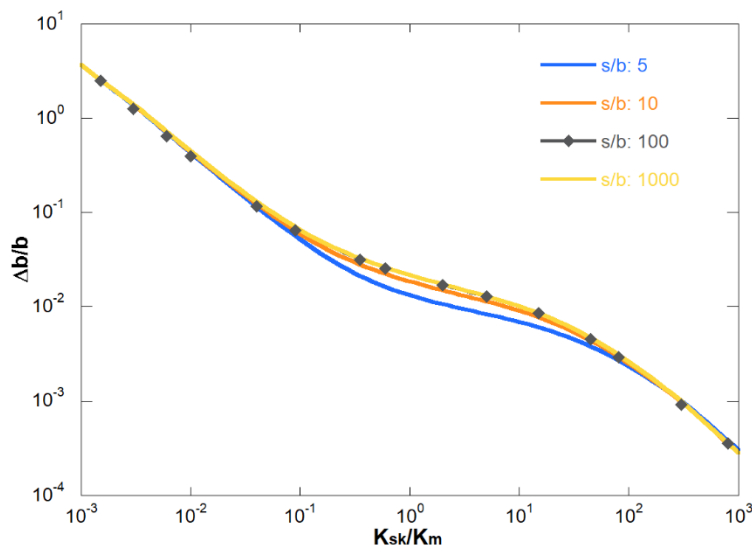


Figure 1-10: Aperture dilation $\Delta b/b$ with varying skeletal stiffness. All data are captured at a constant pore pressure of 60 MPa, and each curve represents a different spacing to aperture ratio s/b . It can be seen that s/b exerts almost no influence over fracture dilation. The first region of the plot, where K_{sk}/K_m is between 10^{-3} to approximately 10^{-1} is controlled by the matrix stiffness. The middle portion of the plot with K_{sk}/K_m between 10^{-1} to 10^1 represents a transition where both the matrix stiffness and the skeletal stiffness exert influence over the aperture dilation. The final third of the plot where K_{sk}/K_m is between 10^1 to 10^3 is controlled by the skeletal stiffness.

Figure 1-10 shows aperture dilation $\Delta b/b$ with evolving skeletal stiffness. For a given pore pressure, a rock will experience larger dilation with soft fractures than with stiff fractures. This suggests an additive competition in real world applications where pore pressure is being changed at the same time that an external stress is causing bulk strain. Notably, changing the s/b ratio does not produce significant differences as can be seen by the four curves overprinting each other. This differs from the uniaxial strain configuration where results scaled directly with each magnitude of spacing.

There are several regions within Figure 1-10. In the first region, from K_{sk}/K_m equals 10^{-3} to 10^{-1} all curves are overprinted at a linear slope that seems to be resumed in the third region where K_{sk}/K_m varies from 10^1 to 10^3 . In the first region, $K_{sk} \ll K_m$, suggesting that aperture dilation is controlled by K_m . In the third region, $K_m \ll K_{sk}$, suggesting that aperture dilation is controlled by K_{sk} . In both regions, the stiffer material controlled the magnitude of aperture dilation Δb . There is a middle region where K_{sk}/K_m is between 10^{-1} and 10^1 , such that material properties are relatively similar to each other. The inflection point is at K_{sk}/K_m equal to unity. In the first half of the middle region, where K_{sk}/K_m is between 10^{-1} and unity, the rate of aperture dilation begins to slow down as skeletal stiffness approaches the matrix stiffness. In the second half of the middle region, where K_{sk}/K_m is between unity and 10^1 , the rate of aperture dilation slows down even more as the pore skeleton becomes increasingly stiffer.

Figure 1-11 shows aperture dilation for different pore pressures with varying skeletal stiffness. For this plot, the spacing to aperture ratio is 100. As pore pressure increases, there is more dilation of the pore. While the pore pressure affects the dilation for a given K_{sk}/K_m , all pore pressures follow the same curve shape. Increasing pore pressure does not change the shape of the

$\Delta b/b$ vs. K_{sk}/K_m curve, suggesting a linear relationship between pore pressure and pore dilation. This trend is confirmed in Figure 1-12.

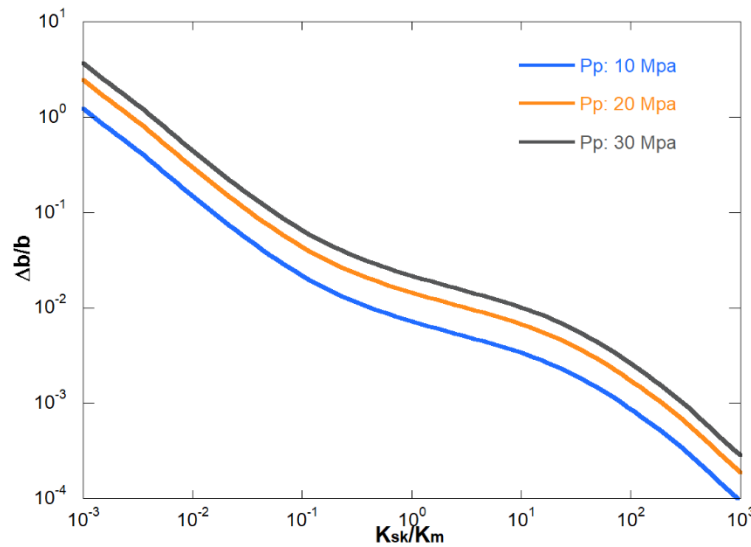


Figure 1-11: Aperture dilation with varying K_{sk}/K_m for three different pore pressures.

Figure 1-12 shows aperture dilation with increasing pore pressure. Dilation appears to follow a linear trend with pore pressure. Three scenarios are shown: the left plot, middle, and right plots are K_{sk}/K_m equal to 10^{-2} , 10^0 , and 10^2 respectively. Recalling Figure 1-10, the middle plot shows the separation of the curves when both the skeletal stiffness and matrix stiffness are influencing the dilation. The left and right plots show Region 1 and 3 from Figure 1-10, where spacing does not affect aperture dilation.

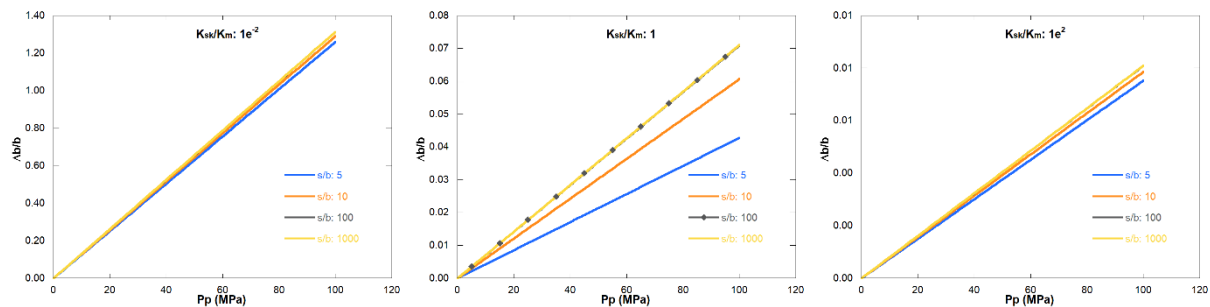


Figure 1-12: Aperture dilation with varying pore pressure for different spacings. The three regions of Figure 1-10 are shown here, with mineral stiffness around the pore increasing from left to right. In the middle case K_{sk} is equal to K_m , showing a general trend separate from stiffness mismatches.

Figure 1-13 shows increased aperture dilation with increasing pore pressure. Three curves are shown representing different K_{sk}/K_m ratios. As pores become softer, they experience larger dilation at the same pore pressure. This is the opposite of what was seen in the first configuration with uniaxial strain, suggesting that permeability loss experienced by soft pores may be mitigated by pressure management.

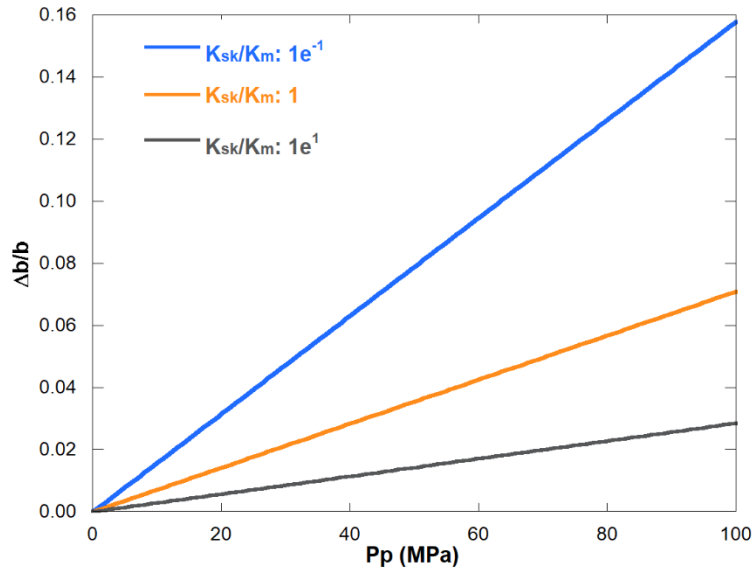


Figure 1-13: Aperture dilation with increasing pore pressure for different skeletal stiffness ratios. The softest fracture experienced the most dilation.

Incorporating Pore Geometry

We added Equation 9 to the COMSOL data and plotted 3D heat maps of all three variables for the varying pore pressure configuration. Results are shown below in Figure 1-14. As can be seen below, the most notable feature of Figure 1-14 is that in the case of varying pore pressure, the solution does not depend on fracture spacing. This is different than the uniaxial stress configuration, in which increasing strain at high values of s/b reduced permeability tremendously. Physically, an increase in pore pressure should not be influenced by fracture spacing because the deformation originates at the inside pore boundary whereas additional external stress causes a deformation that originates outside of the pore boundary. In the second case, the amount of

material available for deformation—as determined by the spacing between fractures—directly affects the amount of strain that must be accommodated by the pore space.

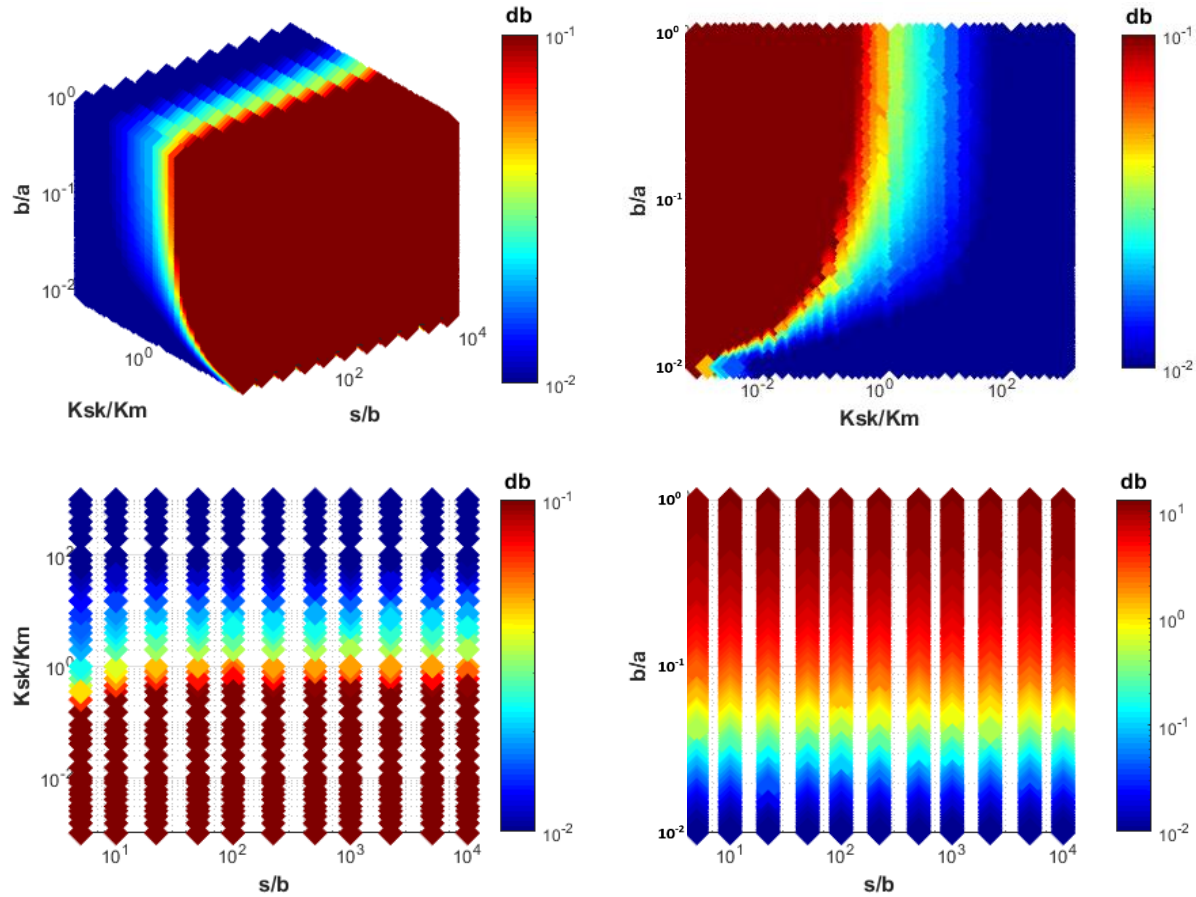


Figure 1-14: Plot 1-14a shows a 3D heat map of aperture dilation with changes in aspect ratio b/a , pore mineral stiffness K_{sk}/K_m , and fracture spacing s/b . Figure 1-14b shows that softer pores experience greater aperture dilation as pore pressure is increased than do stiffer pores. We note that the solution does not change with spacing, as is confirmed in Figure 1-14c and 1-14d.

There are several factors that could affect the distribution of minerals around the pore space. Depositional environment determines the initial porosity and connectivity. In some rocks, dissolution, migration, and precipitation of calcite can create stiff pores encased in calcite surrounded by a clay matrix. Similarly, diagenesis of smectite will release dissolved silica that can lead to quartz cementation of pores (Berger et al., 1997; Metz et al., 2005).

The effect of spacing in the uniaxial stress simulation may be understated due to the way the model was constructed. In this study, two-dimensional squares with one non-interacting pore were considered. Since the existence of nearby pores are known to increase the compressibility of a rock (Fond et al., 2001; Chalon & Montheillet, 2003), the spacing to aperture ratio s/b necessarily influences a rock's compressibility. The s/b ratio will be examined closer in the next chapter, where its role is further explored using laboratory data and analysis of the cubic law.

The measured bulk modulus of a material is a weighted average of the bulk moduli of the individual mineral components. Therefore, rocks with identical mineralogy are expected to experience the same strain under a given stress. However, the distribution of the resulting strain will be directly related to the distribution of minerals around the pores. In the Marcellus shale the porosity is believed to be concentrated in the clays and organics with stiffer components such as quartz and calcite being found in the far field region. In the Wolfcamp shale, the pore space is believed to be surrounded directly by calcite, creating a much stiffer skeletal structure for the pore channels than is found in the Marcellus. This too will be examined closer in the next chapter.

Summary and Conclusion

We simulated the effects of mineral distribution around pores (K_{sk}/K_m), pore geometry (α), and fracture spacing (s/b) on permeability evolution with changes in external stress and internal pore pressure. We found that the aspect ratio has the largest impact on both configurations. This is important for shales, as investigators report different aspect ratios for different basins. A basin like the Marcellus—consisting of slit-like pores with low aspect ratio—would see greater permeability reduction during pressure depletion than would a shale where the pores have larger aspect ratios.

The role of spacing was different for each configuration. In the case where the effective stress was changing because of an external stress, the role of spacing in permeability reduction

became more pronounced as the spacing between fractures increased. As spacing between fractures increases, each fracture must take more of the load of an external stress. As spacing between fractures decreases, there are more fractures available to accommodate a given stress and the strain is distributed such that each fracture experiences less closure. Therefore, increased fracture density makes fractures less compliant. However, in the case of pore pressure variation, the results were independent of spacing.

Mineral distribution around the pore space showed that soft pores encased in a stiff matrix behave differently than stiff pores encased in a soft matrix. There are several distinct regions when plotting k/k_0 vs. K_{sk}/K_m . When K_{sk} is much lower than K_m , the change in permeability due to external strain is controlled by the fracture stiffness. When K_{sk} is much higher than K_m , the change in permeability is controlled by the matrix stiffness. There is an inflection point where K_{sk} and K_m are equal. Between K_{sk}/K_m at 0.1 to 1, and again from 1 to 10, the behavior is more complex. This is the area of greatest interest as most natural systems would fall in this region.

The simulation shows that permeability evolution due to external strain is controlled by fracture density, pore geometry, and pore stiffness; whereas permeability evolution due to pore pressure changes are controlled by pore geometry and pore stiffness alone. In some shales, the magnitude of permeability evolution for a given external stress and internal pore pressure will be dominated by the permeability enhancement from pore pressure. In other shales—in particular shales where fracture spacing is large—permeability controls may result in a net decrease. This work highlights the importance of understanding that no two shales are alike unless their aspect ratios, fracture spacing, and mineral distribution around pores are all alike. As this is not generally the case, shales will respond differently to changes in stress brought about by drilling operations

and pressure depletion. This suggests that pressure maintenance may be more important in shales with low aspect ratio, soft minerals around pores, and high fracture spacing.

Acknowledgements

This work is a partial result of support from Chevron Energy Technology Company, and their support is gratefully acknowledged.

References

- Bandyopadhyay, K. (2009). Seismic anisotropy: Geological causes and its implications to reservoir geophysics. *Stanford University*.
- Berger, G., Lacharpagne, J. C., Velde, B., Beaufort, D., & Lanson, B. (1997). Kinetic constraints on illitization reactions and the effects of organic diagenesis in sandstone/shale sequences. *Applied Geochemistry*, 12(1), 23-35.
- Bernabe, Y., Brace, W. F., & Evans, B. (1982). Permeability, porosity and pore geometry of hot-pressed calcite. *Mechanics of Materials*, 1(3), 173-183.
- Brown, S. R. (1987). Fluid flow through rock joints: the effect of surface roughness. *Journal of Geophysical Research: Solid Earth*, 92(B2), 1337-1347.
- Budiansky, B., & O'connell, R. J. (1976). Elastic moduli of a cracked solid. *International Journal of Solids and Structures*, 12(2), 81-97.
- Chalon, F., & Montheillet, F. (2003). The interaction of two spherical gas bubbles in an infinite elastic solid. *Journal of Applied Mechanics*, 70(6), 789-798.
- Chang, C. P., Angelier, J., & Huang, C. Y. (2009). Subduction zone geodynamics.
- Civan, F., Rai, C. S., & Sondergeld, C. H. (2012). Determining shale permeability to gas by simultaneous analysis of various pressure tests. *SPE Journal*, 17(03), 717-726.
- Costin, L. S. (1983). A microcrack model for the deformation and failure of brittle rock. *Journal of Geophysical Research: Solid Earth*, 88(B11), 9485-9492.
- Curtis, M. E., Sondergeld, C. H., Ambrose, R. J., & Rai, C. S. (2012). Microstructural investigation of gas shales in two and three dimensions using nanometer-scale resolution imaging Microstructure of Gas Shales. *AAPG bulletin*, 96(4), 665-677.
- Daigle, H., Hayman, N. W., Kelly, E. D., Milliken, K. L., & Jiang, H. (2017). Fracture capture of organic pores in shales. *Geophysical Research Letters*, 44(5), 2167-2176.

- Elsworth, D. (1989, July). Thermal permeability enhancement of blocky rocks: One-dimensional flows. In *International Journal of Rock Mechanics and Mining Sciences & Geomechanics Abstracts* (Vol. 26, No. 3-4, pp. 329-339). Pergamon.
- Fond, C., Riccardi, A., Schirrer, R., & Montheillet, F. (2001). Mechanical interaction between spherical inhomogeneities: an assessment of a method based on the equivalent inclusion. *EUROPEAN JOURNAL OF MECHANICS SERIES A SOLIDS*, 20(1), 59-76.
- Garrett, K. W., & Bailey, J. E. (1977). Multiple transverse fracture in 90 cross-ply laminates of a glass fibre-reinforced polyester. *Journal of Materials Science*, 12(1), 157-168.
- Goodman, R. E. (1989). Introduction to rock mechanics (Vol. 2). *New York: Wiley*.
- Gu, X., & Mildner, D. F. R. (2016). Ultra-small-angle neutron scattering with azimuthal asymmetry. *Journal of Applied Crystallography*, 49(3), 934-943.
- Horne, S. A. (2013). A statistical review of mudrock elastic anisotropy. *Geophysical Prospecting*, 61(4), 817-826.
- Izadi, G., Wang, S., Elsworth, D., Liu, J., Wu, Y., & Pone, D. (2011). Permeability evolution of fluid-infiltrated coal containing discrete fractures. *International Journal of Coal Geology*, 85(2), 202-211.
- Jasiuk, I. (1995). Cavities vis-a-vis rigid inclusions: elastic moduli of materials with polygonal inclusions. *International Journal of Solids and Structures*, 32(3-4), 407-422.
- Javadpour, F. (2009). Nanopores and apparent permeability of gas flow in mudrocks (shales and siltstone). *Journal of Canadian Petroleum Technology*, 48(08), 16-21.
- Javadpour, F., Fisher, D., & Unsworth, M. (2007). Nanoscale gas flow in shale gas sediments. *Journal of Canadian Petroleum Technology*, 46(10).
- Kumar, H., Elsworth, D., Mathews, J. P., & Marone, C. (2016). Permeability evolution in sorbing media: analogies between organic-rich shale and coal. *Geofluids*, 16(1), 43-55.
- Ladeira, F. L., & Price, N. J. (1981). Relationship between fracture spacing and bed thickness. *Journal of Structural Geology*, 3(2), 179-183.
- Li, X., & Elsworth, D. (2015). Geomechanics of CO₂ enhanced shale gas recovery. *Journal of Natural Gas Science and Engineering*, 26, 1607-1619.
- Loucks, R. G., Reed, R. M., Ruppel, S. C., & Jarvie, D. M. (2009). Morphology, genesis, and distribution of nanometer-scale pores in siliceous mudstones of the Mississippian Barnett Shale. *Journal of Sedimentary Research*, 79(12), 848-861.
- Mavko, G., Mukerji, T., & Dvorkin, J. (2009). The rock physics handbook: Tools for seismic analysis of porous media. *Cambridge University Press*.

- Metz, V., Amram, K., & Ganor, J. (2005). Stoichiometry of smectite dissolution reaction. *Geochimica et Cosmochimica Acta*, 69(7), 1755-1772.
- Narr, W. (1996). Estimating average fracture spacing in subsurface rock. *AAPG bulletin*, 80(10), 1565-1585.
- Narr, W., & Suppe, J. (1991). Joint spacing in sedimentary rocks. *Journal of Structural Geology*, 13(9), 1037-1048.
- Ortega, O. J., Marrett, R. A., & Laubach, S. E. (2006). A scale-independent approach to fracture intensity and average spacing measurement. *AAPG bulletin*, 90(2), 193-208.
- Savin, G. N. (1976). Stress concentration around holes,(1961).
- Sisavath, S., Jing, X. D., & Zimmerman, R. W. (2000). Effect of stress on the hydraulic conductivity of rock pores. *Physics and Chemistry of the Earth, Part A: Solid Earth and Geodesy*, 25(2), 163-168.
- Sondergeld, C. H., Newsham, K. E., Comisky, J. T., Rice, M. C., & Rai, C. S. (2010, January). Petrophysical considerations in evaluating and producing shale gas resources. In *SPE Unconventional Gas Conference*. Society of Petroleum Engineers.
- Sone, H., & Zoback, M. D. (2013). Mechanical properties of shale-gas reservoir rocks—Part 1: Static and dynamic elastic properties and anisotropy. *Geophysics*, 78(5), D381-D392.
- Tsang, Y. W., & Witherspoon, P. A. (1981). Hydromechanical behavior of a deformable rock fracture subject to normal stress. *Journal of Geophysical Research: Solid Earth*, 86(B10), 9287-9298.
- Tsukrov, I., & Novak, J. (2002). Effective elastic properties of solids with defects of irregular shapes. *International Journal of Solids and Structures*, 39(6), 1539-1555.
- Ulm, F. J., & Abousleiman, Y. (2006). The nanogranular nature of shale. *Acta Geotechnica*, 1(2), 77-88.
- Vernik, L., & Nur, A. (1992). Ultrasonic velocity and anisotropy of hydrocarbon source rocks. *Geophysics*, 57(5), 727-735.
- Walsh, J. B. (1965). The effect of cracks on the compressibility of rock. *Journal of Geophysical Research*, 70(2), 381-389.
- Zimmerman, R. W. (1985). Discussion:“The Constitutive Theory for Fluid-Filled Porous Materials”(Katsube, N., 1985, ASME J. Appl. Mech., 52, pp. 185–189). *Journal of Applied Mechanics*, 52(4), 983-983.

Zimmerman, R. W. (1986). Compressibility of two-dimensional cavities of various shapes. *Journal of Applied Mechanics*, 53(3), 500-504.

Chapter 2

A Strain Based Approach to Calculate Disparities in Pore Structure between Shale Basins during Permeability Evolution

Abstract

We compare the permeability response of Marcellus shale to Wolfcamp shale under changing strain to explore differences in pore structure between them. This work highlights that while magnitude of strain for a given stress is determined predominantly through a shale's mineral composition, the response of transport properties to a given strain are dependent on fracture spacing, fracture geometry, and mineral distribution around pores. We dynamically stress samples of Marcellus and Wolfcamp shales and observed levels of compaction, creep, and permeability evolution. We characterize the differences between the two shales using bulk mineralogy, SEM imaging with elemental analysis, and the cubic law for permeability evolution. We find that the Marcellus shale is comprised predominantly of clays that leads to more deformation when stressed than the Wolfcamp shale which is composed predominantly of quartz and calcite. The level of creep and compaction are directly related to the amount of clay in each shale sample. Modifications to the cubic law for fluid flow reveal that Marcellus shale has a lower fracture density than the Wolfcamp shale, that the pore geometry more closely resembles slit-like pores, and that the mineral distribution around the pore space is soft compared to the Wolfcamp shale. These differences cause the Marcellus shale to experience much greater permeability reduction under the same compressive strain than the Wolfcamp. The result of our study is a unique strain-driven model to capture permeability evolution in shale due to differences in pore structure.

Introduction

There are several permeabilities existent within a shale reservoir (Curtis, 2002). The first is the permeability of hydraulic fractures created during completions operations—these are highly conductive pathways that increase the overall permeability of the reservoir. The second is the permeability of preexisting fractures—also called joints—which are the result of subsurface processes that occur during burial, organic maturation, and tectonic stress (Engelder, 1985; Hancock & Engelder, 1989). There are often several sets of joints in a shale, and the effectiveness of hydraulic fracturing is dependent on the density of joints intersected (Engelder et al., 2009).

There exist a third and fourth permeability in shales, and these are found in the solid matrix between joints. These two permeabilities are much lower than the joint permeability or the hydraulic fracture permeability. Within the matrix shale there exist small pathways in between grain boundaries that allow for hydrocarbons to migrate to the joint sets. There are two sets of such flow paths which create distinct, orthogonal permeabilities: two oriented in the bedding-parallel direction and one in the bedding-perpendicular direction. The flow paths in the bedding-perpendicular direction are often typified as highly tortuous nano-sized capillary tubes (Javadpour et al., 2007; Javadpour, 2009; Civan et al., 2012), whereas the flow paths in the bedding-parallel direction can be modeled as long penny-shaped cracks (Li & Elsworth, 2014; Kumar et al., 2015). Many studies have focused on characterizing the flow in the bedding-perpendicular direction: the purpose of this study is to better understand the flow in the bedding-parallel direction.

Within the matrix rock, shale is an orthotropic material with a dominant fracture set in the bedding-parallel direction (Crook, 2002; Bonnelye, 2017). The dominant fracture set is composed of long, penny-shaped fractures separated by finely laminated bedding planes (Bandyodaphyay, 2009) on the order of 1 to 100 microns thick (Ulm & Abousleiman 2006; Horne, 2013). The

fracture apertures in the bedding-parallel direction are thought to range between 0.01 to 0.5 microns—a range which allows for diffusion-driven flow as the aperture approaches the mean flow path of the gas molecules (Javadpour, 2009; Civan, 2013). This fracture set is responsible for the majority of flow, and permeability in the bedding-parallel direction has been found to be 10 to 100 times higher than permeability in the bedding-perpendicular direction (Bolton et al., 2000; Kwon et al., 2004; Pan et al., 2015).

Many investigators have focused on characterizing the nano-tube driven flow in the bedding-perpendicular direction and have found that the no-slip boundary condition used to develop laminar flow models is no longer valid at fracture diameters in the 1 nm to 50 nm range (Javadpour, 2009; Civan, 2012). Measured permeabilities in shales range from 10^{-23} m^2 to 10^{-17} m^2 (Daigle, 2017). Darcy driven flow dominates from approximately 10^{-20} m^2 to 10^{-17} m^2 , whereas molecular diffusion and Knudsen flow must be accounted for when permeability reaches approximately 10^{-21} m^2 or lower (Brown, 1946; Civan, 2012). These ranges are not absolute, and an understanding of the fracture set's geometry and distribution within the matrix remain critical parameters for characterizing permeability and flow through these tight rocks.

It is well known that permeability is a dynamic metric: drilling (Islam et al., 2009), fracturing (Daigle, 2017), creep (Sinha, 2013), and seismic events (Polak et al., 2003; Candela et al., 2014) have all been shown to alter the initial permeability. A change in permeability is caused by either a change in flow channel diameter or fracture coalescence (Eberhardt et al., 1999). In both cases, deformation is the main contributor to changes in the fracture geometry. At stresses that are well below the rock's ultimate strength, compressive deformation closes fractures, whereas fractures begin to coalesce as compressive stress approaches the ultimate strength (Walsh, 1966; Scholz, 1968).

There are three parameters that define a fracture set's geometry within a shale: the fracture length a , the fracture aperture b , and the fracture spacing s . The aspect ratio α is the ratio b/a and ranges from unity for circular tubes to a limit of zero for infinite cracks. The ability to flow fluid through a fracture set is predominantly a function of the fracture aperture, and gas production is typically modelled as flow between parallel plates (Goodman, 1989). Of equal importance is the fracture spacing—if the fractures are dense then permeability will be higher, whereas permeability will be lower in the case that the spacing between fractures is large. Fracture spacing is known to be related to bedding thickness (Ladeira, 1981; Narr, 1991) and the degree of rock compaction during burial (Chang et al., 2009). Spacing is often proportional to fracture aperture (Garrett & Bailey, 1977). While it will vary spatially, the spacing determined by permeability measurements will reflect an average (Narr, 1996; Ortega et al., 2006). In joint sets, the spacing between fractures is known to remain constant after a certain compressive strain threshold (Wu & Pollard 1995).

Elsworth (1989) explored permeability evolution in fractured media when the change in aperture was due to deformation of the solid bedding planes and was controlled by s . This assumption is valid when mineral stiffness is much larger than fracture stiffness or when s is much larger than b . In the case of shale matrix, there currently exists no quantitative link between the bedding planes—which are finely laminated mineral ensembles—and fracture spacing. The aim of this work is to quantify the spacing and aperture values, the spacing-to-aperture ratio, and to set up a scheme that solves for these two variables.

In addition to differences in pore geometry and fracture density, shales also exhibit a range of mineralogical composition which determines material properties. The bulk modulus and shear modulus of a rock can be accurately measured if its mineralogical composition is known, as these values will be an average of each mineral's individual elastic moduli (Voigt, 1889; Reuss, 1929;

Hill, 1952; Clark, 1966; Simmons & Wang, 1971). A sedimentary rock's elastic moduli will determine its response to stress. Shale is a class of rocks typified by low permeability and high clay content. However, the variation in mineralogy between shale basins is large, resulting in different bulk responses to changes in stress (Sone & Zoback, 2013). The mineral constituents of shale besides clays—quartz, feldspars, carbonates, and pyrite—have rigid grains and resist mechanical compaction to a greater degree than clays (Gu & Mildner, 2016). Variations in mineralogy lead to variations in elastic and non-elastic deformation. A common feature of shales that makes them difficult to characterize in the laboratory is time-dependent compaction. After a shale sample has been reintroduced to stress, it will continue to compact for a period ranging from hours to weeks (Sinha et al., 2013). The magnitude of this compaction is variable, and the permeability reduction experienced during this time can be negligible or several orders of magnitude. A critical unknown in the laboratory is whether this time dependent compaction is a feature that reservoir rocks will experience during drilling and completions operations and pressure depletion or whether it is simply the rock returning to its *in situ* configuration after being exhumed to atmospheric stress conditions. As this compaction is noted in both outcrop samples and cored samples, it is believed to be a condition that can be activated during drilling and completions activities. As mineralogy is heterogenous throughout a reservoir, the mechanical response to reactivated compaction is complex. An understanding of pore structure throughout the reservoir is required to understand the response of transport properties to reactivated compaction.

For shales that have high amounts of organic matter, the porosity is mainly found within the organic matter itself (Loucks et al., 2009). Much of the remainder of the porosity is found in the clay—predominantly illite and smectite (Sondergeld et al., 2010; Curtis et al., 2012). In the previous chapter, we showed that this leads to a potential mismatch between the minerals

surrounding the pore space and the minerals within the matrix. For organic-rich and clay-rich shales, pores are likely to be typified as soft fractures embedded in a stiffer matrix. For shales that are not organic-rich or clay rich, this characteristic is likely to be reversed with stiff fractures surrounded by a soft matrix. Regardless of overall mineralogy, dissolution of silica or calcite throughout geologic time can lead to cementation of pore boundaries (Berger et al., 1997; Metz et al., 2005). Published values of elastic moduli for various minerals suggest that this disparity of mineral distribution around pores can cause a mismatch in material properties that could be several orders of magnitude (Mavko, 1998; Mavko, 2009).

In addition to fracture spacing and mineral distribution, shales have been reported to have different pore geometries from basin to basin. The aspect ratio has been found to vary from 0.05 to almost 1.0 in Permian Basin shales, whereas the Bakken shale was found to have an average aspect ratio of 0.10 (Bandyopadhyay, 2009; Sone & Zoback, 2013). In the previous chapter, we explored the additional aperture closure that results from decreasing aspect ratios at the same strain and saw that it could contribute substantially to permeability evolution in the case that two shales are characterized by different aspect ratios. In this study, we will further explore the mineralogical differences between the Marcellus shale and Wolfcamp shale. We will use the cubic law to solve for fracture spacing and aspect ratio for these two basins. We incorporate differences in mineral distribution around pores into our strain driven model and find that permeability evolution with evolving strains can be described with these variables.

Characterization Techniques

We performed a suite of experiments on cylindrical samples of Marcellus shale and Wolfcamp shale that were loaded into a triaxial vessel. Samples were stressed and allowed to compact until no additional deformation was measured by an LVDT placed on the outside of the triaxial vessel. Compaction lasted anywhere from a few hours to a few days. We measured

permeability evolution with evolving strains and different pore fluids using pressure pulse tests (Brace, 1965). Mineralogy data were collected on samples before loading them into the triaxial vessel.

SEM Imaging

In addition to experimental data, we gathered SEM images from our samples. We performed elemental analysis on two sample sites for the Marcellus shale and two for the Wolfcamp shale. The images are included below in Figure 2-1. We include elemental analysis for calcium, aluminum, and silicon as proxies for calcite, clays, and quartz—we note that silicon will be present in clays as well as quartz grains. Figure 2-1 shows a greater concentration of silicon where quartz is located, whereas measurements in clays do not generally show such high concentrations. As can be seen in Figure 2-1, the Marcellus sample shows much higher clay composition with calcite and quartz embedded in a clay matrix, whereas the Wolfcamp samples show much higher quartz and calcite composition.

The images shown in Figure 2-1 are typical of what we found for the samples investigated. As can be seen in the column of backscatter images, the fabric of these two shales are categorically different. This is confirmed in the second column, where the calcium content of the Wolfcamp sample is much higher than in the Marcellus sample. While these are both shales, the differences in depositional environment, burial history, thermal maturation, and mineral migration are apparent as the clay content of the Marcellus samples appears to be quite high compared to the Wolfcamp samples.

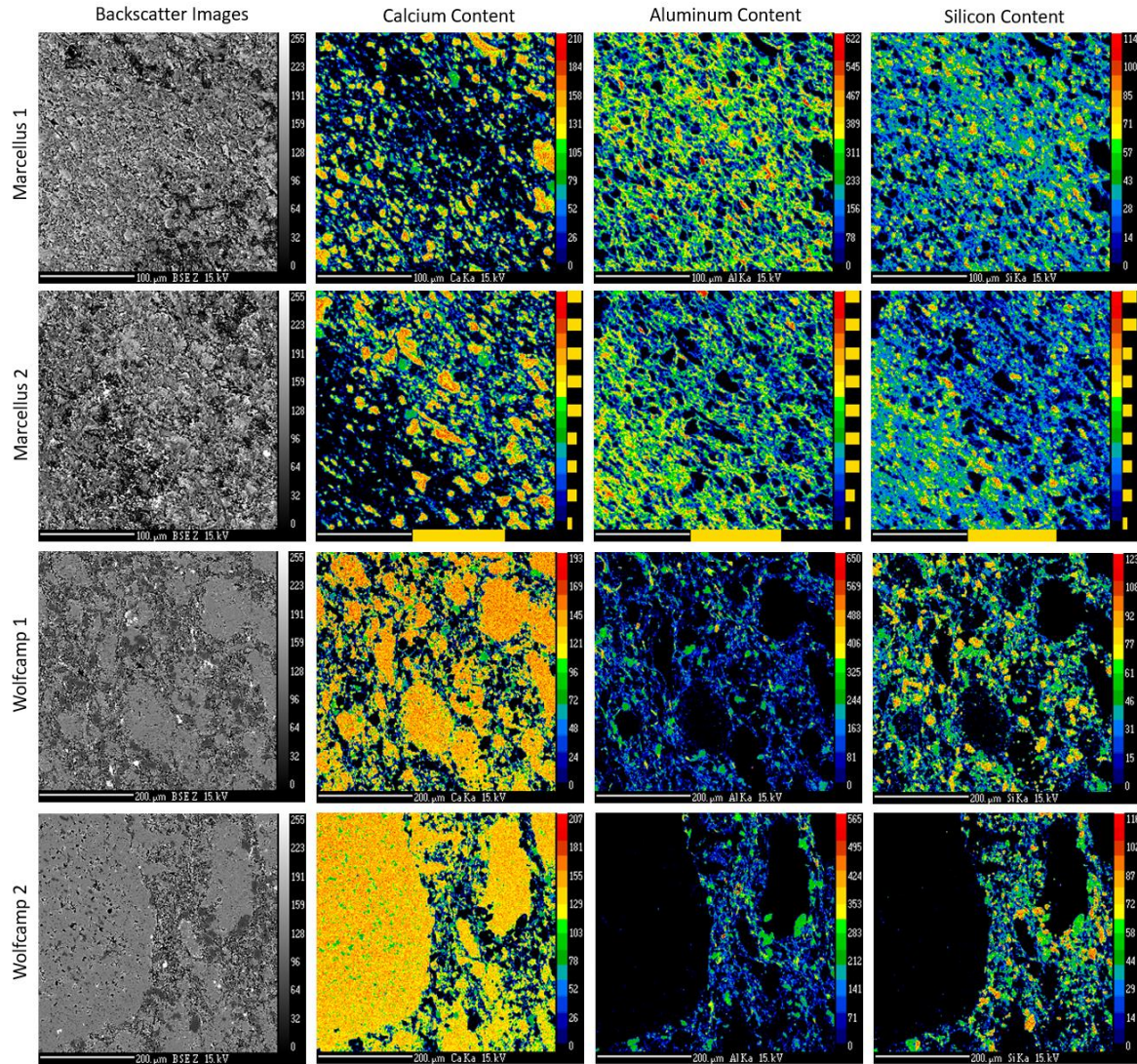


Figure 2-1: SEM images of Marcellus and Wolfcamp shales. Each row shows (from left to right) a backscatter image, calcium content, aluminum content, and silicon content as proxies for calcite, clays, and quartz. In the case of the Marcellus images (top two rows), the predominant mineral constituent is clay. In the Wolfcamp, the predominant mineral is calcite with clays surrounding large calcite grains. This suggests that the Marcellus is likely to be typified as soft pores surrounded by a stiffer matrix and the Wolfcamp as stiffer pores surrounded by a soft matrix.

These images suggest that the mineral stiffness of the pore skeleton K_{sk} will be higher than the matrix stiffness K_m in the Wolfcamp such that K_{sk}/K_m may be greater than unity. In the Marcellus, this trend is reversed, such that K_{sk}/K_m will be less than unity. As the mineralogy data shows below, the principle difference is the amount and location of the quartz and calcite.

Mineralogy Data

We also gathered bulk mineralogy data for both the Marcellus and Wolfcamp samples. We found that in general the Marcellus samples were clay-rich with lesser amounts of quartz or carbonates than the Wolfcamp samples. In Figure 2-2 the clay content of Marcellus samples are generally higher than in the Wolfcamp samples, whereas the Wolfcamp had larger amounts of quartz and carbonates. These three minerals accounted for most of the composition for each sample, although organic matter (1-4%), pyrite (<2%), and other minerals were found to lesser degrees. Figure 2-2a shows that values for clay content in the Marcellus ranged from 27%-60% by weight and in the Wolfcamp ranged from 8%-44% by weight. Quartz values range from 19%-38% in the Marcellus and in the Wolfcamp from 17%-52% by weight. Figure 2-2b shows clay content cross plotted with carbonate content. In both basins, as carbonate content increases, clay content decreases. The carbonate content in the Marcellus ranged from 0%-43% and in the Wolfcamp from 2%-71%. Figure 2-2d shows the combined quartz content and clay content compared to the carbonate content. Both basins fall along the same straight line. Figure 2-2e and Figure 2-2f show similar plots for different combinations of quartz, clay, and carbonates.

For the Wolfcamp shale samples we were able to gather acoustic data and density data as well. We used the standard equations to convert V_p , V_s , v and ρ into K , G , and E :

$$K = \rho(V_p^2 - \frac{4}{3}V_s^2) \quad (1)$$

where K is the bulk modulus, ρ is the rock density, and V_p and V_s are the compressional and shear wave velocities, respectively.

$$G = \rho V_s^2 \quad (2)$$

where G is the shear modulus.

$$E = \rho V_E^2 \quad (3)$$

where E is the Young's modulus.

$$\nu = \frac{V_p^2 - 2V_s^2}{2(V_p^2 - V_s^2)} \quad (4)$$

where ν is the Poisson ratio. We then plotted elastic moduli against mineralogy. V_p ranged from 3.5 to 5.6 km/s and V_s ranged from 2.1 to 3.2 km/s. Density ranged from 1450 to 1835 kg/m³. Poisson ratio ranged from 0.18 to 0.28 with most values falling between 0.19 to 0.22.

In Figure 2-3 we see that all three of the moduli decrease with increasing clay content and increase with increasing carbonate content. Modulus values increased with increasing quartz content but with more spread around the linear regression curve. Values for bulk modulus K ranged from 10 GPa to 26 GPa as the clay content ranged from 8%-44% and carbonate content ranged from 2%-71%. Bulk modulus for clay ranges from 1.5 GPa for a Kaolinite to 25 GPa for Gulf clays, whereas quartz is 37 GPa, calcite is 64-77 GPa, and kerogen is 2.9 GPa (Mavko & Mukerji, 2009). These values suggest that the minerals found in the Wolfcamp must be on the low end of the ranges provided by Mavko (2009).

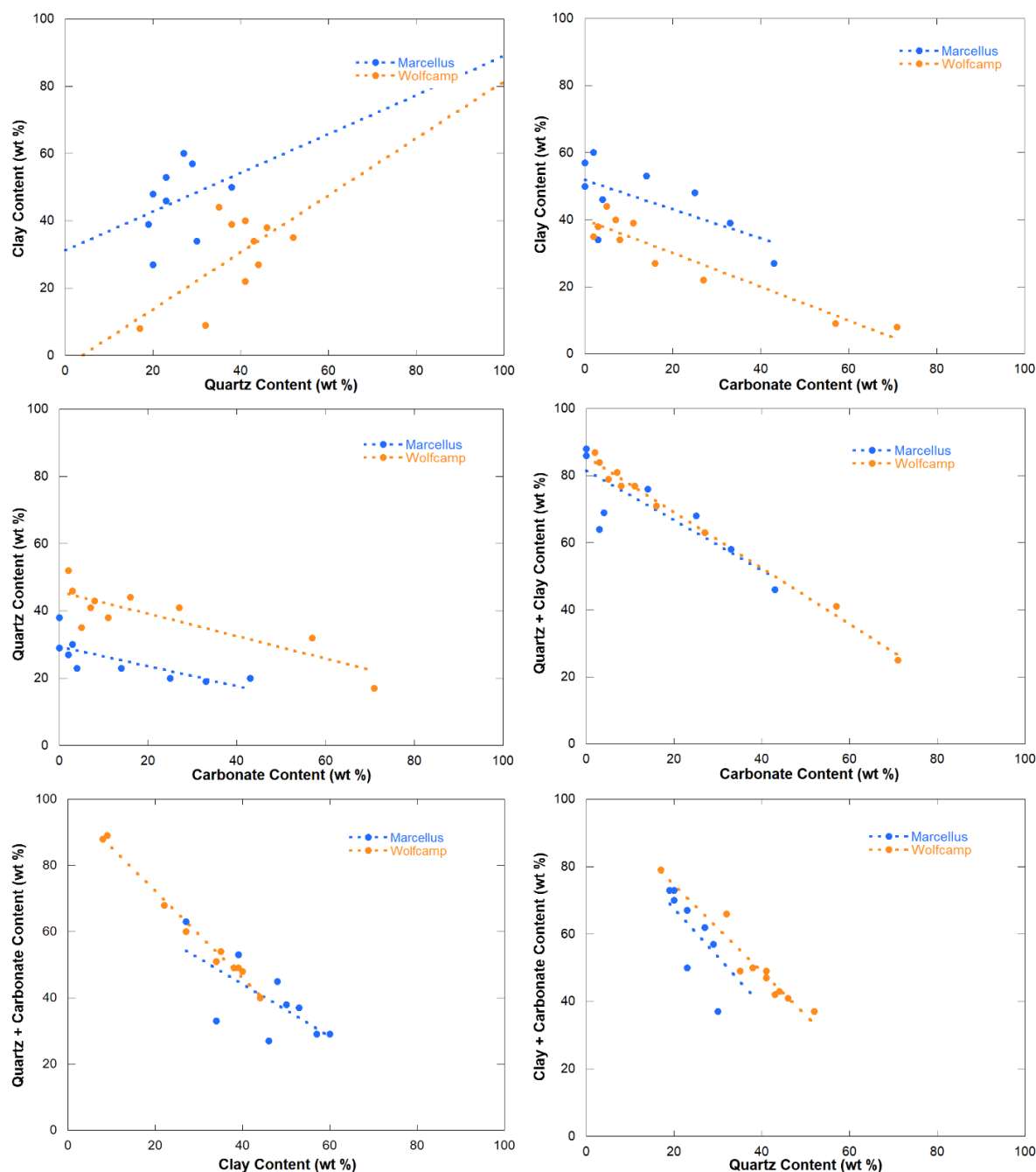


Figure 2-2: Cross plots of mineralogy by weight % for Wolfcamp samples and Marcellus samples. Figure 2-2a displays clay content vs. quartz content and shows that the Marcellus typically has higher clay composition. Figure 2-2b displays clay content vs. carbonate content. Figure 2-2c displays quartz content vs. carbonate content and shows that the Wolfcamp samples have higher quartz composition. Figure 2-2d shows quartz + clay vs. carbonate content. All values for both basins fall along a straight line. Figure 2-2e displays quartz + carbonate vs. clay and shows that the Wolfcamp is predominantly quartz and carbonates whereas the Marcellus is predominantly clay. This suggests a mismatch in mineral distribution around pores. Figure 2-2f displays clay + carbonate content vs. quartz content.

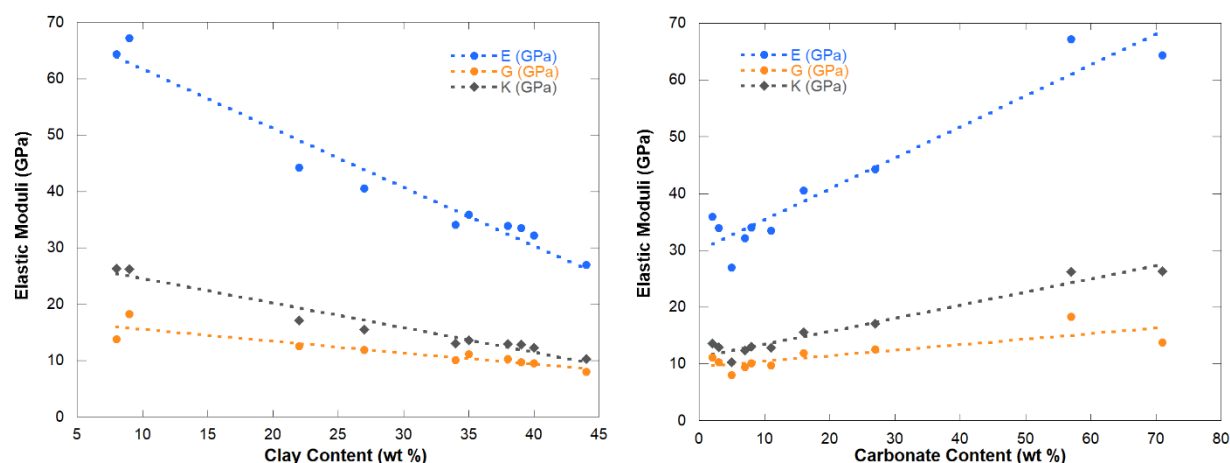


Figure 2-3: Elastic moduli of Wolfcamp samples with varying mineralogy. E, G, and K all decrease with increasing clay content (LHS) and decreasing carbonate content (RHS).

Time Dependent Compaction Data

We compiled compaction data from six Marcellus shale samples. All samples were loaded to 24 MPa hydrostatic stress and allowed to compact until there was no additional deformation. Figure 2-4 shows compaction over approximately 10 hours. In this case, positive strain is compression. These curves were compared to mineralogy data and it was found that the magnitude of compaction was directly related to the clay composition of each sample. The right axis of Figure 2-4 shows the clay content of each sample and provides an excellent match.

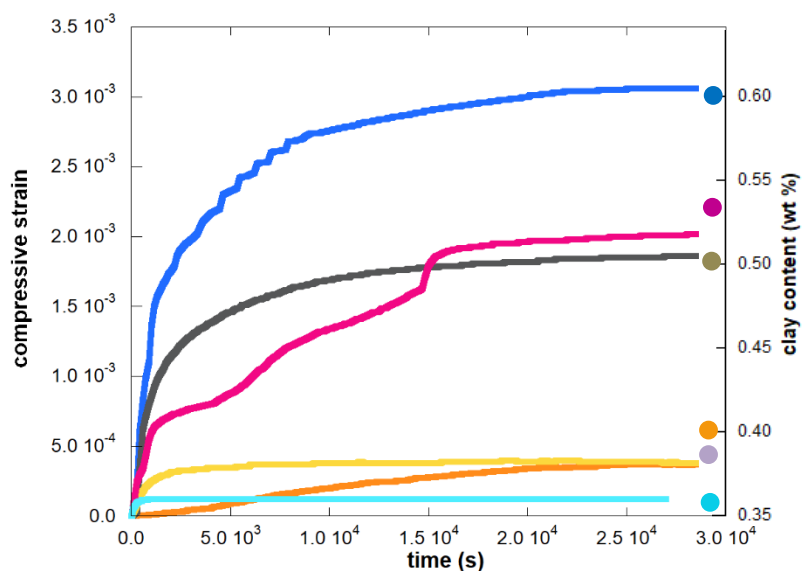


Figure 2-4: Compaction after loading (left) is related to % clay content (right).

Time dependent compaction is a common problem for shale in the laboratory (Sinha, 2013). During our experimental suite we measured permeability evolution with pore pressure using helium and methane in series. As shown in Figure 2-5, the Marcellus sample does not exhibit the expected behavior. The helium curve should be monotonically increasing, as the only elastic effect should be poromechanical expansion. However, as time dependent compaction is also occurring, both the helium and methane curves are rotated downward. On the right-hand side of Figure 2-5 is a set of curves for the Wolfcamp shale. There is not the same time dependent compaction visible in the Wolfcamp sample, as can be seen by permeability enhancement with increasing pore pressure for helium. Both samples have an organic content of 3%, resulting in similar wedges between the helium curve and the methane curve due to adsorptive permeability loss with methane. However, the Marcellus sample is 50% clay whereas the Wolfcamp sample is only 38% clay. Later we show that the permeability loss is also due to the additional pore compressibility within the Marcellus.

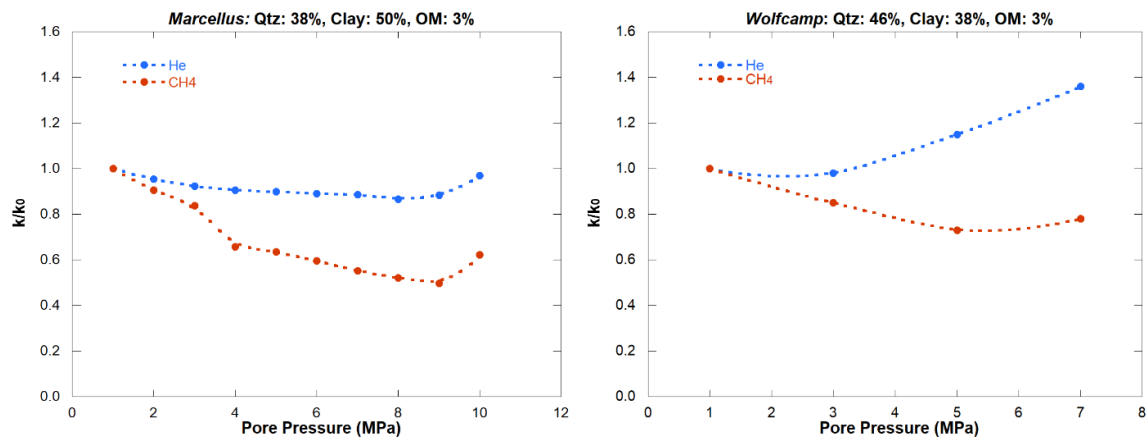


Figure 2-5: Marcellus shale samples creep during permeability measurements, whereas Wolfcamp shale samples do not. On the LHS permeability is plotted against pore pressure. The blue curve representing helium should be monotonically increasing due to poromechanical expansion, as is seen on the RHS for the Wolfcamp sample. The downward shift of the curves on the LHS is due to time dependent compaction throughout the experiment. The Marcellus sample is 50% clay and 38% quartz, whereas the Wolfcamp sample is 38% clay and 46% quartz. Both are 3% organic matter, which is seen in the adsorptive permeability loss between the helium and methane curves for each sample.

Permeability Evolution with Strains

After samples compacted, we measured permeability evolution as we varied strain. In general, Marcellus samples experienced a much larger reduction of permeability compared to the Wolfcamp samples. In Figure 2-6 we plot permeability evolution versus strain for a representative run from each shale basin. The permeability evolution in the Wolfcamp was quite different than in the Marcellus. As can be seen in Figure 2-6, the Marcellus sample experienced a 100-fold permeability reduction compared to the Wolfcamp at the same amount of external strain.

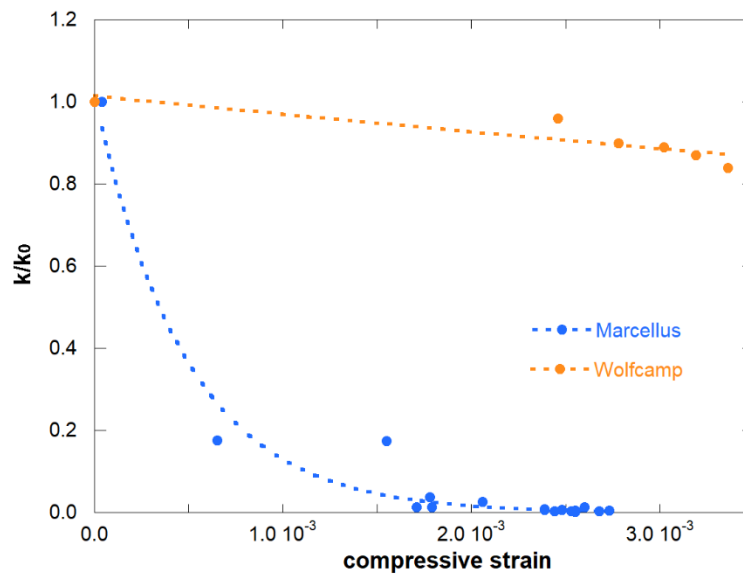


Figure 2-6: The same magnitude of strain in Marcellus samples produce very large permeability loss compared to the same level of strain in Wolfcamp samples.

Characterization Using the Cubic Law

The cubic law can be modified to explore the roles of fracture spacing, fracture geometry, and mineral distribution around pores. First, we derive an expression for the spacing the aperture ratio s/b in terms of permeability evolution with strain. Then, we modify that expression to solve for average aspect ratio b/a . We can use the mineralogical constraints to reconcile the differences in permeability evolution with the mineral distribution around the pore space as captured by K_{sk}/K_m from the previous chapter.

Fracture Spacing

Next, we will examine the disparity between the Wolfcamp and Marcellus shale's permeability evolution by exploring the spacing to aperture ratio s/b , also called the fracture spacing. In Figure 2-7, the cubic law is used to plot several permeability curves at different spacing to aperture ratios along with the experimental data to illustrate the influence of this variable. As can be seen, the data suggest that the Marcellus shale fracture spacing is much further apart than the Wolfcamp. For fractures that are far apart, the spacing can be the primary driver of permeability evolution.

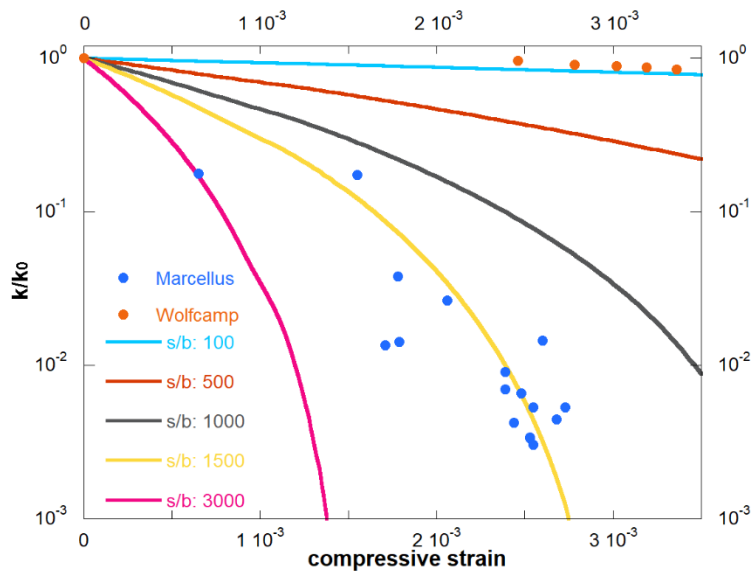


Figure 2-7: As s/b increases, permeability is reduced at the same strain. The Marcellus shale permeability data fits a fracture spacing of approximately 1500, whereas the Wolfcamp sample fits a spacing of 50. In this figure, no other influences are considered. The fracture spacing will be lower once pore geometry and mineral stiffness are included later.

For flow between parallel plates, permeability evolution can be cast as

$$\frac{k}{k_0} = \left(1 + \frac{\Delta b}{b_0}\right)^3 \quad (5)$$

where k is the permeability in m^2 , k_0 is the initial permeability, b_0 is the initial aperture, and Δb is the change in aperture—in the case of aperture reduction Δb is negative. In our experiments, we measured deformation along the bedding-parallel fracture set such that the dynamic Poisson ratio

is required to convert to deformation perpendicular to the fracture set. To calculate the portion of permeability evolution due to spacing, Δb can be defined as

$$\Delta b = \nu \varepsilon s \quad (6)$$

where ν is the Poisson ratio, ε is the longitudinal strain, and s is the fracture spacing in meters. This changes equation 5 to

$$\frac{k}{k_0} = \left(1 - \nu \varepsilon \frac{s}{b_0}\right)^3 \quad (7)$$

Equation 7 is similar to Elsworth's (1989) approach to fractures that are soft compared to the matrix:

$$\Delta k = \frac{1}{12s} (b + s \Delta \varepsilon)^3 \quad (8)$$

Because spacing is assumed to be constant, we note that the initial spacing-to-aperture ratio s/b_0 is constant:

$$\frac{s}{b_0} = \text{constant} \quad (9)$$

We can therefore rearrange equation 7 in terms of this constant ratio:

$$\frac{s}{b_0} = \frac{1}{\nu \varepsilon} \left(1 - \left(\frac{k}{k_0}\right)^{\frac{1}{3}}\right) \quad (10)$$

In the above formulation, the value of the spacing-to-aperture ratio is a constant and represents the role of the fracture spacing in permeability evolution in the absence of other influences. We plot the values of equation 10 below in Figure 2-8 for a Marcellus sample and a Wolfcamp sample.

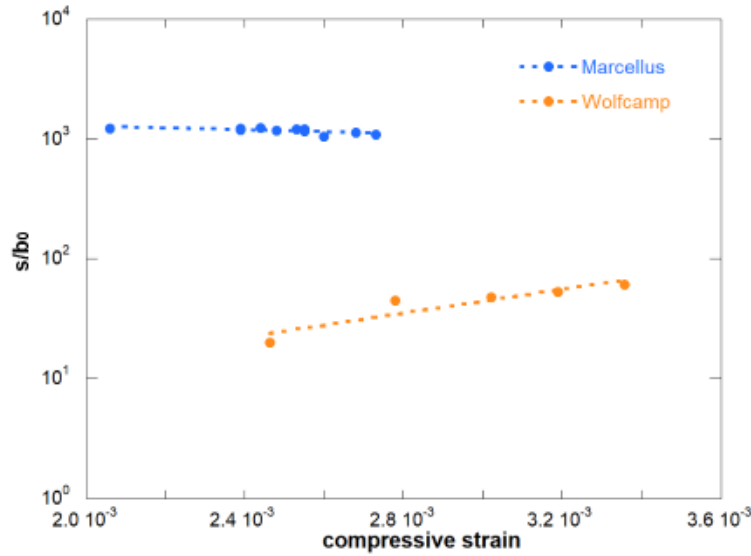


Figure 2-8: Calculated fracture spacing using permeability and strain data in Equation 10 with a Poisson ratio of 0.22. In the absence of other influences, the Marcellus has a high spacing over 10^3 whereas the Wolfcamp is approximately 50. This is in conjunction with Figure 2-7.

Pore Geometry

Exploring the role of pore geometry, we return to the equations we used in the previous chapter, where α equals b/a :

$$C_{pc} = \frac{1-\nu}{G} \left(\alpha + \frac{1}{\alpha} \right) \quad (11)$$

The strain in the pore space can be found with the effective stress and the pore compressibility:

$$\varepsilon_{pc} = \sigma' C_{pc} \quad (12)$$

The change in aperture $\Delta b/b$ can be calculated two ways. The first is to assume that the aspect ratio is constant, as was done in the previous chapter. In that case, the isolated role of pore geometry in determining permeability evolution is

$$\frac{k}{k_0} = \left(1 - \sigma' C_{pc} \right)^{\frac{3}{2}} \quad (13)$$

As α approaches zero, pore compressibility can be simplified as

$$C_{pc} = \frac{1-\nu}{G\alpha} \quad (14)$$

such that

$$\varepsilon_{pc} = \varepsilon \frac{1-\nu}{\alpha} \quad (15)$$

where we differentiate between the pore strain ε_{pc} and the bulk external strain ε . Setting equation (7) and equation (13) equal to each other:

$$\left(1 - \varepsilon \frac{1-\nu}{\alpha}\right)^{\frac{1}{2}} = 1 - \nu \frac{s}{b_0} \varepsilon \quad (16)$$

Expanding the right hand side creates a 2nd order polynomial

$$1 - \varepsilon \frac{1-\nu}{\alpha} = 1 - 2\nu \frac{s}{b_0} \varepsilon + \nu^2 \frac{s^2}{b_0^2} \varepsilon^2 \quad (17)$$

Which simplifies to

$$\frac{a}{b} (1 - \nu) = \nu \frac{s}{b_0} (2 - \nu \frac{s}{b_0} \varepsilon) \quad (18)$$

Noting that b/b_0 is $k/k_0^{1/3}$ this expression becomes

$$\frac{a}{s} = \frac{\nu}{1-\nu} \left(\frac{k}{k_0}\right)^{\frac{1}{3}} \left(1 + \left(\frac{k}{k_0}\right)^{\frac{1}{3}}\right) \quad (19)$$

Equation (15) is valid when the aspect ratio α is assumed constant. This need not be the case, and in the event that α changes due to fracture closure Equation (13) becomes

$$\frac{k}{k_0} = (1 - \sigma' C_{pc})^3 \quad (20)$$

This simplifies the steps to isolate a/s as follows. Setting equation (7) and equation (20) equal to each other leads to

$$1 - \varepsilon \frac{1-\nu}{\alpha} = 1 - \nu \frac{s}{b_0} \varepsilon \quad (21)$$

Which simplifies to

$$\frac{a}{b} (1 - \nu) = \nu \frac{s}{b_0} \quad (22)$$

Such that

$$\frac{a}{s} = \frac{\nu}{1-\nu} \left(\frac{k}{k_0} \right)^{\frac{1}{3}}, \text{ variable } \alpha \quad (23)$$

The results from equation (19) and equation (23) are applied to the data for the Marcellus and Wolfcamp samples and are plotted below in Figure 2-9.

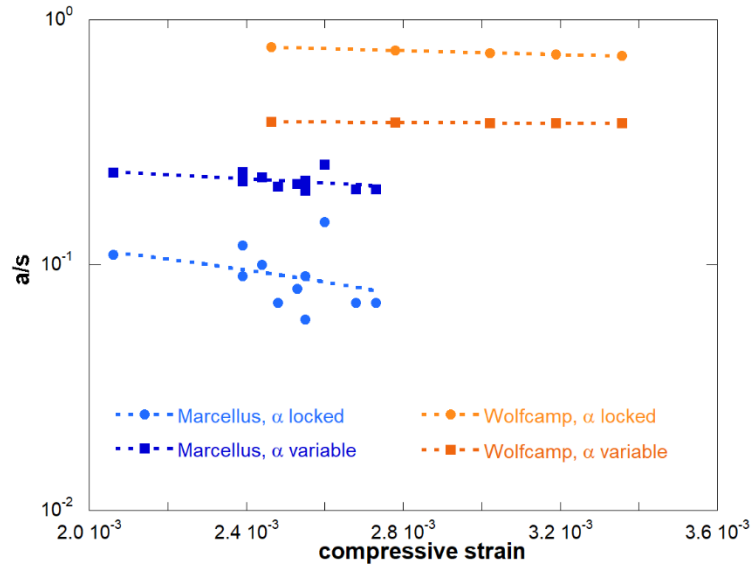


Figure 2-9: Fracture length to spacing a/s . Both equation 19 and equation 23 are shown.

The solutions we are interested in are for the α variable case. The value of a/s for the Marcellus is approximately 0.20 and for the Wolfcamp is approximately 0.40. This is a valuable constraint, because later it will allow us to define the aspect ratio in terms of the spacing. With equation (10) and equation (23), the initial aspect ratio α_0 can be calculated. As strain was parallel to the ellipsoid major semi-axis, changes in aspect ratio are primarily from changes in aperture Δb . Any Δa can be assumed negligible for the experiment's configuration, such that b_0/a should provide a good estimate of α_0 . Combining equations (10) and (23) give

$$\frac{b_0}{a} = \frac{\frac{b_0}{s}}{\frac{a}{s}} = \frac{\varepsilon(1-\nu)}{\left(\frac{k}{k_0} \right)^{\frac{1}{3}} \left(\left(\frac{k}{k_0} \right)^{\frac{1}{3}} - 1 \right)} \quad (24)$$

The results of equation (24) are plotted for each sample below in Figure 2-10. We can see in Figure 2-10 that the aspect ratio for the Wolfcamp is approximately five times larger than in the

Marcellus. In the absence of other influences, the Marcellus α is approximately 10^{-2} , and the Wolfcamp is approximately 5×10^{-2} . Equation 20 suggests that this alone can result in a 50% difference in permeability evolution.

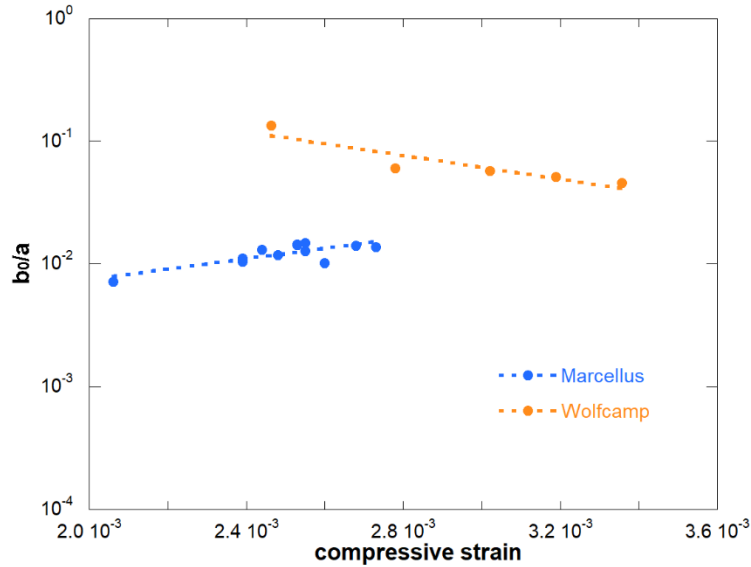


Figure 2-10: Calculated initial aspect ratio for both the Marcellus and Wolfcamp samples.

Mineral distribution around the pore space

In the previous chapter, we presented permeability evolution as a function of K_{sk}/K_m , where K_{sk} is the stiffness of minerals around the pore space and K_m is the stiffness of the matrix. We can modify the plot from the previous chapter showing permeability evolution and view changing apertures instead. The result is plotted below in Figure 2-11. As in the previous chapter, we note that the solution is independent of strain. This is useful, as it reduces the number of variables that are dependent on strain by one. Figure 2-11 should be interpreted as the additional change in aperture as a result of pore stiffness. Values are normalized to K_{sk}/K_m equal to 1. Values below this threshold represent softer minerals allowing for greater pore closure due to strain. Values above this threshold correct the aperture loss associated with other influences when the minerals around pores are stiffer than the surrounding matrix.

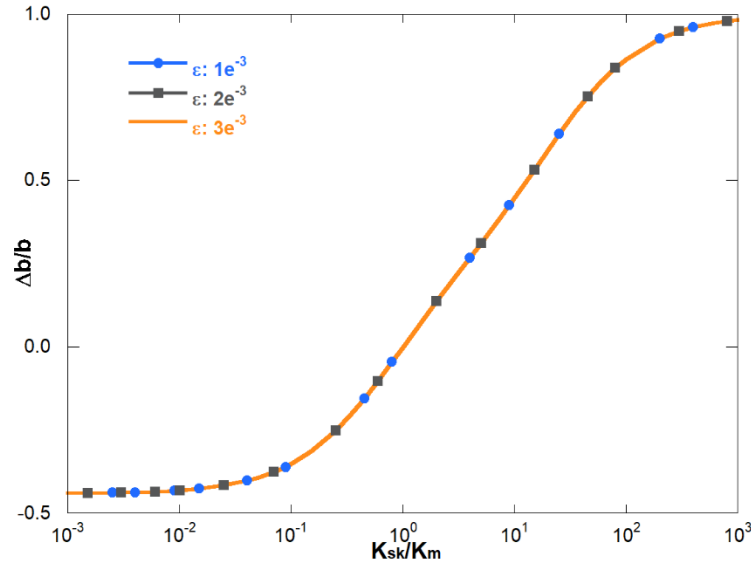


Figure 2-11: Changing aperture with varying pore mineral stiffness. Results are normalized to K_{sk}/K_m equal to 1, and show that if a grain mismatch creates a pore mineral stiffness less than the surrounding matrix stiffness, additional aperture is lost. The results are independent of strain.

Integrating all variables

In the above sections, fracture spacing s/b , pore geometry α , and mineral stiffness K_{sk}/K_m were analyzed as independent variables in order to understand their individual contributions to permeability evolution. Now they are analyzed in conjunction with each other to provide a more complete characterization of the pore structure of shales. The complete equation for permeability evolution is

$$\frac{k}{k_0} = \left(1 + \left(\frac{\Delta b}{b_0} \right)_{\frac{s}{b}} + \left(\frac{\Delta b}{b_0} \right)_{\alpha} + \left(\frac{\Delta b}{b} \right)_{\frac{K_{sk}}{K_m}} \right)^3 \quad (25)$$

where the influence of fracture spacing s/b , pore geometry α , and mineral stiffness K_{sk}/K_m are defined based on the change in pore aperture that they are each responsible for. The last term for K_{sk}/K_m does not have an analytical solution, but we can use Figure 2-11. Mineral stiffness varies within one order of magnitude. It is expected that most mismatches will be close to K_{sk}/K_m equal

to unity; however, the variance in aperture around this value is large. Having developed equations for the other terms, we can recast equation (25) as

$$\frac{k}{k_0} = \left(1 + \nu \varepsilon \frac{s}{b_0} + \varepsilon \frac{1-\nu}{\alpha} + \left(\frac{\Delta b}{b} \right) \frac{K_{sk}}{K_m} \right)^3 \quad (26)$$

Recalling from Figure 2-9 that a/s is approximately 0.2 for the Marcellus and 0.4 for the Wolfcamp, we can constrain the relationship between s/b_0 and α :

$$\frac{a}{s} = c \rightarrow \frac{a}{b_0} = c \frac{s}{b_0} \quad (27)$$

such that equation 26 becomes

$$\frac{k}{k_0} = \left(1 - \varepsilon \left(\nu \frac{s}{b_0} + c \frac{s}{b_0} (1 - \nu) \right) + \left(\frac{\Delta b}{b} \right) \frac{K_{sk}}{K_m} \right)^3 \quad (28)$$

The value of c in equation 28 is 0.2 for the Marcellus and 0.4 for the Wolfcamp. Having eliminated α , we can use a best fit for s/b_0 and the change in aperture due to mineral stiffness from Figure 2-11. We find that the values that best fit the permeability and strain data are s/b equal to 700 for the Marcellus and 40 for the Wolfcamp, α equal to 0.007 for the Marcellus and 0.06 for the Wolfcamp, and K_{sk}/K_m of 0.7 for the Marcellus and 1.0 for the Wolfcamp. This suggests that the Wolfcamp has a much higher fracture density than the Marcellus, allowing for strain to be distributed among more fractures. It also shows that the aspect ratio of the Marcellus pores make them more compressible than in the Wolfcamp. Casting the Marcellus as softer pores in a stiff matrix than the Wolfcamp recovered the remaining variance between equation 28 and the experimental data. The matches to the permeability versus strain curves are below in Figure 2-12.

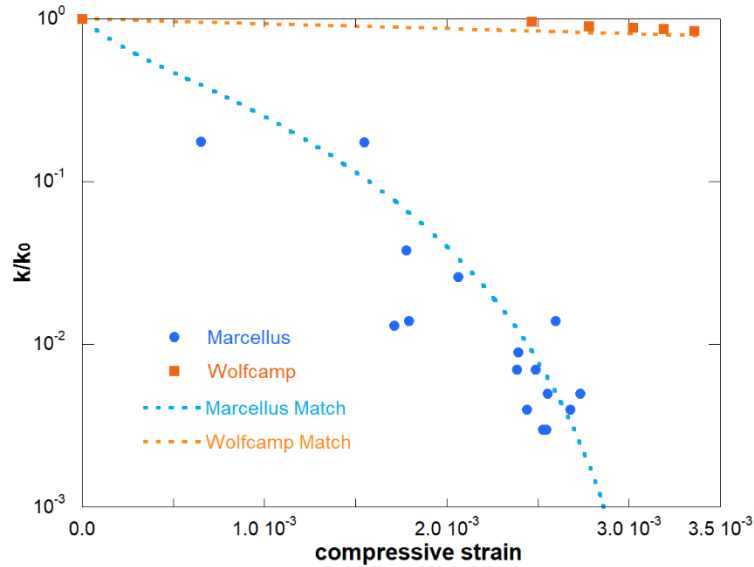


Figure 2-12: Experimental data for permeability and strain plotted with equation 28 for the Marcellus and Wolfcamp basins. The values used to match the Marcellus data were s/b_0 equal to 700, α equal to $7e^{-3}$, and K_{sk}/K_m equal to 0.7. The values used to match the Wolfcamp data were s/b_0 equal to 40, α equal to $6e^{-2}$, and K_{sk}/K_m equal to 1.0.

Conclusion

We showed that the Marcellus shale is predominantly clay while the Wolfcamp shale is predominantly quartz and calcite. This disparity in mineralogy is the basis for the differences in mechanical response to stress, including time dependent compaction upon initial loading. The magnitude of creep-induced strain is related to the clay content. Compaction reduces permeability in the lab and may reduce it in field operations as well. At constant stress, shale compaction is a function of mineralogy. At constant strain, permeability evolution is a function of pore stiffness and pore density. Pore stiffness is determined by pore geometry and distribution of minerals around the pore space. As fracture spacing increases, fracture compliance also increases as strain becomes distributed among fewer fractures.

Shales will experience different levels of permeability evolution at the same level of strain depending on their mineralogy, mineral distribution around flow channels, flow channel geometry, and fracture density. All of these observations point to a complex response within a heterogeneous

shale reservoir with the introduction of a new stress or strain. We showed that the Marcellus shale is characterized by high clay content as well as high fracture spacing, slit-like pores, and soft pores in a stiffer matrix. The Wolfcamp shale is characterized by high quartz and calcite content, lower fracture spacing, and rounder pores. These differences highlight that shales require additional characterization, and understanding the differences in pore structure is critical to predicting permeability evolution during oil and gas operations.

Acknowledgements

This work is a partial result of support from Chevron Energy Technology Company, and their support is gratefully acknowledged.

References

- Bandyopadhyay, K. (2009). Seismic anisotropy: Geological causes and its implications to reservoir geophysics. *Stanford University*.
- Berger, G., Lacharpagne, J. C., Velde, B., Beaufort, D., & Lanson, B. (1997). Kinetic constraints on illitization reactions and the effects of organic diagenesis in sandstone/shale sequences. *Applied Geochemistry*, 12(1), 23-35.
- Bolton, A. J., Maltman, A. J., & Fisher, Q. (2000). Anisotropic permeability and bimodal pore-size distributions of fine-grained marine sediments. *Marine and Petroleum Geology*, 17(6), 657-672.
- Bonnelye, A., Schubnel, A., David, C., Henry, P., Guglielmi, Y., Gout, C., ... & Dick, P. (2017). Elastic wave velocity evolution of shales deformed under uppermost crustal conditions. *Journal of Geophysical Research: Solid Earth*, 122(1), 130-141.
- Brown, G. P., DiNardo, A., Cheng, G. K., & Sherwood, T. K. (1946). The flow of gases in pipes at low pressures. *Journal of Applied Physics*, 17(10), 802-813.
- Brown, S. R. (1987). Fluid flow through rock joints: the effect of surface roughness. *Journal of Geophysical Research: Solid Earth*, 92(B2), 1337-1347.
- Candela, T., Brodsky, E. E., Marone, C., & Elsworth, D. (2014). Laboratory evidence for particle mobilization as a mechanism for permeability enhancement via dynamic stressing. *Earth and Planetary Science Letters*, 392, 279-291.
- Chang, C. P., Angelier, J., & Huang, C. Y. (2009). Subduction zone geodynamics.

- Civan, F., Rai, C. S., & Sondergeld, C. H. (2012). Determining shale permeability to gas by simultaneous analysis of various pressure tests. *SPE Journal*, 17(03), 717-726.
- Civan, F. (2013). Comparison of control volume analysis and porous media averaging for formulation of porous media transport. In *Modelling and Simulation in Fluid Dynamics in Porous Media* (pp. 27-53). Springer, New York, NY.
- Clark, S. P. (Ed.). (1966). *Handbook of physical constants* (Vol. 97). Geological Society of America.
- Crook, A. J., Yu, J. G., & Willson, S. M. (2002, January). Development of an orthotropic 3D elastoplastic material model for shale. In *SPE/ISRM Rock Mechanics Conference*. Society of Petroleum Engineers.
- Curtis, M. E., Sondergeld, C. H., Ambrose, R. J., & Rai, C. S. (2012). Microstructural investigation of gas shales in two and three dimensions using nanometer-scale resolution imaging Microstructure of Gas Shales. *AAPG bulletin*, 96(4), 665-677.
- Daigle, H., Hayman, N. W., Kelly, E. D., Milliken, K. L., & Jiang, H. (2017). Fracture capture of organic pores in shales. *Geophysical Research Letters*, 44(5), 2167-2176.
- Eberhardt, E., Stead, D., & Stimpson, B. (1999). Quantifying progressive pre-peak brittle fracture damage in rock during uniaxial compression. *International Journal of Rock Mechanics and Mining Sciences*, 36(3), 361-380.
- Elsworth, D. (1989, July). Thermal permeability enhancement of blocky rocks: One-dimensional flows. In *International Journal of Rock Mechanics and Mining Sciences & Geomechanics Abstracts* (Vol. 26, No. 3-4, pp. 329-339). Pergamon.
- Garrett, K. W., & Bailey, J. E. (1977). Multiple transverse fracture in 90 cross-ply laminates of a glass fibre-reinforced polyester. *Journal of Materials Science*, 12(1), 157-168.
- Goodman, R. E. (1989). Introduction to rock mechanics (Vol. 2). New York: Wiley.
- Gu, X., & Mildner, D. F. R. (2016). Ultra-small-angle neutron scattering with azimuthal asymmetry. *Journal of Applied Crystallography*, 49(3), 934-943.
- Hill, R. (1952). The elastic behaviour of a crystalline aggregate. *Proceedings of the Physical Society. Section A*, 65(5), 349.
- Horne, S. A. (2013). A statistical review of mudrock elastic anisotropy. *Geophysical Prospecting*, 61(4), 817-826.
- Islam, M., Skalle, P., Faruk, A. M. M., & Pierre, B. (2009, January). Analytical and numerical study of consolidation effect on time delayed borehole stability during underbalanced drilling in

shale. In *Kuwait International Petroleum Conference and Exhibition*. Society of Petroleum Engineers.

Izadi, G., Wang, S., Elsworth, D., Liu, J., Wu, Y., & Pone, D. (2011). Permeability evolution of fluid-infiltrated coal containing discrete fractures. *International Journal of Coal Geology*, 85(2), 202-211.

Javadpour, F., Fisher, D., & Unsworth, M. (2007). Nanoscale gas flow in shale gas sediments. *Journal of Canadian Petroleum Technology*, 46(10).

Javadpour, F. (2009). Nanopores and apparent permeability of gas flow in mudrocks (shales and siltstone). *Journal of Canadian Petroleum Technology*, 48(08), 16-21.

Kumar, H., Elsworth, D., Mathews, J. P., & Marone, C. (2016). Permeability evolution in sorbing media: analogies between organic-rich shale and coal. *Geofluids*, 16(1), 43-55.

Kwon, O., Kronenberg, A. K., Gangi, A. F., Johnson, B., & Herbert, B. E. (2004). Permeability of illite-bearing shale: 1. Anisotropy and effects of clay content and loading. *Journal of Geophysical Research: Solid Earth*, 109(B10).

Ladeira, F. L., & Price, N. J. (1981). Relationship between fracture spacing and bed thickness. *Journal of Structural Geology*, 3(2), 179-183.

Li, X., & Elsworth, D. (2015). Geomechanics of CO₂ enhanced shale gas recovery. *Journal of Natural Gas Science and Engineering*, 26, 1607-1619.

Loucks, R. G., Reed, R. M., Ruppel, S. C., & Jarvie, D. M. (2009). Morphology, genesis, and distribution of nanometer-scale pores in siliceous mudstones of the Mississippian Barnett Shale. *Journal of Sedimentary Research*, 79(12), 848-861.

Mavko, G., & Mukerji, T. (1998). Bounds on low-frequency seismic velocities in partially saturated rocks. *Geophysics*, 63(3), 918-924.

Mavko, G., Mukerji, T., & Dvorkin, J. (2009). The rock physics handbook: Tools for seismic analysis of porous media. *Cambridge University Press*.

Metz, V., Amram, K., & Ganor, J. (2005). Stoichiometry of smectite dissolution reaction. *Geochimica et Cosmochimica Acta*, 69(7), 1755-1772.

Narr, W., & Suppe, J. (1991). Joint spacing in sedimentary rocks. *Journal of Structural Geology*, 13(9), 1037-1048.

Narr, W. (1996). Estimating average fracture spacing in subsurface rock. *AAPG bulletin*, 80(10), 1565-1585.

Ortega, O. J., Marrett, R. A., & Laubach, S. E. (2006). A scale-independent approach to fracture intensity and average spacing measurement. *AAPG bulletin*, 90(2), 193-208.

Pan, Z., Ma, Y., Connell, L. D., Down, D. I., & Camilleri, M. (2015). Measuring anisotropic permeability using a cubic shale sample in a triaxial cell. *Journal of Natural Gas Science and Engineering*, 26, 336-344.

Polak, A., Elsworth, D., Yasuhara, H., Grader, A. S., & Halleck, P. M. (2003). Permeability reduction of a natural fracture under net dissolution by hydrothermal fluids. *Geophysical Research Letters*, 30(20).

Reuss, A. (1929). A. Reuss, Z. Angew. Math. Mech. 9, 49 (1929). *Z. Angew. Math. Mech.*, 9, 49.

Scholz, C. H. (1968). Experimental study of the fracturing process in brittle rock. *Journal of Geophysical Research*, 73(4), 1447-1454.

Simmons, G., & Wang, H. (1971). A Handbook of Single Crystal Elastic Constants and Calculated Aggregate Properties.

Sinha, S., Braun, E. M., Determan, M. D., Passey, Q. R., Leonardi, S. A., Boros, J. A., ... & Kudva, R. A. (2013, March). Steady-state permeability measurements on intact shale samples at reservoir conditions-effect of stress, temperature, pressure, and type of gas. In *SPE Middle East oil and gas show and conference*. Society of Petroleum Engineers.

Sondergeld, C. H., Newsham, K. E., Comisky, J. T., Rice, M. C., & Rai, C. S. (2010, January). Petrophysical considerations in evaluating and producing shale gas resources. In *SPE Unconventional Gas Conference*. Society of Petroleum Engineers.

Sone, H., & Zoback, M. D. (2013). Mechanical properties of shale-gas reservoir rocks—Part 1: Static and dynamic elastic properties and anisotropy. *Geophysics*, 78(5), D381-D392.

Tsang, Y. W., & Witherspoon, P. A. (1981). Hydromechanical behavior of a deformable rock fracture subject to normal stress. *Journal of Geophysical Research: Solid Earth*, 86(B10), 9287-9298.

Ulm, F. J., & Abousleiman, Y. (2006). The nanogranular nature of shale. *Acta Geotechnica*, 1(2), 77-88.

Voigt, W. (1889). On the relation between the elasticity constants of isotropic bodies. *Ann. Phys. Chem*, 274, 573-587.

Walsh, J. B. (1966). Seismic wave attenuation in rock due to friction. *Journal of Geophysical Research*, 71(10), 2591-2599.

Wu, H., & Pollard, D. D. (1995). An experimental study of the relationship between joint spacing and layer thickness. *Journal of Structural Geology*, 17(6), 887-905.

Chapter 3

Permeability Enhancement in Gas Shale due to Nitrogen Flooding

Abstract

We show that nitrogen flooding can double matrix permeability of gas shales. In laboratory experiments, nitrogen gas increased permeability in the bedding-parallel and bedding-perpendicular directions by 206% and 234%, respectively. Experiments are performed at constant stress, pore pressure, and temperature. We build a model to show that the permeability enhancement is controlled by the sorptive strain, pore geometry, and the spacing-to-aperture ratio. This work addresses how an organic-poor shale can experience large permeability changes driven by sorption induced strains. We plot methane and helium permeability curves as a function of pore pressure to isolate the portion of permeability evolution controlled by sorption. We independently build strain curves to solve for the sorptive strain and find good agreement between these two methods. This work demonstrates that matrix permeability in gas shales can be doubled, which suggests that ultimate recovery can be improved as well.

Introduction

Shale is a sedimentary rock composed primarily of silica, calcite, clays, and organic matter. Within the matrix, these individual mineral components form thin laminae separated by fracture planes which allow for fluid flow. The role of adsorption in shales has been a topic of great interest in both the scientific and industrial community, as *in situ* methane is adsorbed within the organic pore space. Adsorption in shales can account for up to half of the gas storage—in the case of low organic content, illite may be responsible for the additional sorptive storage (Lu et al., 1995).

As shale and coal are both fractured and sorptive media their responses to sorptive gases are similar (Kumar et al., 2016). Many permeability models have been developed to capture the effect of sorption in coals (Seidle et al., 1992; Palmer & Mansoori, 1998; Cui & Bustin, 2005; Shi & Durucan, 2005; Palmer, 2009), and permeability evolution in fractured, sorptive media is typically cast in terms of evolving strains (Izadi et al., 2011; Liu et al., 2011). These strains occur due to organic shrinkage within the matrix and sorption within fractures (Li et al., 2017). Increasing the concentration of a sorptive gas causes organic swelling which constricts flow channels and lowers permeability. In flow channels composed of sorptive minerals, the layer of adsorbed gas against the flow channel wall directly reduces the flow channel aperture (Sakhaeepour & Bryant, 2012). On the other hand, the shrinkage of organic matter increases fracture aperture (Levine, 1996; Liu & Rutqvist, 2010). The magnitude of permeability reduction caused by sorptive swelling represents the potential permeability enhancement in the event of desorption. In coals, methane desorption has been shown to increase permeability by 2 to 5-fold (Harpalani & Schraufnagel 1990). This has been directly observed in coal basins where permeability increased during depletion as organic shrinkage expanded fractures, which had a larger effect than the compression caused by the additional overburden stress (Mavor & Vaughn, 1998).

If the injection pressure of a sorptive gas is higher than the pore pressure, poromechanical expansion of the pore space competes with the permeability reduction caused by sorptive swelling (Liu et al., 2010; Kumar et al., 2016). At lower pore pressures, Langmuir swelling dominates. As the rate of permeability reduction due to Langmuir swelling decreases, the rate of permeability enhancement due to poromechanical expansion increases. Therefore, there is a point at which poromechanical expansion outpaces Langmuir swelling and permeability reduction reaches an inflection point and becomes permeability enhancement.

The main sorptive difference between coals and shales is the %TOC, with shales such as the Marcellus having 1-2% TOC and many coals have 90-99% TOC. A primary influence on the magnitude of sorption-driven permeability reduction is the %TOC, which in coals can cause a sorptive strain of 10^{-2} (Zhang et al., 2008; Robertson, 2008) and in shales 10^{-4} . However, permeability loss is often comparable. The purpose of this study is to address this disparity—that a smaller sorptive strain in shales can produce a similar permeability reduction. We propose that the spacing-to-aperture ratio s/b must be larger in shales in order to accommodate for the similar permeability evolution. We verify our hypothesis using nitrogen flooding, which demonstrates that reducing the sorptive strain can enhance the matrix permeability of shales.

Methods

We conducted two sets of experiments. The first was a suite of experiments designed to capture the sorptive strain evolution and sorptive permeability evolution in shales. With this information, we designed an experiment that isolated sorption-driven permeability evolution via nitrogen flooding at constant pore pressure.

First Experimental Set

Experiments were conducted in a triaxial vessel loaded with cores of Marcellus shale. For the first experiment, we allowed a sample to compact and we measured permeability at different pore pressures and constant temperature. We started with helium and then repeated the experiment with methane. We recorded strain throughout the experiments. Because the sorptive strain and poromechanical strain act in parallel at any given point, the methane experiment captured the additive effect whereas the helium strain captured the poromechanical effect only. Therefore, the helium strain curve could be subtracted from the methane curve in order to solve for the sorptive strain.

Second Experimental Set

The second set of experiments was nitrogen flooding—one sample cored in the bedding-parallel direction (19x16mm) and the other in the bedding-perpendicular direction (19x3mm). The stress state of the bedding-parallel flood was 24 MPa hydrostatic external stress and 6 MPa pore pressure. The stress state of the bedding-perpendicular flood had to be dropped to 10 MPa external hydrostatic stress and 6 MPa pore pressure in order to obtain a permeability measurement. Each sample was saturated with methane at 6 MPa pore pressure. After initial permeability measurements, the upstream gas lines were evacuated and vacuumed to remove all methane—this process took only 5 minutes in order to minimize gas leaving the sample on the upstream side. Once the lines were vacuumed, nitrogen was injected into the upstream side while the downstream lines remained full of methane at 5.7 MPa. The upstream line pressure was raised to 6.3 MPa and the pressure pulse test was repeated—with nitrogen infiltrating the sample from the upstream side and methane leaving on the downstream side. This process was repeated daily until there was no more change in permeability. We used pressure pulse tests (Brace 1968) to solve for the pressure decay, which in equation (1) is α :

$$k = \frac{\alpha\mu\beta L}{A} \frac{V_{up}V_{dn}}{V_{up}+V_{dn}} \quad (1)$$

Results

We resolved the strain data in order to model the isolated sorptive strain. We also isolated the sorption-driven permeability evolution of the first set of experiments. With the sorptive strain found at our selected pore pressure of 6 MPa, we conducted nitrogen flooding experiments and show that the anticipated results match the experimental results.

Resolving Sorptive Strain

We plot the strains versus pore pressure for helium and methane below. There are two strains acting in parallel with increasing pore pressure, the poromechanical expansion and the sorptive swelling:

$$\varepsilon_{total} = \varepsilon_{p+s} = \varepsilon_p + \varepsilon_s \quad (2)$$

Such that

$$\varepsilon_s = \varepsilon_{p+s} - \varepsilon_p \quad (3)$$

Also

$$\varepsilon_s = \varepsilon_L \frac{P}{P+P_L} \quad (4)$$

The methane strain data represent ε_{p+s} as both strains are present at increasing pore pressure. The strain for helium has no adsorption strain present, and is equal to ε_p . In order to find ε_s , we subtracted the helium strain from the methane strain and fit the resulting data to a Langmuir-type strain curve according to equation (4) above. The resulting curve was then compared to the Langmuir-type curve predicted for permeability evolution. From the plot below, the sorptive strain at 6 MPa is 1.15×10^{-4} , which can be used to calculate P_L and ε_L . A fitted curve with P_L equal to 7 MPa and ε_L equal to 2.75×10^{-4} provides a good match to the experimental data. Next we will show that it also captures the sorptive permeability evolution with an excellent fit.

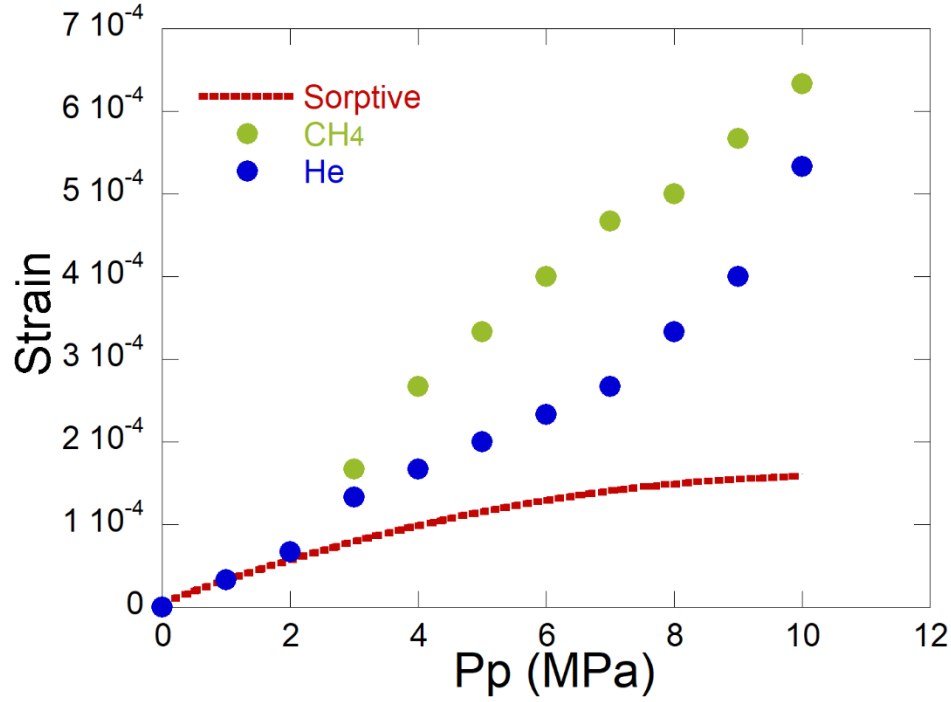


Figure 3-1: Strain vs. pore pressure for helium and methane. Subtracting the helium strain data from the methane strain data and fitting a Langmuir-type strain curve yields a Langmuir pressure P_L of 7 MPa and a Langmuir strain ϵ_L of 2.75×10^{-4} .

Solving for sorption-induced permeability evolution

When considering methane permeability evolution with increasing pore pressure, the poromechanical strain and the sorptive strain are parallel processes creating a net response at each location in the matrix such that permeability evolution can be modeled as processes in parallel (Wang et al., 2012):

$$\frac{k}{k_0} = \left(1 + \left(\frac{s}{b_0} + \frac{a(1-\nu)}{b_0} \right) (\epsilon_p + \epsilon_s) \right)^3 \quad (5)$$

Permeability models for multicomponent gas mixtures have been developed for coals (Mavor & Gunter, 2004). While an extended Langmuir equation for binary mixtures could be used (Wu et al., 2011), recognizing that the primary mechanism responsible for the sorptive strain evolution is methane desorption due to decreasing partial pressure allows for the model to be developed only accounting for the sorptive response of methane. Here we find that at 6 MPa, the sorptive strain

is equal to 1.15×10^{-4} and we fit a Langmuir curve with ε_L equal to 2.75×10^{-4} and P_L equal to 7 MPa. Revisiting equation (2) above,

$$\frac{k}{k_0} = (1 + A - B)^3 \quad (6)$$

$$A = \frac{\Delta b_p}{b_0} = \frac{s}{b_0} \varepsilon_p = \frac{s \Delta \sigma'}{E b_0} \quad (7)$$

$$B = \frac{\Delta b_s}{b_0} = \left(\frac{s}{b_0} + \frac{a(1-\nu)}{b_0} \right) \varepsilon_s = \left(\frac{s}{b_0} + \frac{1-\nu}{\alpha} \right) \varepsilon_L \frac{P}{P+P_L} \quad (8)$$

where k is the new permeability, k_0 is the original permeability, b/a is the aspect ratio of pores, A represents the change in aperture due to poromechanical expansion, and B represents the reduction in aperture due to sorptive swelling. This equation can be rearranged as follows:

$$\left(\frac{k}{k_0} \right)^{\frac{1}{3}} = 1 + A - B \quad (9)$$

$$\left(\frac{k}{k_0} \right)^{\frac{1}{3}} + 1 = \sqrt[3]{(1+A)^3} + (1-B) \quad (10)$$

$$(1-B)^3 = \left[\left(\frac{k}{k_0} \right)^{\frac{1}{3}} + 1 - \sqrt[3]{(1+A)^3} \right]^3 \quad (11)$$

We note that $(1-B)^3$ is the permeability evolution in the absence of poromechanical expansion and $(1+A)^3$ is the permeability evolution in the absence of Langmuir swelling. In this equation k/k_0 is the combined response, which is what was measured when using methane. We could cast this equation as follows:

$$\left(\frac{k}{k_0} \right)_{sorpative} = \left[\left(\frac{k}{k_0} \right)_{CH_4}^{\frac{1}{3}} + 1 - \left(\frac{k}{k_0} \right)_{He}^{\frac{1}{3}} \right]^3 \quad (12)$$

We plot equation (12) below and use the same sorption data derived in equation (8) to fit a curve to the data from equation (12). We find an excellent fit and good agreement between these two methods of solving for sorptive strain and sorptive permeability evolution.

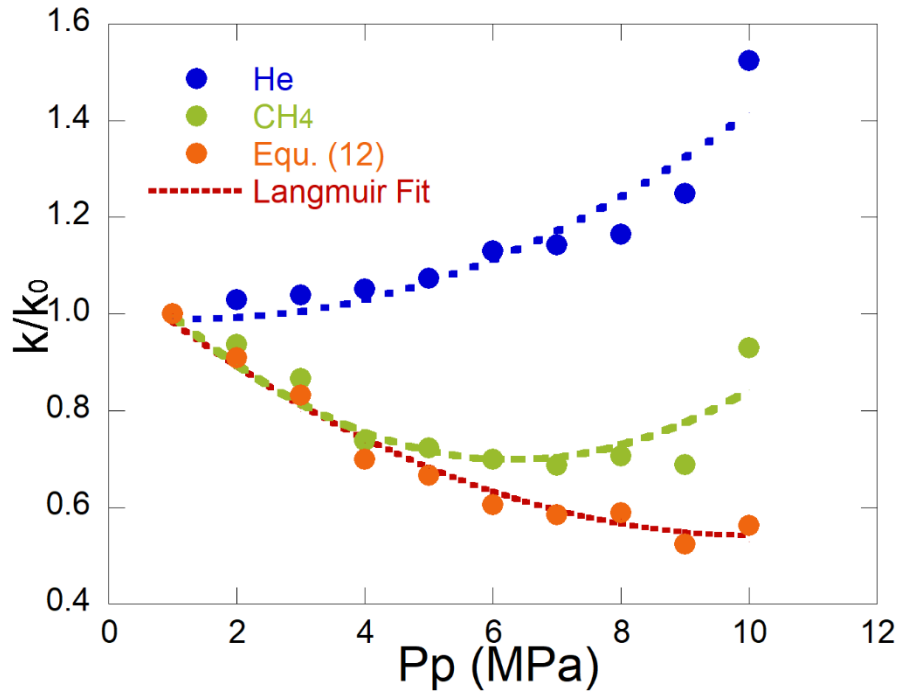


Figure 3-2: Solving for sorptive permeability evolution for processes in parallel. The light and dark blue dots represent the sorptive data points when calculated in series and in parallel, respectively—for the pressure range studied these values are very similar. The red regression curve is for a Langmuir-type permeability evolution with the Langmuir pressure as 7 MPa.

In the above figure, the red curve represents the permeability reduction due to sorption and the blue dots are the result of equation (8) above. The Langmuir-type curve that reflects a sorptive strain of 1.15×10^{-4} at 6 MPa, fits equation (8), and uses data from equations 2-4 with an ϵ_L of 2.75×10^{-4} , a Langmuir pressure of 7 MPa, an s/b_0 of 1500, and an aspect ratio b/a of 7×10^{-3} .

Nitrogen Flooding Experiments

We plotted α/α_0 for each run, where α_0 is the pressure decay when the sample is 100% methane. We found that the value of α increased 79% in the bedding-parallel direction and 57% in the bedding-perpendicular direction. In order to convert this to permeability, we modified the Brace equation to account for a mixture:

$$k = f_i(\mu_i \beta_i) \frac{\alpha L}{A} \frac{V_{up} V_{dn}}{V_{up} + V_{dn}} \quad (13)$$

where

$$fi = \frac{\alpha_n - \alpha_i}{\alpha_n - \alpha_1} \quad (14)$$

Since we only had three α measurements before each sample stabilized, the first value is at 100% methane, the last value is at 100% nitrogen, and the middle value found with equation (14). We found that the permeability increased 203% in the bedding-parallel direction and 236% in the bedding-perpendicular direction.

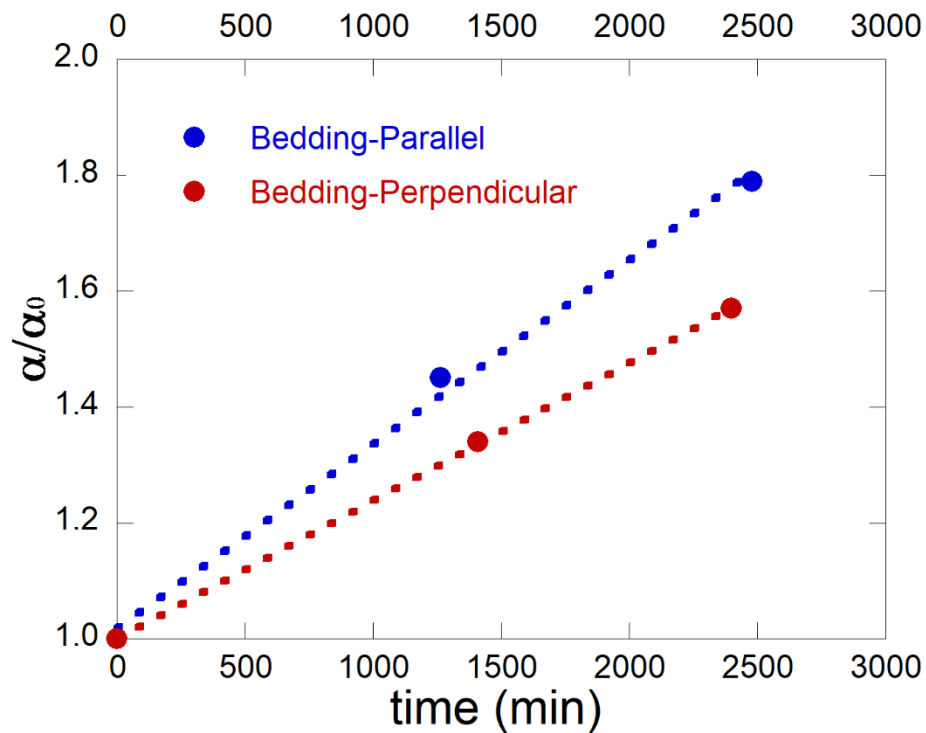


Figure 3-3: Normalized pressure decay α/α_0 . As N_2 infiltrates the sample, α increases.

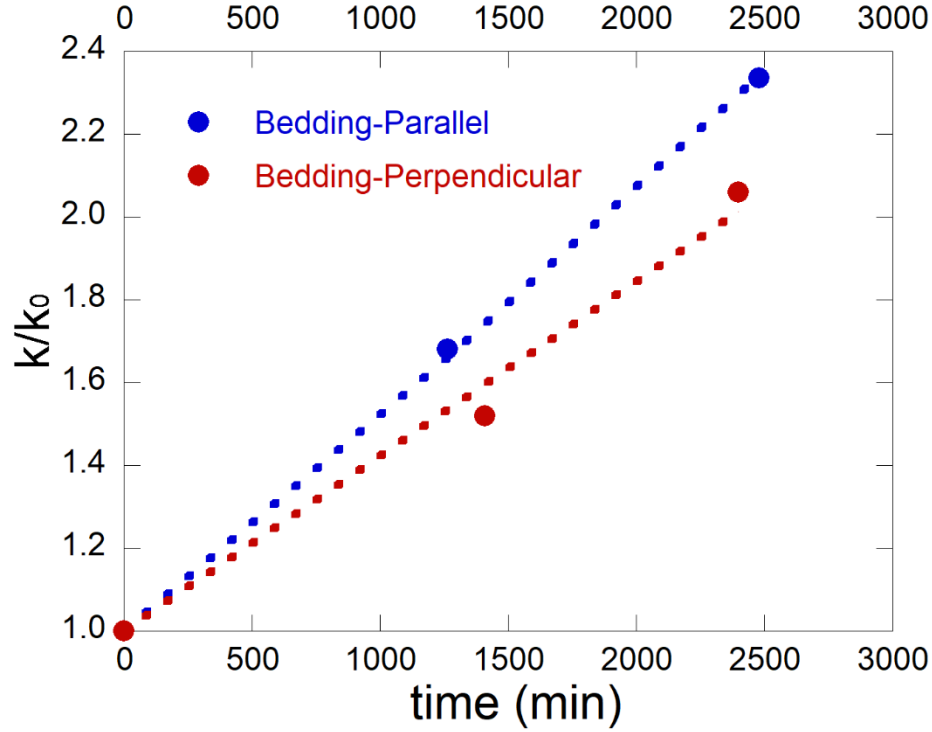


Figure 3-4: Normalized permeability evolution k/k_0 . Permeability increased 203% in the bedding-parallel direction and 236% in the bedding-perpendicular direction

At constant pore pressure, there is no poromechanical expansion. If the Langmuir strain at that pore pressure is known, there is no need to solve the Langmuir-type curve for the given pore pressure. Therefore,

$$\frac{k}{k_0} = \left(1 + \left(\frac{s}{b_0} + \frac{a(1-\nu)}{b_0} \right) \varepsilon_s \right)^3 \quad (15)$$

because the only strain is caused by methane desorption. While nitrogen is slightly sorptive, it has been shown to have less than one-fifth the sorptive strain in coals with very high %TOC (Chen et al., 2012). In the absence of Langmuir data, sorptive strains could be used directly to solve equation 15. In this case, s/b_0 is approximately 1500 while a/b_0 is 7×10^{-3} . These values are in agreement with the previous work performed to characterize Marcellus shale from chapters 1 and 2.

Discussion

We consider the mechanism by which organic matter shrinks in the presence of nitrogen gas at constant pore pressure. Next we explore the nature of the sorptive strain, which some have argued may not follow a Langmuir-type curve. Lastly, we consider alternative methods of sorption-driven permeability evolution and their potential for field application.

Lowering the partial pressure of methane causes desorption

In the case of nitrogen flooding at constant pore pressure, there is no poromechanical expansion in the pore space to enhance permeability. The only strain within the matrix is the shrinkage of the organic matter as methane desorbs. Whereas carbon dioxide has a stronger affinity to adsorb than methane, nitrogen is a very weakly sorptive gas. Indeed, it can be treated as a non-sorptive gas when compared to methane adsorption in shales and coals. The mechanism by which nitrogen induces desorption is by lowering the partial pressure of the methane. The swelling caused by the methane adsorption is removed and flow channels become less restricted. In shale gas reservoirs, gas depletion occurs first in the joint sets, then in the inorganic matrix, and lastly in the organic matter (Sang et al., 2016). Therefore, in the case of nitrogen flooding, the permeability enhancement would occur in this same order.

The small pressure differential at either end of the sample—which is ± 0.3 MPa—allows for movement of gas within the sample from the upstream to the downstream side. However, this is not the same mechanism as increasing the pore pressure within the sample itself—certainly there is a pressure gradient within the sample, but that same gradient exists when taking the original methane permeability measurements and is necessary to conduct pressure pulse tests. Identical circumstances—a core saturated with gas at 6 MPa pore pressure with a ± 0.3 MPa differential at the inlet and outlet in order to allow for fluid flow—exists in both the methane and nitrogen measurements.

Langmuir-type curves vs. BET-type curves

In some studies, sorptive storage data fit a BET-type curve better, suggesting that monolayer coverage may not be the best model (Yu et al., 2016). However, these studies focused on CO₂ injection at room temperature. At the pressure and temperature conditions explored, CO₂ was in the liquid phase which may be capable of multi-layer coverage. In the case of methane and nitrogen at room temperature, both are supercritical in the range studied here. There is too much energy in supercritical gases to expect measurable BET coverage; moreover, there is no data suggesting that additional adsorbed layers would contribute to the sorptive strain. Robertson (2005; 2008) showed that sorptive strains follow Langmuir-type curves in coals.

Alternative methods

The permeability enhancement caused by poromechanical expansion can be directly observed by using a non-sorptive gas such as helium. Some investigators are concerned that helium may have a sieving effect due to its small molecular diameter, but this should only be an issue at permeabilities where the flow channel diameter approaches the kinetic diameter, which typically occurs at permeabilities lower than 10^{-21} m². Some investigators have attempted to isolate the sorption-induced permeability reduction in the laboratory by increasing the pore pressure while maintaining constant effective stress. This method is useful, although limited when the %TOC is low.

While N₂ flooding may increase methane recovery by increasing matrix permeability, CO₂ is more sorptive than methane and causes more organic swelling at a given pore pressure. Adsorption of CO₂ lowers permeability but also increases methane recovery as the native methane is desorbed into the free gas phase (Pan & Connell, 2012; Li & Elsworth, 2015; Liu et al., 2017).

Conclusion

We have shown that the permeability of a gas shale matrix rock can be increased two-fold by nitrogen flooding. Laboratory results showed a 203% and a 236% permeability increase in the bedding-parallel and bedding-perpendicular directions, respectively. For the case of nitrogen flooding conducted at near-constant pore pressure considered here, it is important to isolate the sorption induced permeability reduction and sorptive strain in order to determine the possible permeability enhancement that could be caused by methane desorption.

In the case of CO₂ flooding which has received more attention, the main drawback is that the highly sorptive CO₂ reduces permeability by causing significantly more organic swelling than methane. In the case of N₂ flooding, the introduction of a non-sorptive species lowers the partial pressure of the methane, allowing it to desorb and organic shrinkage to occur. The magnitude of permeability enhancement that will result is strongly dependent on the spacing-to-aperture ratio of the fracture sets that exist in the matrix: high s/b ratios experience larger permeability enhancements than smaller s/b ratios. This in part explains how shales often have similar permeability evolution curves to coals which have 50-100 times more %TOC. As the sorptive strain is directly related to the %TOC, studies have shown that the sorptive strains in coals are 50-100 times larger than in shales. This indicates that for the finely laminated matrix shale, the spacing that exists between dominant flow channels may be 50-100 larger than in coals.

A limitation of the analysis in this study is that concentrations of nitrogen and methane throughout the experiment could not be directly measured within the core. However, the final permeability enhancement most likely corresponds to either 100% nitrogen or, more likely, to an irreducible methane concentration. Therefore, values of α in pressure pulse tests can be used to

interpolate relative concentrations of binary mixtures with reasonable accuracy such that mixture viscosity and compressibility can be adjusted to produce a measurement of permeability.

The prospect of nitrogen flooding in gas shales has been a part of the industry's conversations since the shale gas boom began. The main limitation is that the geometry of a well pad—pronged horizontal wells with noninteractive hydraulic fractures—does not allow for efficient flooding as in conventional fields that employ injection techniques. The huff-and-puff method has been proposed, although it is uncertain which gas would be produced. In the case of huff-and-puff with CO₂ the fact that the CO₂ preferentially adsorbs indicates that methane would be produced; however, the significant reduction in permeability calls into question how much methane would make it to the well head. Various schemes have been proposed to address the limitations of well orientation and communication—the main result of this work is to place a quantifiable permeability enhancement that would result—approximately 200% in the matrix—in order to allow operators to calculate potential revenue enhancement and accelerated gas capture to justify experimenting with different well patterns.

References

- Brace, W., Walsh, J. B., & Frangos, W. T. (1968). Permeability of granite under high pressure. *Journal of Geophysical research*, 73(6), 2225-2236.
- Chen, Z., Liu, J., Pan, Z., Connell, L. D., & Elsworth, D. (2012). Influence of the effective stress coefficient and sorption-induced strain on the evolution of coal permeability: model development and analysis. *International Journal of Greenhouse Gas Control*, 8, 101-110.
- Cui, X., & Bustin, R. M. (2005). Volumetric strain associated with methane desorption and its impact on coalbed gas production from deep coal seams. *AAPG Bulletin*, 89(9), 1181-1202.
- Harpalani, S., & Schraufnagel, R. A. (1990, January). Influence of Matrix Shrinkage and Compressibility on Gas Production From Coalbed Methane Reservoirs'. In *SPE annual technical conference and exhibition*. Society of Petroleum Engineers.

- Izadi, G., Wang, S., Elsworth, D., Liu, J., Wu, Y., & Pone, D. (2011). Permeability evolution of fluid-infiltrated coal containing discrete fractures. *International Journal of Coal Geology*, 85(2), 202-211.
- Kumar, H., Elsworth, D., Mathews, J. P., & Marone, C. (2016). Permeability evolution in sorbing media: analogies between organic-rich shale and coal. *Geofluids*, 16(1), 43-55.
- Levine, J. R. (1996). Model study of the influence of matrix shrinkage on absolute permeability of coal bed reservoirs. *Geological Society, London, Special Publications*, 109(1), 197-212.
- Li, X., & Elsworth, D. (2015). Geomechanics of CO₂ enhanced shale gas recovery. *Journal of Natural Gas Science and Engineering*, 26, 1607-1619.
- Li, X., Feng, Z., Han, G., Elsworth, D., Marone, C., Saffer, D., & Cheon, D. S. (2017). Permeability evolution of propped artificial fractures in Green River shale. *Rock Mechanics and Rock Engineering*, 50(6), 1473-1485.
- Liu, H. H., & Rutqvist, J. (2010). A new coal-permeability model: internal swelling stress and fracture-matrix interaction. *Transport in Porous Media*, 82(1), 157-171.
- Liu, J., Chen, Z., Elsworth, D., Qu, H., & Chen, D. (2011). Interactions of multiple processes during CBM extraction: a critical review. *International Journal of Coal Geology*, 87(3-4), 175-189.
- Liu, J., Chen, Z., Elsworth, D., Miao, X., & Mao, X. (2010). Linking gas-sorption induced changes in coal permeability to directional strains through a modulus reduction ratio. *International Journal of Coal Geology*, 83(1), 21-30.
- Liu, J., Yao, Y., Liu, D., & Elsworth, D. (2017). Experimental evaluation of CO₂ enhanced recovery of adsorbed-gas from shale. *International Journal of Coal Geology*, 179, 211-218.
- Lu, X. C., Li, F. C., & Watson, A. T. (1995). Adsorption measurements in Devonian shales. *Fuel*, 74(4), 599-603.
- Mavor, M. J., & Vaughn, J. E. (1998). Increasing coal absolute permeability in the San Juan Basin fruitland formation. *SPE Reservoir Evaluation & Engineering*, 1(03), 201-206.
- Mavor, M. J., & Gunter, W. D. (2004, January). Secondary porosity and permeability of coal vs. gas composition and pressure. In *SPE Annual Technical Conference and Exhibition*. Society of Petroleum Engineers.
- Palmer, I., & Mansoori, J. (1996, January). How permeability depends on stress and pore pressure in coalbeds: a new model. In *SPE Annual Technical Conference and Exhibition*. Society of Petroleum Engineers.

- Palmer, I. (2009). Permeability changes in coal: analytical modeling. *International Journal of Coal Geology*, 77(1-2), 119-126.
- Pan, Z., & Connell, L. D. (2012). Modelling permeability for coal reservoirs: a review of analytical models and testing data. *International Journal of Coal Geology*, 92, 1-44.
- Robertson, E. P. (2008). *Improvements in measuring sorption-induced strain and permeability in coal* (No. INL/CON-08-14637). Idaho National Laboratory (INL).
- Robertson, E. P. (2005). *Measurement and modeling of sorption-induced strain and permeability changes in coal*. United States. Department of Energy.
- Sakhaee-Pour, A., & Bryant, S. (2012). Gas permeability of shale. *SPE Reservoir Evaluation & Engineering*, 15(04), 401-409.
- Sang, G., Elsworth, D., Miao, X., Mao, X., & Wang, J. (2016). Numerical study of a stress dependent triple porosity model for shale gas reservoirs accommodating gas diffusion in kerogen. *Journal of Natural Gas Science and Engineering*, 32, 423-438.
- Seidle, J. P., Jeansonne, M. W., & Erickson, D. J. (1992, January). Application of matchstick geometry to stress dependent permeability in coals. In *SPE rocky mountain regional meeting*. Society of Petroleum Engineers.
- Shi, J. Q., & Durucan, S. (2005). A model for changes in coalbed permeability during primary and enhanced methane recovery. *SPE Reservoir Evaluation & Engineering*, 8(04), 291-299.
- Wang, S., Elsworth, D., & Liu, J. (2012). A mechanistic model for permeability evolution in fractured sorbing media. *Journal of Geophysical Research: Solid Earth*, 117(B6).
- Wu, Y., Liu, J., Chen, Z., Elsworth, D., & Pone, D. (2011). A dual poroelastic model for CO₂-enhanced coalbed methane recovery. *International Journal of Coal Geology*, 86(2-3), 177-189.
- Yu, W., Sepehrnoori, K., & Patzek, T. W. (2016). Modeling gas adsorption in Marcellus shale with Langmuir and bet isotherms. *SPE Journal*, 21(02), 589-600.
- Zhang, H., Liu, J., & Elsworth, D. (2008). How sorption-induced matrix deformation affects gas flow in coal seams: a new FE model. *International Journal of Rock Mechanics and Mining Sciences*, 45(8), 1226-1236.

Chapter 4

Relationships between Mechanical and Transport Properties in Shale

Abstract

We explore relationships among bulk modulus, crack density, and permeability through repetitive loading of Marcellus shale. Cumulative cyclic stressing (22-26 MPa with confinement of 24 MPa) is applied at a frequency of 0.05 Hz over 100,000 cycles. Changes in acoustic velocities are used to follow changes in dynamic bulk modulus, Poisson ratio, and crack density and to correlate these with bedding-parallel measurements of methane permeability. The shale is represented as an orthotropic elastic medium containing a dominant, noninteracting fracture set separated by thin laminae. An effective continuum model links permeability evolution to the evolution of the bulk modulus and crack density. Bulk modulus is linearly related to crack density by a scaling parameter representing rock fabric and fracture geometry. The Poisson ratio and bulk modulus of the intact, uncracked shale are deduced from our data. We propose a method for tracking permeability evolution of finely laminated shale using acoustic waves.

Introduction

Laminated shale can be characterized as an orthotropic material with a dominant fracture set oriented parallel to bedding (Bonnelye et al., 2016; Crook et al., 2002). This orthotropy results from nanometer to micrometer-wide bedding-parallel fractures separated by finely laminated thin stacks of minerals (Horne, 2013; Ulm & Abousleiman, 2006). Ultrasonic measurements confirm this orthotropy, often manifest as anisotropy based on the contrast between bedding-parallel laminations (Bandyodaphyay, 2009) and properties perpendicular to bedding (Vanorio et al., 2008).

The presence of fractures has been shown to influence both the mechanical and transport properties of rocks, to increase the anisotropy, with correlations apparent between elastic wave velocities and permeability (Gueguen & Schubnel, 2003). Permeability and compressional velocity both increase as the angle to bedding increases from perpendicular to parallel (Tutuncu et al., 2011). The permeability of shale is generally 10-100 times higher parallel to bedding than perpendicular to bedding (Bolton et al., 2000; Kwon et al., 2004; Pan et al., 2015). Shales are also observed to be approximately twice as stiff parallel to bedding than perpendicular to it (Sone & Zoback, 2013). Codifying such correlations between permeability and stiffness, via wave-speed measurements, is the focus of this work.

We use the influence of crack density on material properties (Bristow, 1960; Walsh, 1965) to link stiffness and permeability. Crack density may be considered as a scalar, a vector, a second rank tensor, or a fourth rank tensor depending on the application (Kachanov, 1992; O'Connell & Budiansky, 1974). For the special case of a cracked material (Budiansky & O'Connell, 1976) with non-interacting, parallel fracture sets (Kachanov, 1992; Piau, 1980) the elastic response is orthotropic or anisotropic and characteristic of shales (Hornby, 1994).

Various models relate crack density to permeability (Geuguen & Dienes, 1989) and to material stiffness (Kachanov et al., 1994; Sayers & Kachanov, 1990) with crack densities and permeability measured simultaneously (Fortin et al., 2011). For changes in state, the evolution of seismic velocities and permeability have both been used to measure crack density evolution, dilatancy, and crack propagation in granites, rock salt, and basalt (Oda et al., 2002; Schulze et al., 2001; Vinciguerra et al., 2005). Here, we explore the relationships among permeability, bulk modulus, and crack density in order to develop a method to track permeability evolution based on changes in geometry of the fracture network that impact the mechanical state of the solid.

Methods

We used cylindrical samples of Marcellus shale (19 mm in diameter and 16 mm in length, cut with bedding parallel to the cylinder axis) and subjected them to triaxial loading in a standard pressure vessel with custom components for simultaneous measurement of permeability and elastic wave properties. Several experiments were run in the course of developing our data set, but we focus here on one representative run that resulted in an especially long and continuous data set. The sample was loaded hydrostatically to 24 MPa and allowed to compact for a week. A suite of permeability measurements was conducted at an average pore pressure of 6 MPa using the pressure pulse method (Brace et al., 1968):

$$k = \frac{\mu\beta\alpha L}{A} \frac{V_{up}V_{dn}}{V_{up}+V_{dn}} \quad (1)$$

where k is permeability in m^2 , μ is gas viscosity in $\text{Pa}\cdot\text{s}$, β is gas compressibility in Pa^{-1} , α is the slope of the pressure pulse decay in s^{-1} , L is the sample length in meters, A is the sample's cross-sectional area in m^2 , and V_{up} and V_{dn} are the upstream and downstream reservoir volumes, respectively, measured in m^3 . The upstream and downstream volumes were determined using the real gas law. Values for μ and β were determined with NIST's online thermophysical properties software for pore pressure of 6 MPa and room temperature of 21°C. During the permeability measurements, upstream and downstream pressures were set to 6.3 MPa and 5.7 MPa respectively.

Permeability measurements were made concurrently with measurements of elastic properties. We used 500 kHz central frequency piezoelectric transducers to measure acoustic travel times, bulk modulus K , and Poisson ratio, ν , where:

$$\bar{K} = \rho \left(V_p^2 - \frac{4}{3} V_s^2 \right) \quad (2)$$

and

$$\bar{\nu} = \frac{V_p^2 - 2V_s^2}{2(V_p^2 - V_s^2)} \quad (3)$$

In a continuum framework containing cracks, \bar{K} is the cracked bulk modulus, $\bar{\nu}$ is the cracked Poisson ratio, and ρ is the shale density, which we measured to be 2600 kg/m³. V_p and V_s are the compressional wave velocity and shear wave velocity, respectively. The cracked Poisson ratio was used to calculate the crack density parameter at each time step. We used the scalar definition of the crack density parameter ϵ for long narrow elliptic cracks (Budiansky & O'Connell, 1976; O'Connell & Budiansky 1974):

$$\epsilon = \frac{45}{8} \frac{\nu - \bar{\nu}}{(1 - \bar{\nu})(10\nu - 8\nu\bar{\nu} - \bar{\nu})} \quad (4)$$

where $\bar{\nu}$ is the measured Poisson ratio of the cracked medium and ν is the corresponding Poisson ratio of the intact rock, in this case 0.277.

After samples compacted under hydrostatic load, we made initial measurements of permeability, bulk modulus, Poisson ratio, and crack density, and then began to cycle the axial stress from 22 to 26 MPa in 10 second intervals while keeping the confining stress at 24 MPa. This process was automated, such that we were able to cycle the stress approximately 4,000 times a day. There was a period of quiescence from days 10-20, to allow further monitoring of compaction during hydrostatic stressing. In 37 days, approximately 100,000 cycles were performed on the sample. Measurements for material properties were conducted once per day.

Results

Our basic data set consists of deformation measurements and the evolution of material properties as a function time during hydrostatic loading with small amplitude stress cycles. We focus in particular on the relationship between bulk modulus, permeability, and crack density and show that bulk modulus and crack density follow a linear relationship. Two of the unknowns—intact bulk modulus and intact Poisson ratio—can be deduced from our data.

Evolution of material properties over time

Figure 4-1 shows the evolution of material properties over time—permeability is plotted on the right axis on a logarithmic scale. The permeability dropped from an initial value of $6.7 \times 10^{-18} \text{ m}^2$ to a final value of $3.0 \times 10^{-20} \text{ m}^2$: a 233-fold decrease. The shape of the permeability curve shows faster permeability reduction at early times—one order of magnitude in the first few days. The crack density is also plotted in Figure 4-1 and over the experiment ranges from a starting value of 0.172 to 0.085—a 49% reduction. The permeability and crack density scale directly with each other, as do the bulk modulus and Poisson ratio. The bulk modulus ranged from a starting value of 12.1 GPa to 15.1 GPa and the Poisson ratio ranged from 0.197 to 0.237.

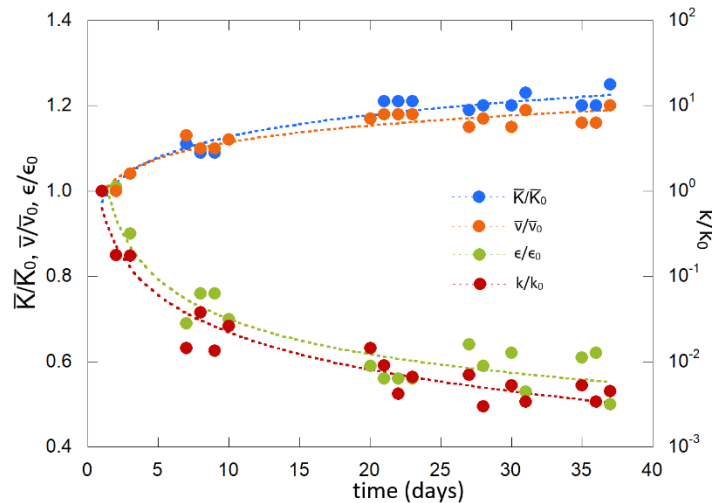


Figure 4-1: Evolution of material properties over time. Bulk modulus and Poisson ratio follow similar trends. The crack density is plotted on Cartesian axes while the permeability is plotted on semi-log axes: crack density evolution scales with the permeability evolution.

Evolution of permeability plotted against changing material properties

We monitored the evolution of permeability and acoustic travel time throughout the experiment (Figure 4-2). Figure 4-2 shows the evolution of permeability as a function of evolving material properties and acoustic travel times. Figure 4-2a shows the permeability evolution as a function of crack density. Permeability evolution is plotted on a logarithmic scale, and the figure shows that as crack density decreases linearly, permeability decreases logarithmically. Similarly,

as bulk modulus increases linearly in Figure 4-2b, permeability decreases linearly. Acoustic wave speeds are plotted against permeability evolution in Figures 2c and 2d. We note that as the p-wave velocity increased from 3.0 to 3.3 km/s, the permeability decreased two and a half orders of magnitude. As this sample is loaded parallel to bedding, we see a much larger change in V_p (Figure 4-2c) over the experiment than we do in V_s (Figure 4-2d). These plots are consistent with fracture closure and fracture shortening. This is clearly seen in Figure 4-2b comparing bulk modulus to permeability evolution: fractures close (decreased aperture b) as permeability evolution decreases and fracture length a shortens as bulk modulus increases.

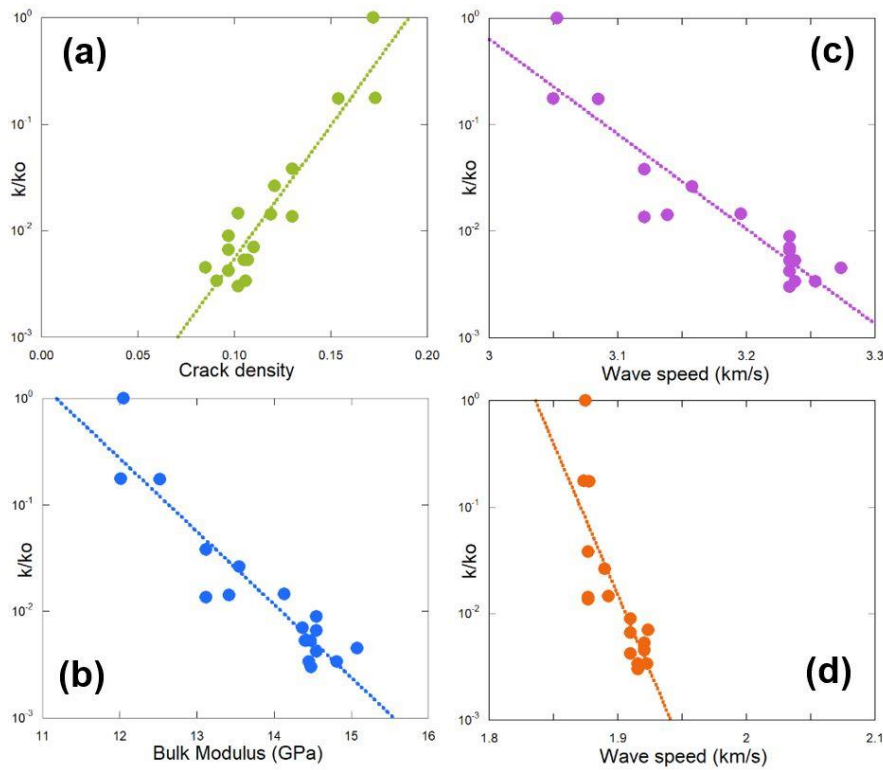


Figure 4-2: Mechanical properties plotted against permeability evolution. Figure 4-2a (top-left) shows permeability reduction as crack density decreases, largely driven by changes in fracture aperture. Figure 4-2b (bottom-left) shows bulk modulus increasing as permeability decreases, indicating that mechanical stress cycling led to a reduction in both the fracture length and fracture aperture. Figures 2c and 2d (V_p top-right and V_s bottom-right, respectively) show the change in acoustic wave speeds as permeability was reduced.

Relationship between bulk modulus, crack density, and intact Poisson ratio

We find that bulk modulus varies linearly with crack density (Figure 4-3) and can be cast in the following form:

$$\bar{K} = K(1 - \alpha\epsilon) \quad (5)$$

where \bar{K} is the measured bulk modulus of the cracked medium, K is the intact bulk modulus, ϵ is the dimensionless crack density parameter, and α is a constant equal to 2.0. As α increases, stiffness decreases for a given crack density (Equation 5). This suggests that α is related to material properties including rock fabric and bedding orientation. Others have noted that the parameter α depends on the matrix and fluid properties, the geometry of the cracks, and the interactions between them (Benson et al., 2006; Faoro et al., 2013). Also plotted on Figure 4-3 is bulk modulus vs. cracked Poisson ratio. The value of the Poisson ratio at the intact bulk modulus value of 18.2 GPa is 0.277 and corresponds to the value of the intact Poisson ratio in the absence of cracks.

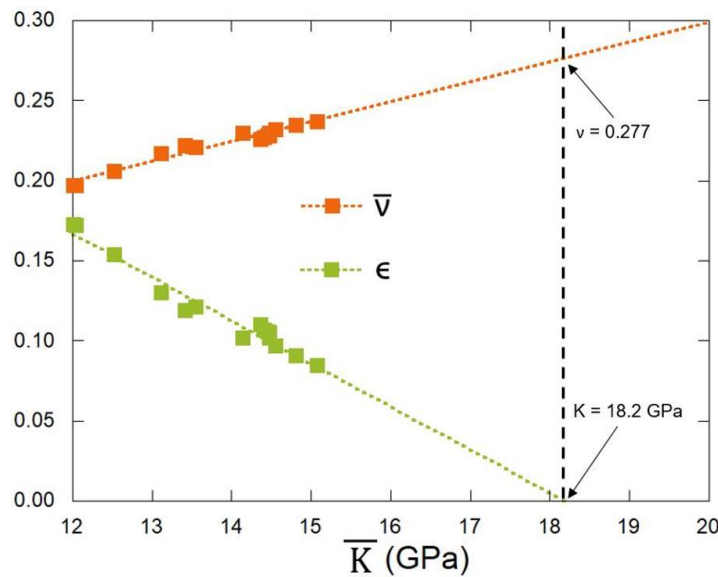


Figure 4-3: Bulk modulus vs. crack density and Poisson ratio. The data indicate linear relationships and show the values of the intact bulk modulus and intact Poisson ratio. Interchanging the axes would show that the bulk modulus and crack density parameter are related through Equation (5).

Discussion

Here we explore the relationships among three measured rock properties and the subsequent evolution of mechanical and transport properties after applying a cyclic deviatoric stress to a sample of Marcellus shale. Our findings indicate that the relationship between bulk modulus and crack density is linear. We apply an effective continuum model to relate the bulk modulus and the permeability through the crack density parameter. We use the scalar definition of crack density set out by O'Connell and Budiansky (1974) due to its popularity, ease of implementation, and applicability to orthotropic materials with noninteractive fractures. In order to relate crack density to permeability, we cast crack density in terms of the area and perimeter of an ellipsoidal crack. The aperture of the ellipse is then defined in terms of the crack density. We find that permeability evolution can be related to crack density evolution.

Finding the unknowns K and ν

In Equations 1-5 there are three unknowns: intact bulk modulus K , intact Poisson ratio ν , and the slope of the K vs. ϵ relationship α in Figure 4-3. We measure every other variable in Equations 1-5. The intact bulk modulus of 18.2 GPa corresponds to the value of the measured bulk modulus when crack density is zero (Figure 4-3). Plotting bulk modulus vs. measured Poisson ratio, the intact Poisson ratio is that value of ν when K equals 18.2 GPa, the intact bulk modulus. Therefore the intact Poisson ratio is equal to 0.277. The value of the slope α can be found directly by solving Equation 5. In this case, α is 2.0. This is a useful scheme because the system unknowns are reduced to measured values.

Relating crack density to permeability

The definition of the crack density parameter suggests that permeability must change with a change in crack density. While Equation (4) has limitations—cracks are assumed parallel and the medium must be orthotropic—these limitations vanish as the rock approaches the idealizations of these two assumptions (Gottesman et al., 1980; Kachanov, 1992). Both the Poisson ratio and the bulk modulus can be measured with acoustic waves. In order to relate the crack density to the permeability, we recast the crack density parameter using the geometric interpretation below. In O’Connell and Budiansky (1974) crack density is defined as:

$$\epsilon = \left(\frac{2N}{\pi}\right)\left(\frac{A^2}{P_{el}}\right) \quad (6)$$

where N is the number of cracks per unit volume, A is the area of an ellipsoid crack πab , and P_{el} is the perimeter of the ellipsoid. Rearranging for b :

$$b^2 = \frac{\epsilon P_{el}}{2N\pi a^2} \quad (7)$$

If a circle with radius b and perimeter $2\pi b$ is inscribed into the ellipsoid, with $P_{el} > P_c$, then

$$b > \frac{\epsilon}{Na^2} \quad (8)$$

In the absence of the generation of new cracks, N is a constant such that

$$\frac{b}{b_0} = f\left(\frac{\epsilon}{\epsilon_0}\right) \frac{\epsilon}{\epsilon_0} \frac{a_0^2}{a^2} \quad (9)$$

where f is a function to track crack density evolution and, thereby, remove the inequality sign. In the case of penny shaped cracks

$$\frac{a_0}{a} = \frac{E}{E_0} = \frac{(1-2\nu)}{(1-2\nu_0)} \frac{K}{K_0}. \quad (10)$$

For flow between parallel plates, the cubic law holds such that

$$\frac{k}{k_0} = \left(\frac{b}{b_0}\right)^3 \quad (11)$$

and we can cast permeability evolution in terms of the crack density evolution:

$$\frac{k}{k_0} = \left(f\left(\frac{\epsilon}{\epsilon_0}\right) \frac{\epsilon}{\epsilon_0} \frac{(1-2\nu)^2}{(1-2\nu_0)^2} \frac{K^2}{K_0^2} \right)^3 = \left(f\left(\frac{\epsilon}{\epsilon_0}\right) \frac{\epsilon}{\epsilon_0} \frac{(1-2\nu)^2}{(1-2\nu_0)^2} \frac{(1-\alpha\epsilon)^2}{(1-\alpha\epsilon_0)^2} \right)^3. \quad (12)$$

The crack density evolution function $f(\epsilon/\epsilon_0)$ captures the departure of the fracture set from the idealized geometries used to form the above equations. A realistic constraint on this linear function would be that $f(\epsilon_0/\epsilon_0) = 1$, suggesting an equation of the form

$$f\left(\frac{\epsilon}{\epsilon_0}\right) = (1 + \beta) \frac{\epsilon}{\epsilon_0} - \beta \quad (13)$$

where β is a constant between 0 and 1. β is a property of the rock fabric, geometry, and the tortuosity of the flow channels. A large β value corresponds to a system where the change in aperture is much larger than that suggested by the idealized case. For this experiment, a β of 0.75 captures the permeability evolution in Equation (12) with an excellent fit, as seen in Figure 4-4.

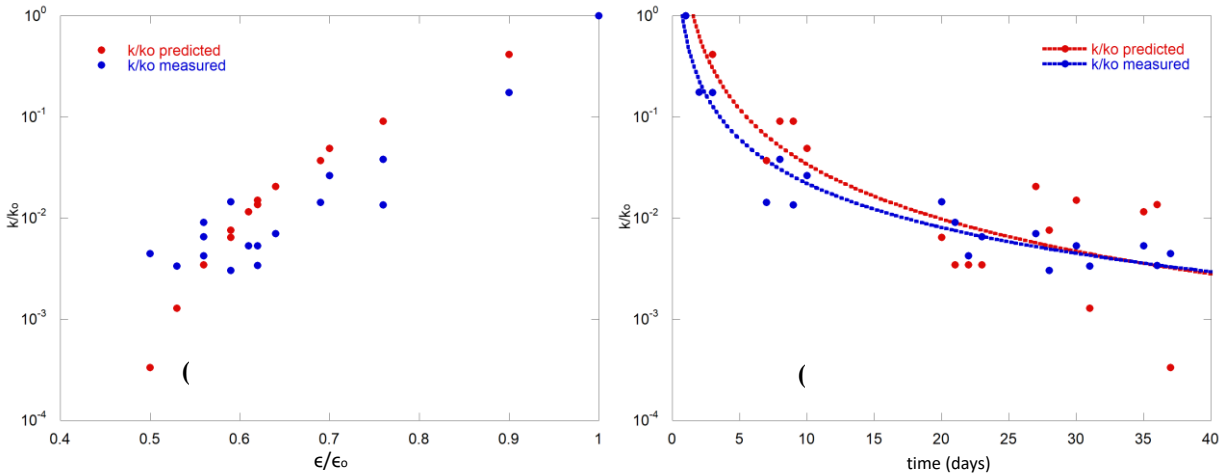


Figure 4-4: Measured and predicted permeability evolution plotted against crack density evolution ϵ/ϵ_0 (4a) and time (4b). The predicted permeability is Equation (12). Figure 4-4a has no spread compared to the scatter of the measured permeability. Figure 4-4b shows that the predicted permeability has more spread than the measured permeability when plotted versus time, although the trend lines are very close to each other.

Conclusion

We mechanically stressed a shale to explore the evolution of transport and mechanical properties over time. We also explored the evolution of transport properties as a function of the evolution of these mechanical properties. Our findings show relationships among bulk modulus, permeability,

and crack density. We derived a model to relate permeability evolution to the product of stiffness evolution and crack density evolution using geometric arguments. In summary:

- Crack density scales directly with permeability
- Crack density has a linear relationship with bulk modulus. The scaling parameter α is related to rock properties.
- Both the intact bulk modulus and intact Poisson ratio can be deduced from cross plots
- Permeability is cast in terms of mechanical property evolution cubed

Shale offers a unique opportunity for characterization because of its severe orthotropy and dominant fracture set oriented parallel to bedding. Measuring permeability in this orientation provides a useful analog to hydrocarbon production in a reservoir in which the shale is also oriented with flow occurring parallel to bedding. The use of the crack density parameter also offers insights into hydrocarbon movement from the matrix into hydraulic fractures.

The relationships explored here are relevant to exploration geologists, geophysicists, seismologists and others. We have related permeability evolution solely to acoustic velocities and deduced constants: α , K , and ν . Perhaps the most immediate opportunity to apply this research is in reservoir characterization, where well logs and fiber optics cables both measure acoustic velocities. The work presented here suggests that these velocities can be used to monitor permeability evolution indirectly and provides a second method to calculate permeability evolution in conjunction with pressure and production data.

Acknowledgements

This work is the result of support from the Chevron Energy Technology Company. This support is gratefully acknowledged.

References

- Bandyopadhyay, K. (2009). Seismic anisotropy: Geological causes and its implications to reservoir geophysics. Stanford University.
- Benson, P., Schubnel, A., Vinciguerra, S., Trovato, C., Meredith, P., & Young, R. P. (2006). Modeling the permeability evolution of microcracked rocks from elastic wave velocity inversion at elevated isostatic pressure. *Journal of Geophysical Research: Solid Earth*, 111(B4).
- Bolton, A. J., Maltman, A. J., & Fisher, Q. (2000). Anisotropic permeability and bimodal pore-size distributions of fine-grained marine sediments. *Marine and Petroleum Geology*, 17(6), 657-672.
- Bonnelye, A., Schubnel, A., David, C., Henry, P., Guglielmi, Y., Gout, C., ... & Dick, P. (2017). Elastic wave velocity evolution of shales deformed under uppermost crustal conditions. *Journal of Geophysical Research: Solid Earth*, 122(1), 130-141.
- Brace, W., Walsh, J. B., & Frangos, W. T. (1968). Permeability of granite under high pressure. *Journal of Geophysical research*, 73(6), 2225-2236.
- Bristow, J. R. (1960). Microcracks, and the static and dynamic elastic constants of annealed and heavily cold-worked metals. *British Journal of Applied Physics*, 11(2), 81.
- Budiansky, B., & O'connell, R. J. (1976). Elastic moduli of a cracked solid. *International journal of Solids and structures*, 12(2), 81-97.
- Crook, A. J., Yu, J. G., & Willson, S. M. (2002, January). Development of an orthotropic 3D elastoplastic material model for shale. In *SPE/ISRM Rock Mechanics Conference*. Society of Petroleum Engineers.
- Faoro, I., Vinciguerra, S., Marone, C., Elsworth, D., & Schubnel, A. (2013). Linking permeability to crack density evolution in thermally stressed rocks under cyclic loading. *Geophysical Research Letters*, 40(11), 2590-2595.
- Fortin, J., Stanchits, S., Vinciguerra, S., & Guéguen, Y. (2011). Influence of thermal and mechanical cracks on permeability and elastic wave velocities in a basalt from Mt. Etna volcano subjected to elevated pressure. *Tectonophysics*, 503(1-2), 60-74.
- Gottesman, T., Hashin, Z., & Brull, M. (1980). Effective elastic moduli of cracked fiber composites. *Advances in composite materials*, 1, 749-758.
- Gueguen, Y., & Dienes, J. (1989). Transport properties of rocks from statistics and percolation. *Mathematical geology*, 21(1), 1-13.
- Gueguen, Y., & Schubnel, A. (2003). Elastic wave velocities and permeability of cracked rocks. *Tectonophysics*, 370(1-4), 163-176.

- Hornby, B. E., Schwartz, L. M., & Hudson, J. A. (1994). Anisotropic effective-medium modeling of the elastic properties of shales. *Geophysics*, 59(10), 1570-1583.
- Horne, S. A. (2013). A statistical review of mudrock elastic anisotropy. *Geophysical Prospecting*, 61(4), 817-826.
- Kachanov, M. (1992). Effective elastic properties of cracked solids: critical review of some basic concepts. *Applied Mechanics Reviews*, 45(8), 304-335.
- Kachanov, M., Tsukrov, I., & Shafiro, B. (1994). Effective moduli of solids with cavities of various shapes. *Applied Mechanics Reviews*, 47(1S), S151-S174.
- Kwon, O., Kronenberg, A. K., Gangi, A. F., Johnson, B., & Herbert, B. E. (2004). Permeability of illite-bearing shale: 1. Anisotropy and effects of clay content and loading. *Journal of Geophysical Research: Solid Earth*, 109(B10).
- O'Connell, R. J., & Budiansky, B. (1974). Seismic velocities in dry and saturated cracked solids. *Journal of Geophysical Research*, 79(35), 5412-5426.
- Oda, M., Takemura, T., & Aoki, T. (2002). Damage growth and permeability change in triaxial compression tests of Inada granite. *Mechanics of Materials*, 34(6), 313-331.
- Pan, Z., Ma, Y., Connell, L. D., Down, D. I., & Camilleri, M. (2015). Measuring anisotropic permeability using a cubic shale sample in a triaxial cell. *Journal of Natural Gas Science and Engineering*, 26, 336-344.
- Piau, M. (1980). Crack-induced anisotropy and scattering in stressed rocks: effective elastic moduli and attenuation. *International Journal of Engineering Science*, 18(4), 549-568.
- Sayers, C. M., & Kachanov, M. (1991). A simple technique for finding effective elastic constants of cracked solids for arbitrary crack orientation statistics. *International Journal of Solids and Structures*, 27(6), 671-680.
- Schulze, O., Popp, T., & Kern, H. (2001). Development of damage and permeability in deforming rock salt. *Engineering Geology*, 61(2-3), 163-180.
- Sone, H., & Zoback, M. D. (2013). Mechanical properties of shale-gas reservoir rocks—Part 1: Static and dynamic elastic properties and anisotropy. *Geophysics*, 78(5), D381-D392.
- Tutuncu, A. N., & Mese, A. I. (2011, January). Relationship between permeability, acoustic, mechanical and strength anisotropies in unconventional reservoirs and seal shales. In *45th US Rock Mechanics/Geomechanics Symposium*. American Rock Mechanics Association.
- Ulm, F. J., & Abousleiman, Y. (2006). The nanogranular nature of shale. *Acta Geotechnica*, 1(2), 77-88.

Vanorio, T., Mukerji, T., & Mavko, G. (2008). Emerging methodologies to characterize the rock physics properties of organic-rich shales. *The Leading Edge*, 27(6), 780-787.

Vinciguerra, S., Trovato, C., Meredith, P. G., & Benson, P. M. (2005). Relating seismic velocities, thermal cracking and permeability in Mt. Etna and Iceland basalts. *International Journal of Rock Mechanics and Mining Sciences*, 42(7-8), 900-910.

Walsh, J. B. (1965). The effect of cracks on the compressibility of rock. *Journal of Geophysical Research*, 70(2), 381-389.

VITA

Brandon Schwartz

Education

The Pennsylvania State University, University Park, PA *December 2018*
PhD, Energy and Mineral Engineering

The Pennsylvania State University, University Park, PA *December 2016*
MS, Energy and Mineral Engineering

The Pennsylvania State University, University Park, PA *May 2016*
BS, Petroleum Engineering

Experience

The Pennsylvania State University, University Park, PA *August 2017—May 2018*
Lecturer

- Taught an introductory course on energy and the environment
- Designed course content including lecture slides, homework, and exams
- Lectured in a classroom of 700 students

G3 Center, The Pennsylvania State University, University Park, PA *August 2015—December 2018*
Research Assistant

- Researched permeability evolution in shales using triaxial vessels
- Modeled variations in pore structure using FEM to capture strain-driven permeability evolution
- Presented bi-weekly and annual updates to sponsor

The Institute for Natural Gas Research, University Park, PA *May 2016—January 2018*
Program Liaison

- Interface with students, faculty, departments, research centers, and industry sponsors
- Managed complete life cycle of feasibility study for domestic company
- Created a graduate level course to teach students how to bridge the gap between product development and basic research

Southwestern Energy Company, Houston, TX *May 2014—August 2014*
Engineering Intern *May 2015—August 2015*

- Determined cause of structural damage leading to early equipment failure in positive displacement pumps
- Recommended maintenance schedule to recapture \$2 million in annual revenue
- Improved fluid transport equations to account for turbulent flow—this was above and beyond my assigned duties and solved a problem previously unidentified by any other engineers